The Chemical Vapour Deposition of Tantalum - in long narrow channels

Mugabi, James Atwoki

Publication date:
2014

Document Version
Publisher's PDF, also known as Version of record

Technical
University of
Denmark

THE CHEMICAL VAPOUR DEPOSITION OF TANTALUM

- IN LONG NARROW CHANNELS

Ph.D Thesis

James Atwoki Mugabi

September 2014

DTU Energy Conversion
Department of Energy Conversion and Storage

THE CHEMICAL VAPOUR DEPOSITION OF TANTALUM

- IN LONG NARROW CHANNELS

Ph.D. Thesis by James Atwoki Mugabi

September 2014

Proton conduction Section

Department of Energy Conversion and Storage

Technical University of Denmark

Supervisor:

Professor Niels J. Bjerrum

Co-supervisors

Associate Professor Irina Petrushina

Senior Researcher Erik Christensen

CTO Tantaline A/S Søren Eriksen

Date of Submission:

30th September 2014

In this project, we use many One-dimensional continuous flow reactors with axial dispersion…

Alternatively,

Many tubes are used in this project…

"*Any intelligent fool can make things bigger, more complex, and more violent. It takes a touch of genius—and a lot of courage to move in the opposite direction.*"

-- E. F. Schumacher

ABSTRACT

Tantalum's resistance to corrosion in hot acidic environments and its superior metallic properties have made it a prime solution as a construction material or protective coating to equipment intended for use in such harsh chemical and physical conditions. The high price of tantalum metal limits its use as a construction material for process equipment, with the cheaper alternative being the construction of equipment from steel and then protecting it with a thin but efficacious layer of tantalum.

Chemical Vapour Deposition (CVD) is chosen as the most effective process to apply thin corrosion protective layers of tantalum because of the process' ability to coat complex geometries and its relative ease to control.

This work focuses on studying the CVD of tantalum in long narrow channels with the view that the knowledge gained during the project can be used to optimise the commercial coating process that Tantaline A/S and Alfa Laval (Sweden) use to manufacture tantalum coated plate heat exchangers.

Experiments are done by coating the inner side of long, thin stainless steel tubes in the temperature range of 700 – 950 ^{O}C and pressure range of 25 – 990 mbar while using different reactant concentrations in order to document the effects of these properties on the tantalum deposition rates.

A kinetic model is developed upon the foundation of a Computational Fluid Dynamics (CFD) and Thermal model in order to broaden the understanding of the process and to identify the key control parameters.

The developed model fits well at temperatures below 900 ^{O}C and the entire pressure range, but fails above 900 ^{O}C due to a change in reaction mechanism. Furthermore, Scanning Electron Microscope (SEM) imaging is used to show that the morphology of the deposited tantalum has a large dependence on temperature and that there is a major change in morphology between 850 – 900 ^{O}C.

The effects of system pressure and precursor partial pressure are also studied, and were found to have relevance to the tantalum distribution along the substrates but little effect on the structural morphology of the deposited layer.

In the implemented mechanism of reaction, $TaCl_3$ is found to have a lot of relevance such that it is the main precursor to the surface reaction and that the overall deposition rates follow its abundance.

An experiment with a real plate heat exchanger is also done and the corresponding model implemented with satisfactory results.

RESUMÉ

Tantals korrosionsbestandighed i varme sure miljøer samt dets overlegne metalliske egenskaber har gjort det til en førsteklasses løsning som konstruktionsmateriale eller som beskyttende belægning til udstyr beregnet til brug under barske kemiske og fysiske forhold. Den høje pris på tantalmetal begrænser imidlertid dets anvendelse som et grundmateriale til procesudstyr. Et billigere alternativ er at fremstille udstyret af stål for derefter at beskytte det med et tyndt, men effektivt lag af tantal.

`Chemical Vapour Deposition´ (CVD) er valgt som den mest effektive proces til at lave tynde korrosionsbeskyttende lag af tantal på baggrund af metodens evne til at belægge komplekse geometrier og fordi den er relativt let at styre.

Dette arbejde er fokuseret på at studere CVD af tantal i lange tynde rør med det mål, at den opnåede viden i løbet af projektet, kan bruges til at optimere den kommercielle belægningsproces, Tantaline A / S og Alfa Laval (Sverige) bruger til at fremstille tantalbelagte pladevarmeveksler.

Forsøgene er udført ved at belægge indersiden af lange, tynde rør af rustfrit stål opvarmet til 700-950 ^{O}C og tryksat til 25-990 mbar, samtidig med at der bruges forskellige reaktantkoncentrationer.

En kinetisk model er udviklet på baggrund af et Computational Fluid Dynamics (CFD) og en varmestyringsmodel for at udvide forståelsen af processen og til at identificere de vigtigste kontrolparametre.

Den udviklede model passer godt med eksperimenterne ved temperaturer under 900 ° C og i hele trykområdet, men ikke over 900 ^{O}C formodentlig på grund af en ændring i reaktionsmekanismen. Endvidere, Elektron Mikroskopi (SEM) anvendes til at vise at morfologien af tantal belægningen har en stor afhængighed af belægningstemperatur, og at der er en væsentlig ændring i morfologi mellem 850-900 ^{O}C.

Virkningerne af tryk og precursor partialtryk er også undersøgt og viste sig at have relevans for tantal fordelingen langs substratet, men ringe effekt på den strukturelle morfologi af det udfældede lag.

Indførelsen af $TaCl_3$ vidste sig at have stor relevans, da det er den vigtigste precursor for overflade reaktionen, og at den samlede reaktionshastighed følger dens partialtryk.

Et eksperiment med en pladevarmeveksler er også gennemført, og den tilsvarende model har givet et tilfredsstillende resultat.

PREFACE

This Ph.D. thesis has been written as part of the Extreme Corrosion project, which is a collaboration between the Technical University of Denmark, Alfa Laval (Sweden) and Tantaline A/S. The project is funded by the Danish National Advanced Technology Foundation, now known as InnovationsFonden.

I have found the project to be a steep but enjoyable learning platform that not only tested ones academic qualities but also the social and psychological skills.

The success of the project in fulfilling its aims is a result of several people passionately working together for the common good. Very many thanks to my supervisors Professor Niels J. Bjerrum, Assoc. Professor Irina Petrushina, Senior Researcher Erik Christensen and Tantaline CTO Søren Eriksen for their varying but indispensable contributions to the completion and success of the project. Also, thank you for choosing me to do the project.

Special thanks are also reserved for the project's steering committee members, who allowed us the freedom to work as we saw fit. These were Jakob Dahl Wedel (InnovationsFonden), Kenneth Rehhoff (Alfa Laval), Mats Nilsson (Alfa Laval) and Peter Lock (Tantaline).

Finally:

This is for you mum (Violet Schmidt Kabagarama). Thank you for everything that you do for me.

TABLE OF CONTENTS

1 INTRODUCTION

The development of high performance materials to meet the demands of modern industrial processes is a call that many have risen to answer; and has led to many exciting products and discoveries in the field of material science. One such demand to be met is to protect metallic equipment, used in processing aggressive acidic media, from corrosion.

Many materials have been used to achieve deferring degrees of corrosion resistant process equipment such as platinum, tantalum, titanium, zirconium, stainless steel and the Hastelloy™ family of products. However, the stand out material in terms of resisting hot acidic environments has been tantalum.[1-3] Tantalum owes its corrosion resistance to the formation of a very stable tantalum (V) oxide layer on its surface when exposed to air or aqueous media.

Tantalum is relatively very expensive and it's in many cases economically impracticle to construct entire pieces of equipment, such as heat exchangers, out of tantalum metal. The solution to this issue has been to construct such equipment out of traditional materials such as stainless steel and then apply a thin solid layer of tantalum on the surface in order to provide a corrosion resistant finish. This allows the equipment to have the properties of tantalum on the surface while maintaining the advantages of the bulk material e.g. the workability and cost efficience of stainless steel.

Tantalum's high afinity towards oxygen makes it impossible to electrodeposit it from aqueous solutions because the more stable tantalum (V) oxide is formed instead. It is possible to apply tantalum coatings by the electrolysis of molten tantalum halides however the process is very sensitive to impurities, difficult to control and mainly limited to manufacturing tantalum metal. Due to this, the process of chemical vapour deposition (CVD) is prefered. [4-6]

The chemical vapour deposition of tantalum is preferable to other deposition processes such as physical vapour deposition because of the practicality of the process and the fact that it can be used on substrates of any geometric shape. No line of sight is required between precursor-generation and deposition. CVD of tantalum is most commonly performed within a temperature range of 700 - 1500°C while using tantalum (V) chloride as the precursor and hydrogen as a reducing carrier gas. The use of other tantalum halides such as the penta bromide and penta iodide as precursor is also reported in conjunction with plasma enhanced CVD at 450°C. [6-9]

The aim of this project is to study the CVD of tantalum in long narrow channels while using tantalum (V) chloride as a precursor and hydrogen as a reducing carrier gas. The motivation for the study is to facilitate the optimisation of a CVD coating process for the Alfa Laval®/ Tantaline® plate heat exchanger, CB30.

2 TANTALUM

Tantalum has grown in prominence over the last two decades because of its use in modern electronics with its primary use being the manufacture of capacitors for portable electronics and other compact electric systems. [10] Other industrial uses of tantalum include high-temperature applications and chemical processing which take advantage of tantalum's high melting point and resistance to corrosion. [10, 11] In the medical field, tantalum is also used to make bone repair implants to take advantage of its good biocompatibility. [12-14]

2.1 Properties of Tantalum

Tantalum is a grey transition metal with an atomic number of 73 and electronic configuration $4f^{14}5d^{3}6s^{2}$. It is commonly extracted from the mineral coltan which is a mixture of the columbite [(Fe, Mn)Nb_2O_6] group and tantalite [(Fe, Mn)Ta_2O_6] group of minerals. [15]

Tantalum has three known crystal structures with different properties, namely: Body centred cubic, Tetragonal and Face centred cubic. [16] Bulk tantalum has the body centred cubic (b.c.c) structure and is commonly referred to as α-tantalum while tetragonal tantalum is referred to as β-tantalum.

Alpha-tantalum has superior mechanical and chemical properties to β-tantalum, which in turn has superior electrical properties. The former is tough, ductile, has a Knoop hardness of 300 – 400, and a low electric resistivity; while β-tantalum is brittle, has a Knoop hardness greater than 900, and has a very high electrical resistivity. This implies that α-tantalum is more suited for mechanical and chemical applications such as corrosion protection while β-tantalum is preferred in the manufacture of capacitors, which make use of its dielectric properties. [16, 17]

Table 1: Properties of α-tantalum at room temperature [18]

Crystal structure	b.c.c
Electrical resistivity *[μΩ·cm]*	12.45
Density *[g/cm³]*	16.65
Melting Point *[^{O}C]*	2996
Boiling Point *[^{O}C]*	5458
Specific Heat Capacity *[J/mol·K]*	25.35
Thermal conductivity *[W/m·K]*	54
Thermal expansion *[x $10^{-6}/^{O}C$]*	6.5

Table 2: Lattice Parameters of α-Ta, f.c.c-Ta and the four hypothetical β-Ta structures[19]

No.	Hypothetical Structures	Space group	Lattice constants (nm)	Density (g/cm^{-3})
α-Ta (b.c.c)		lm(- 3)m	a = 0.331 - 0.333	16.55 – 16.27
f.c.c-Ta		Fm(- 3)m	a = 0.439 - 0.448	14.21 – 13.37
A	β-Uranium	$P4_2/mnm$	a = 1.0194 c = 0.5313	16.33
B_1	Distorted A 15		a = 0.534 c = 0.994	16.96
B_2		Pm(- 3)n	a = 0.534 c = 0.497	16.96
C	Superlattice Ta (N)	P4/mmm	a = b = 1.029 c = 0.92	16.70
D	Hexagonal	$P6_3/mmc$	a = 0.283 c = 0.534	16.23

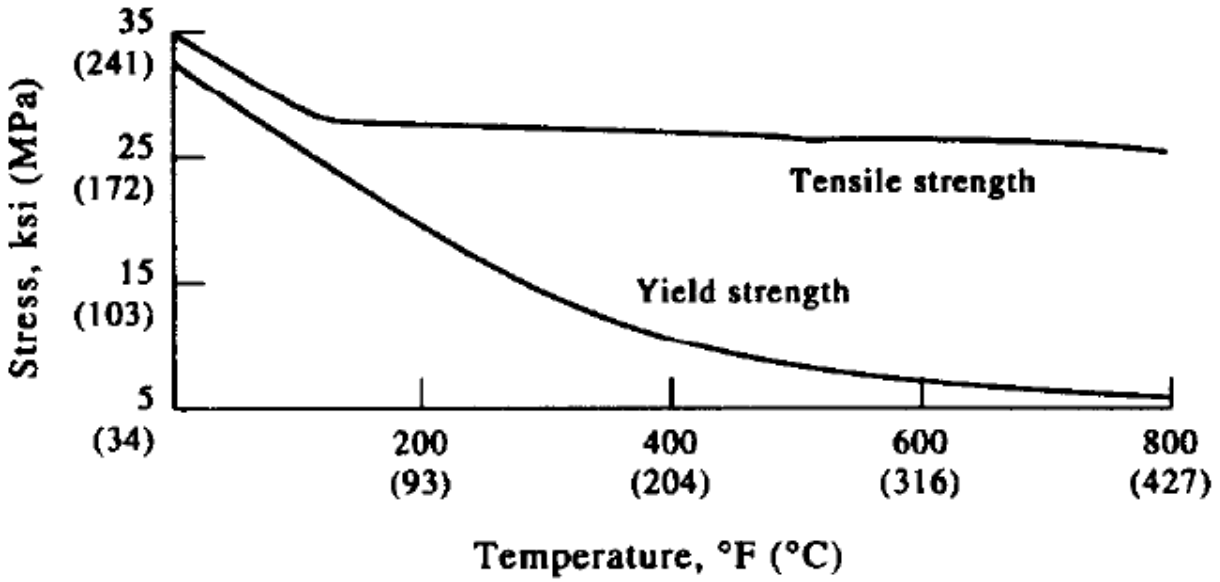

Figure 1: Tensile strength and Yield strength Vs Temperature (1mm thick tantalum sheet) [10]

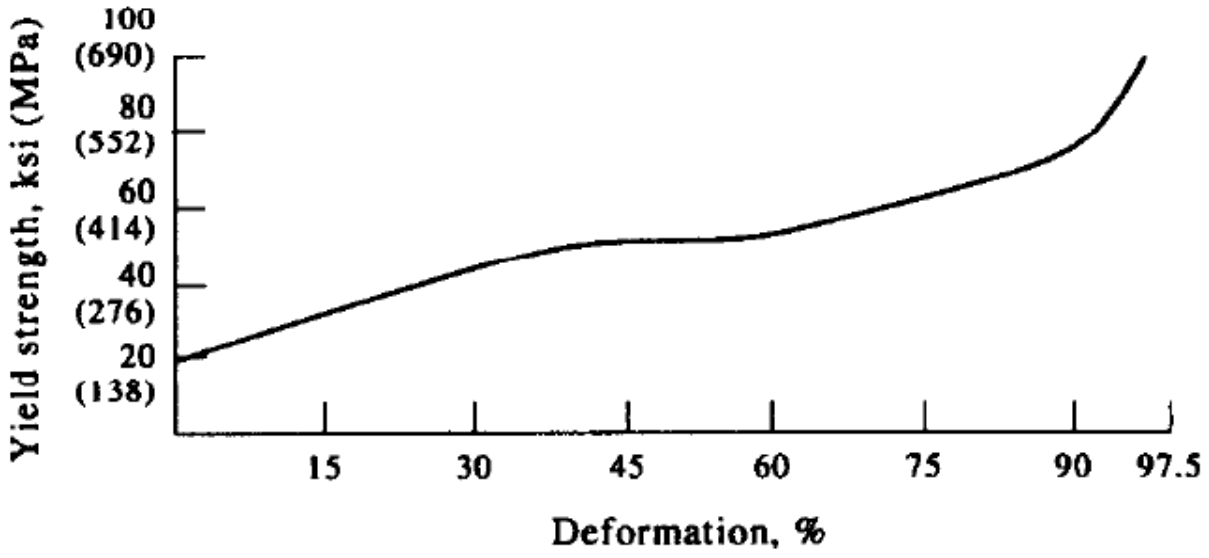

Figure 2: Yield Strength Vs Deformation (51mm thick tantalum sheet)[10]

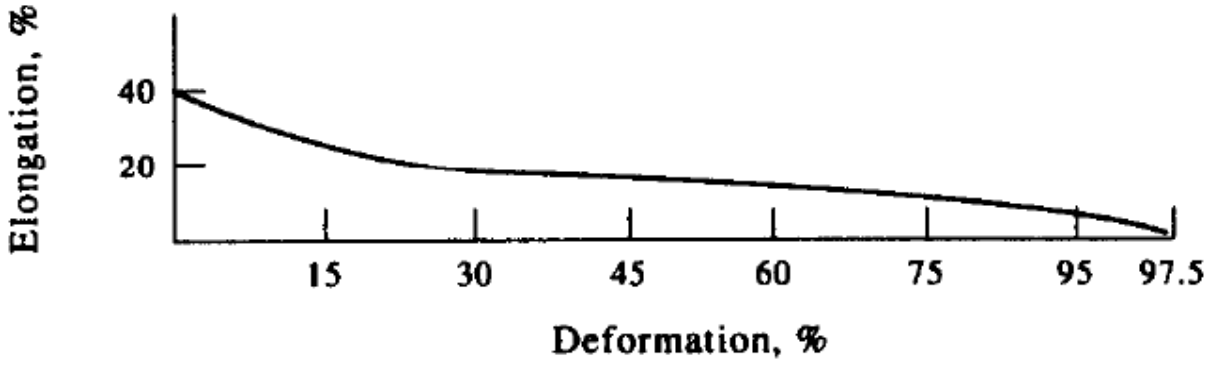

Figure 3: Elongation Vs Deformation (51mm thick tantalum sheet)[10]

2.2 The Chemistry and Corrosion Resistance of Tantalum

Tantalum is a notoriously passive metal such that at temperatures below 150°C it can only be readily attacked by hydrofluoric acid, fluoride ions in acidic solution and free sulphur trioxide. Hot, strong

alkalis such as boiling aqueous solutions of metal hydroxides can also attack tantalum however the process is slow. [10, 20] It is for this reason that tantalum is used to construct process equipment meant for harsh chemical environments. Tantalum is also used to make surgical tools and implants because of its inertness to bodily fluids.

Tantalum has a high afinity for the interstitial gases oxygen, hydrogen, nitrogen, and carbon. These can form a solid solution with tantalum but can also react to form very stable compounds suchas tantalum carbide, which enhance the refractory ability of tantalum. It is the formation of a dense, non-porous layer of tantalum(V) oxide on the surface that passivates tantalum and gives it its superior corrosion resistance in aqeous media.

At temperatures above 250°C tantalum combines with molecular hydrogen and is embrittled by it; however, the hydride decomposes at temperatures above 800°C in vacuum. [20] This solubility/ reaction of hydrogen and tantalum is well studied and found to have a positive correlation to the hydrogen pressure and a negative correlation to temperature as shown in Figure 4 and Figure 5. [21, 22]

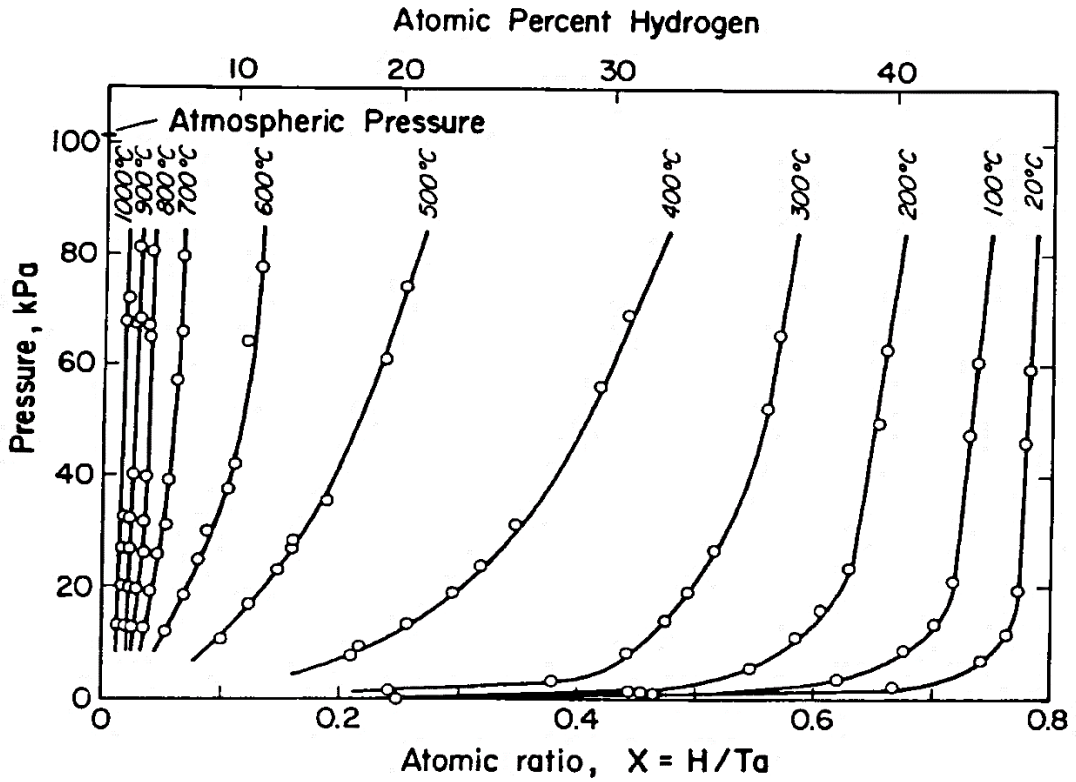

Figure 4: Ta-H Pressure-composition isotherms [21]

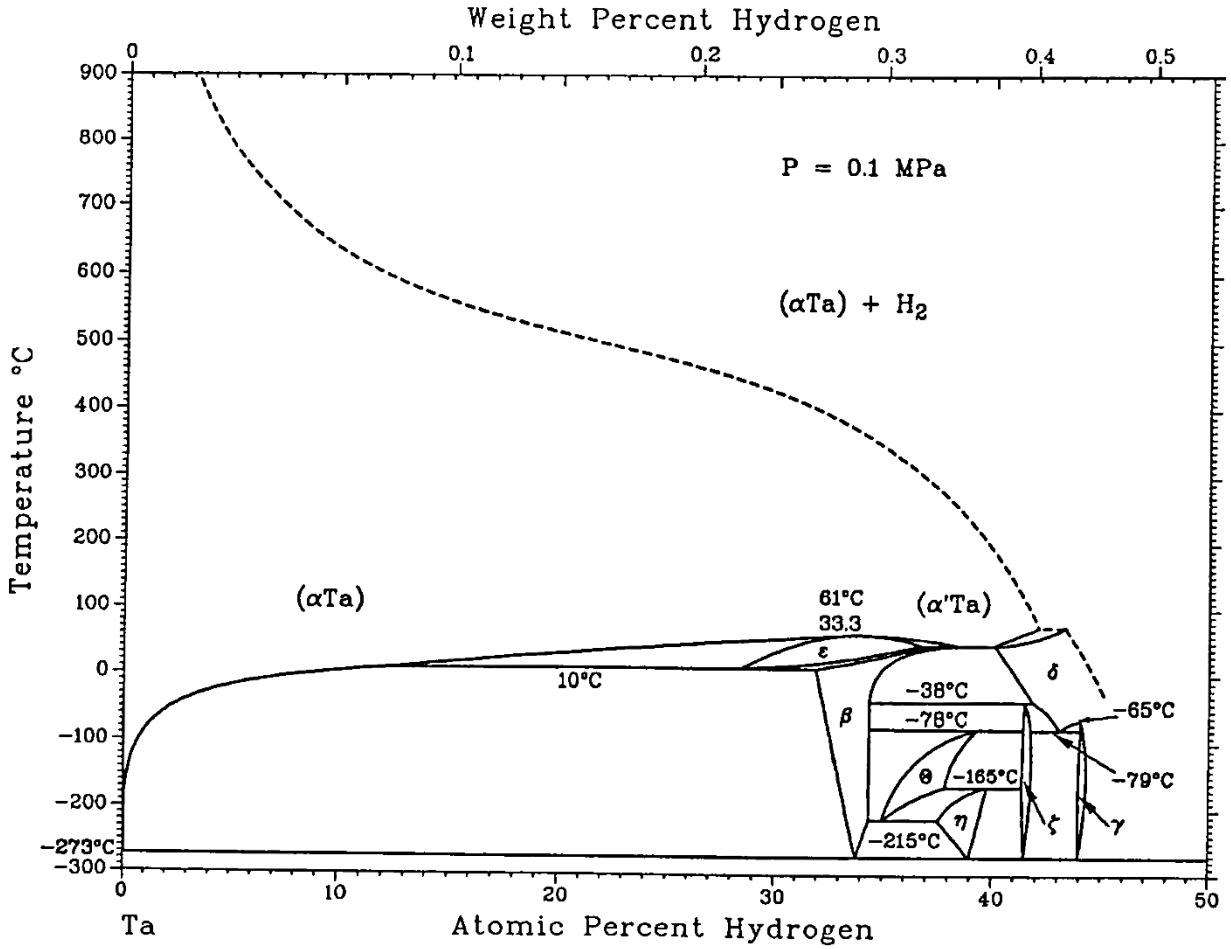

Figure 5: Ta-H Phase diagram [21]

There have been several studies investigating the corrosion resistance of tantalum and its alloys in comparison with other metals, and the outcome of these studies has been a unanimous agreement on the superiority of pure tantalum.

One of these studies is the erosion-corrosion test carried out by *Bermudez et. al.* using 10 wt% HCl, at room temperature, and α-alumina abrasives at 1000 rpm for 168 hours.[1] The study shows that tantalum is not only corrosion resistant but also wear resistant to a degree that far exceeds the other candidate materials. Moreover, the change in weight of tantalum due to the erosion-corrosion test is so little that is has to be raised by 2 orders of magnitude (x100) to be visible on the scale. The results from the study are shown in Figure 6.

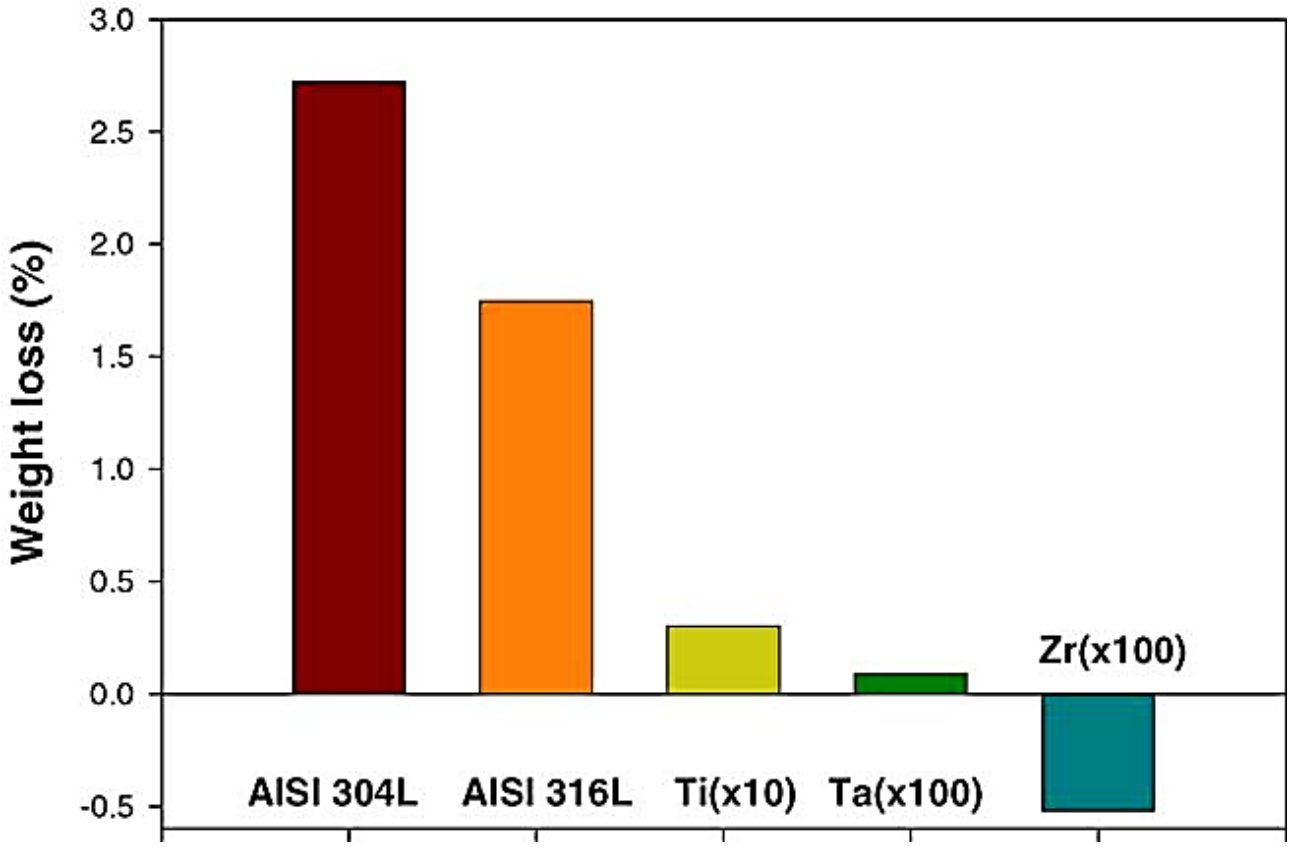

Figure 6: Percentage weight loss after 168h erosion-corrosion test. [1]

Studies by *Robin and Rosa* [2] investigate the corrosion resistance of varying compositions of the niobium - tantalum alloys in hydrochloric acid and phosphoric acid. In both cases, pure tantalum is found to be the most corrosion resistant. The studies further show that tantalum is immune to both 20 wt% HCl and 47 wt% H3PO4 at 150°C.

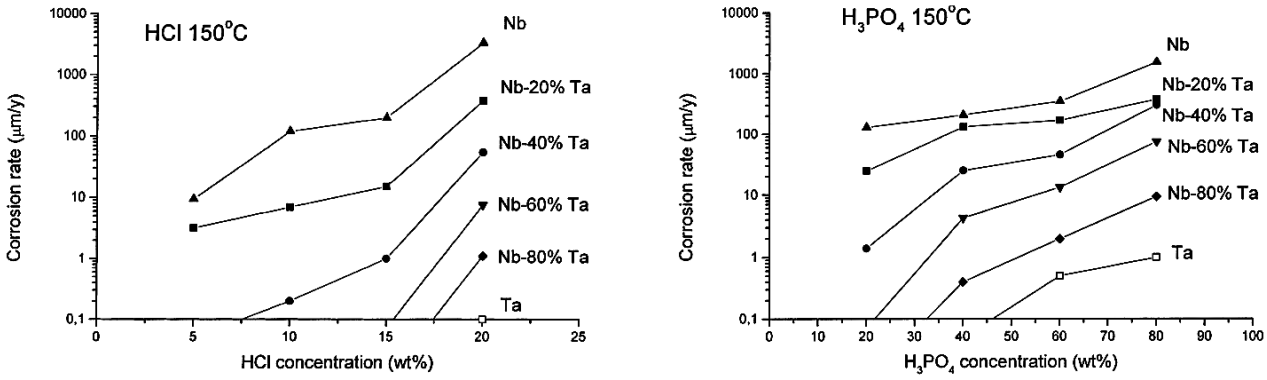

Figure 7: Corrosion Rates of Niobium, Tantalum and their alloys Vs Acid Concentration at 150°C [2]

Previous work by *A. Robin* [23] had studied the corrosion resistance of the niobium – tantalum alloys in boiling sulphuric acid and shown that pure tantalum is inert in up to 40 wt.% boiling H2SO4. The results of the study are shown in Table 3.

Table 3: Corrosion rates [x 10^{-8} g cm^{-2} h^{-1}] of re-crystallized niobium, tantalum and their alloys in boiling 40 wt. % H_2SO_4 solutions [23]

t(h)	48	96	216	408
Nb	1170	1210	1370	1090
Nb-20Ta	260	290	270	290
Nb-40Ta	70	65	50	49
Nb-60Ta	-	-	6.1	14
Nb-80Ta	-	-	10	2.4
Ta	0	0	0	0

Research by *Kouril et. al.* [3] and *Nikiforov et. al.* [11] explored the use of tantalum as a construction material for high temperature steam electrolysers and the results showed that tantalum is stable in 85 wt% H3PO4 at both 120°C and 150°C. Moreover, the material loss due to corrosion was found to be less than 0.001 mm/yr.

3 CHEMICAL VAPOUR DEPOSITION (CVD)

According to *Xu et. al.* [24], Chemical Vapour Deposition is 'a process whereby a thin solid film is deposited onto a substrate through chemical reactions of the gaseous species.' It is a similar process to the Physical Vapour Deposition (PVD) processes, such as sublimation and sputtering, but is differentiated by the occurrence/ need of a chemical reaction at the substrate surface.

The techniques involved in CVD have been developed slowly over the last century to reach the current state. The process had its first practical use in the coating of filaments with carbon or metal in order to increase the lifetime of incandescent lamps during the late 19th century. Other applications such as the production of high purity refractory metals (e.g. tantalum and titanium), and high performance coating soon followed in the early 20th century leading to the semiconductor boom of the 1960s. [18]

This timeline by *H. O Pierson* [18] provides a milestone overview of the history of CVD since 1960:

1960: The terms CVD and PVD were introduced to distinguish between the processes

1960: CVD is used in semiconductor fabrication

1960: Titanium Carbide coatings to harden tools, and the CVD of tungsten were developed

1963: Plasma Enhanced CVD in used in the production of electronics (PECVD/ PACVD)

1968: Industrial use of CVD coated cemented carbides

1980s: CVD of Diamond coatings is developed

1990s: Quick growth of metallo-organic CVD (MOCVD)

1990s: Processes that combine both CVD and PVD are developed for making semiconductors. CVD is used in optics

3.1 Principles of Chemical Vapour Deposition

In a general CVD system one or more volatile chemical precursors of the gaseous phase are transported to the vicinities of the substrate, in a deposition reactor, where chemical reactions take place that lead to the formation of a solid film on the substrate surfaces. This happens simultaneously with the downstream expulsion of the volatile byproducts. [25] Low reaction pressures (or low precursor partial pressures) are applied in order to avoid unwanted gas phase reactions, due to homogenous nucleation; which leads to poor quality surface coatings and wastage of the precursor. [25]

The chemistry of the reactions at the surface largely depends on the system as different reactions are required to achieve the wide range of coatings that can be applied by CVD. The most common reactions happening at the surface are: carburization, disproportionation, hydrolysis, nitridation, oxidation, reduction and thermal decomposition (pyrolysis). The CVD systems are usually designed such that the deposition only happens in the desired area and this is achieved by transporting the precursors in a non-reactive form and then activating the reaction in the substrate's vicinity. The activation is often achieved by an increase in temperature at the substrate, or even an ignition of plasma. [18] [26]

In the pioneering era of CVD, thermal decomposition (pyrolysis) of the precursor was the modus operandi; however, this limited the range of substrate materials that could be coated because pyrolysis often requires temperatures above 1000°C. Secondly, if the coating material and the substrate have desimilar coefficients of thermal expansion, then coating at a very high temperature could lead to the deposition of a layer that cannot withstand the stresses involved when the substrate is cooled post-process and hence cracks and peels-off under cooling. In the case of depositing tantalum from tantalum (V) chloride, pyrolysis would require a temperature above 2300K, which is detrimental to the structural integrity of most substrate materials. The use of reactive carrier gases such as hydrogen, in the case of tantalum CVD, provides an alternative reaction route that requires a lower temperature. In this case the required temperature is reduced to a range of 873K – 1300K. [25]

Originally, the main purpose of the carrier gases was to reduce the partial pressure of the precursor species to prevent gas phase depositions due to homogeneous nucleation, and to assist the flow. For this reason carrier gases were traditionally inert gases such as argon and helium. [18] The use of reactive carrier gases such as hydrogen for reduction and ammonia as a nitrogen source, is borne of a need to optimise the CVD systems either by lowering the reaction temperature or by reducing the number of process steps, respectively.

The general schematic for any CVD process and a description of the steps involved is shown in Figure 8. The steps are numbered from 1 - 7 showing the sequence of events that lead to a surface coating. [18, 24, 27]

1) Transport of the reactant gases to a region close to the surface of the substrate by forced flow (Convection).
2) Diffusion of the reactants through the boundary layer to reach the surface of the substrate; and, often, gas phase chemical reactions to form intermediates which are the true deposition precursors.

3) Adsorption of the reactants, or intermediates, onto the substrate surface, and surface migration (diffusion) of the reacting species so as to come into closer alignment with each other.
4) Heterogeneous deposition reaction and the integration of coating atoms into the growing crystalline surface. Formation of byproducts.
5) Desorption of the byproducts from the surface.
6) Diffusion of the desorbed byproducts through the boundary layer to the bulk gas.
7) Convective transport of the gaseous byproducts away from the reaction environment as exhaust.

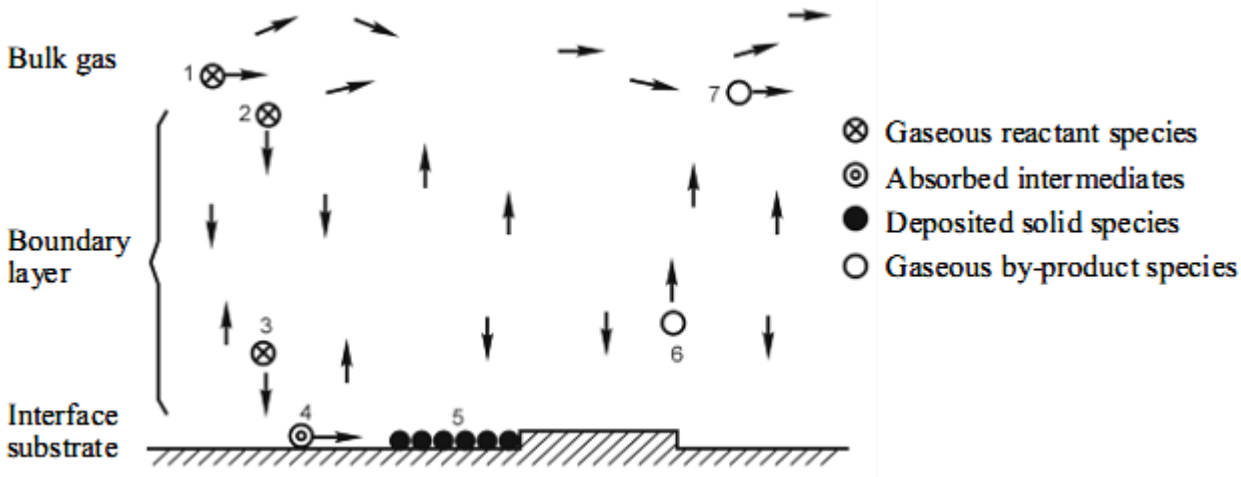

Figure 8: A CVD model [24]

3.2 Classification of the CVD Process

CVD processes can be classified based on the process parameters applied to achieve the desired deposition. These parameters are: Temperature, Pressure, Wall or Substrate, Precursor nature, Depositing time, Gas flow state and Activation manner.

CVD precursors can either be inorganic or metal-organic (MOCVD). Inorganic precursors, usually halides, are most commonly used. Metal-organic precursors are used either to lower the required deposition temperature or to achieve carbide coatings.

High temperature CVD is usually carried out at temperatures close to 1000 ^{O}C, and is the most commonly used, unless the substrate material cannot withstand these temperatures. Low temperature CVD is carried out at around 300^{O}C and is common in applications such as making semiconductors because the substrate is usually a surface of a plastic material that cannot withstand relatively high temperatures. Ultra-high temperature CVD involves temperatures in the range of 1750 - 1900 ^{O}C and is used in the production of refractory metals and single crystals.

There are three categories of pressure governed CVD processes namely: Atmospheric CVD, Low-pressure CVD and Ultra-vacuum CVD. Atmospheric CVD takes place at atmospheric pressure; low-pressure CVD at pressures less than (or around) 1 Torr and ultra-vacuum CVD at 10^{-3} Torr.

CVD processes can also be categorized as cold-wall or hot-wall processes. In Cold-wall processes the reactor wall is left unheated and only the substrate is heated (i.e. inductively or resistively). Deposition happens mainly on the hot substrate in preference to the cold reactor wall. Hot-wall reactors involve heating the entire reaction chamber by the use of an encompassing furnace. In this case, deposition also happens on the reactor/ chamber's walls.

CVD processes can also be classified as continuous, discontinuous or pulsed; all analogous to continuous, batch or fed-batch reaction systems, respectively.

A CVD system can also be categorized as closed or open depending in whether the reactants flow through once (open) or are continuously recycled (together with the products) to the reaction chamber to be reused.

The mode of activating the deposition reaction can also be used to categorize a CVD system. The most relevant, in this case, is thermal activation which is most commonly achieved by using a furnace (resistance heating). Radio frequency heating and infrared heating can also be used for thermal activation. Other forms of activation include the use of plasma (plasma-enhanced CVD) and lasers (laser induced CVD). Both these forms of activation are commonly used to lower the required deposition temperature. [24, 27]

Figure 9 provides an overview of the classification of CVD methods.

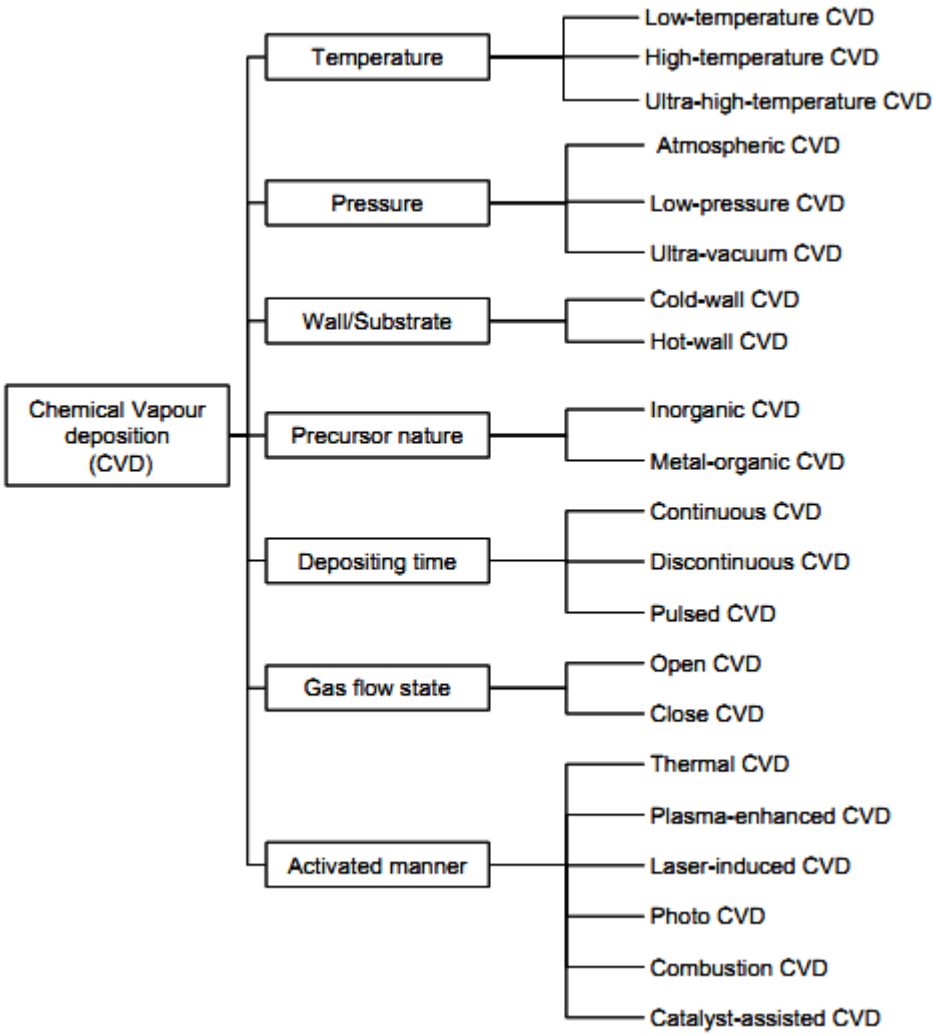

Figure 9: Classification of CVD processes. [24]

3.3 CVD in Flow reactors (Tubular Reactor perspective)

The aim of this project is to study the CVD of tantalum in long narrow channels for the purpose of applying the methods to the coating of heat exchangers. For this reason long narrow stainless steel tubes are used as the primary substrate in this project in order to physically model the reactor conditions. Stainless steel (AISI 316) Swagelok® tubes of 10mm internal diameter, 12mm outside diameter and 4.5m - 6m length are used.

In order to determine and explain the effects of the different process parameters on the deposition rate, it is important to study the conditions under which the deposition happens so as to have a full understanding of how the reaction parameters affect the reaction environment and therefore the deposition rate.

CVD in a tubular reactor is carried out by flowing the reactants through the tube, by the use of a vacuum pump. In this way, the internal surface of the tube is the substrate. The aforementioned

processes, described in Figure 8, then happen simultaneously at any given position inside the tube. Figure 10 shows a simple illustration of tantalum CVD in a tubular reactor while using $TaCl_5$ as a precursor and H_2 as a reducing agent.

$$TaCl_5 + \frac{5}{2}H_2 \rightarrow Ta + 5HCl \qquad \text{Equation 1}$$

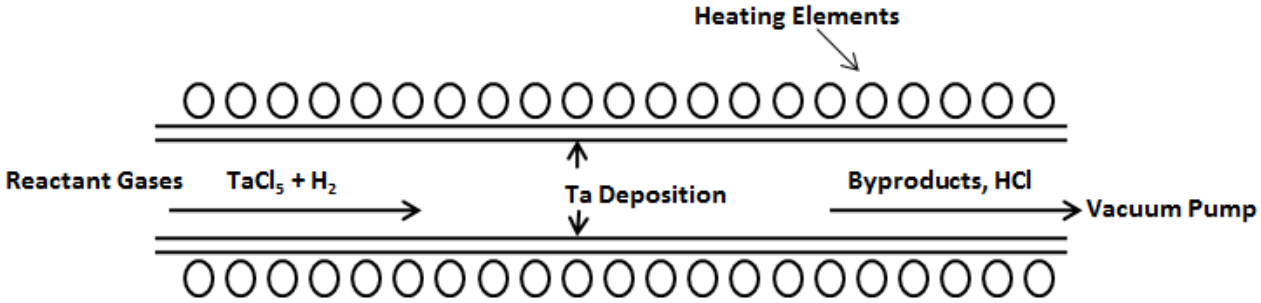

Figure 10: Illustration of tantalum CVD in a tubular reactor [27]

3.3.1 Flow Regime

The flow regime of a fluid is determined by calculating its Reynolds number. The Reynolds number is a dimensionless quantity that measures the ratio of inertial forces to viscous forces in a flow system. Larger inertial forces lead to a high Reynolds number and hence turbulent flow; while lower Reynolds numbers imply the dominance of viscous forces and therefore Laminar flow. Reynolds number can be represented as:

$$\mathrm{Re} = \frac{\rho \cdot u \cdot d}{\mu} \qquad \text{Equation 2}$$

Where: u is the velocity of the gas
ρ is the mass density
d is the tube diameter
μ is the dynamic viscosity of the fluid

The flow is said to be Laminar (parabolic) when Re < 2000, Transient for 2000 < Re < 4000 and Turbulent when Re > 4000.

Gas flow is generally laminar in tube reactor CVD applications because the gases are of low density; the tubes are usually thin in diameter and lower velocities ensure longer residence time. [18]

3.3.2 Velocity Profile

In laminar flow, the velocity of the fluid at the inner surface of the tube wall is essentially zero.[28] The velocity then gradually increases towards the centre of the tube until the maximum is reached,

at the axis of rotation. The region of lower flow acts as a boundary layer between the central core flow (bulk flow) and the tube's wall (CVD substrate). The boundary layer gradually increases in thickness from the inlet of the tube, in the direction of flow, until the flow stabilizes. In CVD applications, reactants have to diffuse through this boundary layer to reach the substrate (tube wall) and likewise, gaseous byproducts have to diffuse through it in order to be eliminated by the bulk gas flow.

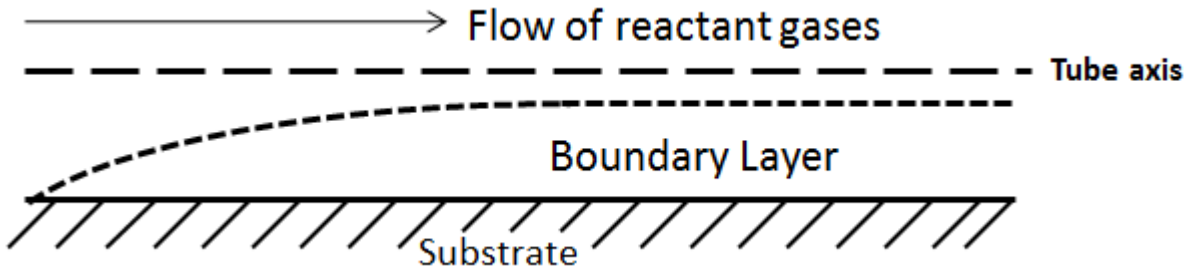

Figure 11: Illustration of the Boundary layer [18, 27]

The thickness of the boundary layer can be expressed in terms of the Reynolds number and distance down the tube:

$$\text{Thickness}, \delta = \sqrt{\frac{x}{Re}} = \sqrt{\frac{x \cdot \mu}{\rho \cdot u \cdot d}} \qquad \text{where} \quad \text{Re} = \frac{\rho \cdot u \cdot d}{\mu} \qquad \text{Equation 3}$$

From this equation, it can be seen that the boundary layer is thicker further down the tube, and when the gas velocity is lower.

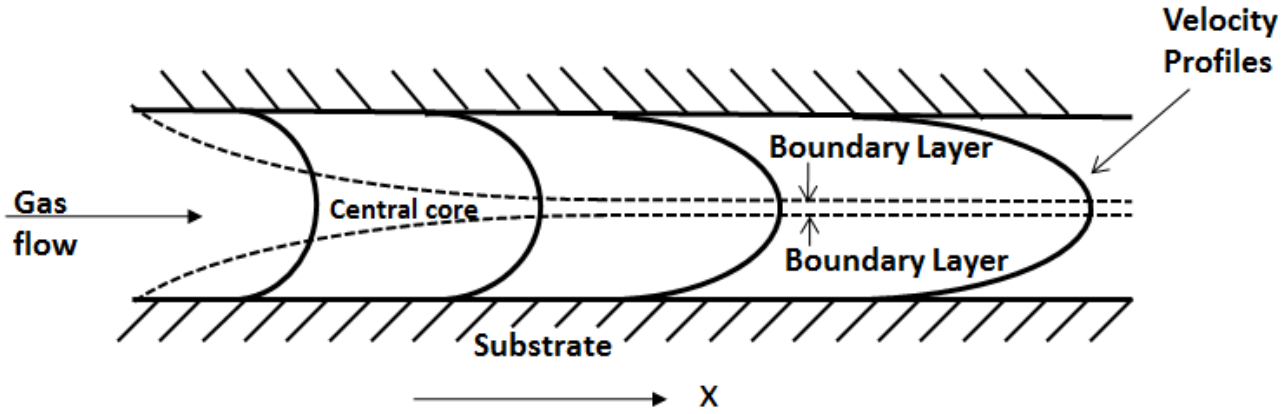

Figure 12: An Illustration of the Velocity Profile along the Tube [9, 18, 27]

The above diagram illustrates the velocity gradient from the high velocity bulk flow, nearer to the centre axis of the tube, to the zero velocity region, closer to the surface of the tube. It can also be seen that flow profile becomes more parabolic as the distance down the tube increases.

3.3.3 Temperature Profile

When the CVD gas mixture enters the tube, the gas temperature rises rapidly due to contact with the hot tube walls. As a result, a temperature gradient is formed such that the gas temperature is higher

towards the walls of the tube than it is at the axis. The mean gas temperature increases with distance, in the direction of the flow, resulting in a temperature boundary layer quite similar to the velocity boundary layer.

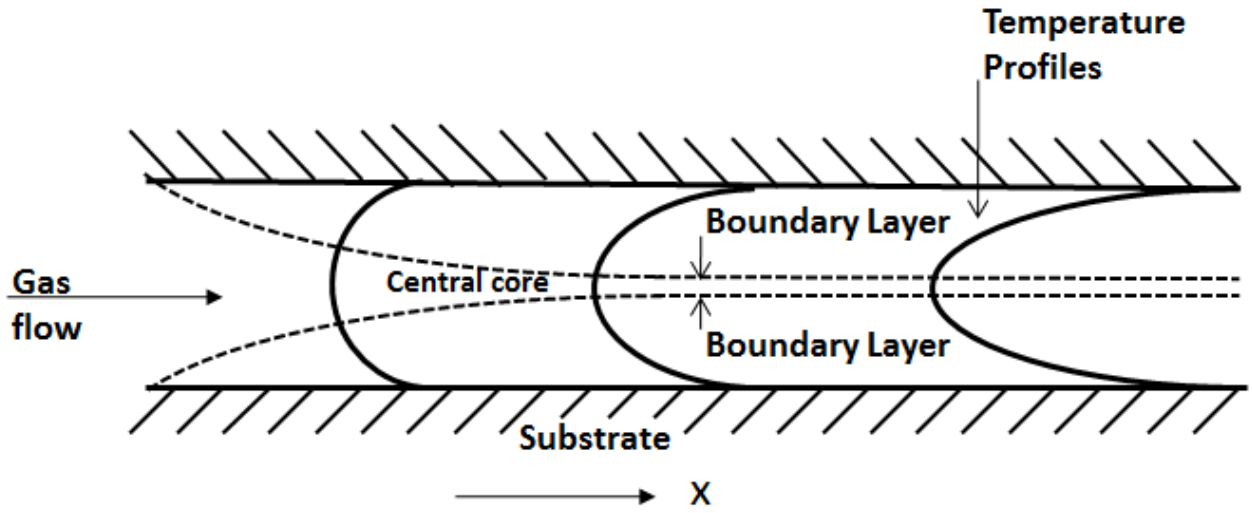

Figure 13: An Illustration of the Temperature Profile along the Tube [9, 18, 27]

3.3.4 Gas Concentration Profile

The reactant gas concentration profile is due to the fact that the original mixture is depleted of the precursor and the reducing carrier gas while the byproduct concentration increases downstream. In this case, the $TaCl_5$ and H_2 get depleted while the HCl concentration increases. Since most of the HCl is formed at the tube surface, as a results of the deposition reaction, its concentration will be greater in the regions closer to the tube wall than in the bulk flow. As a result, a boundary layer between the reactant rich bulk flow and the substrate is formed, and this increases in thickness with the distance down the tube.

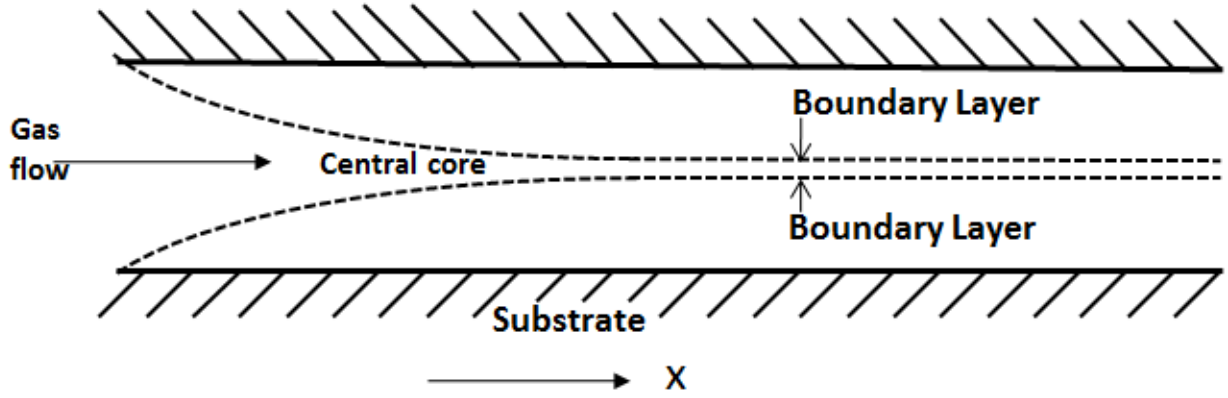

Figure 14: Illustration of the Concentration boundary layer along the Tube [9, 18, 27]

3.4 Factors affecting the deposition rate

The CVD model in Figure 8 shows the seven main steps that lead to a deposition, and any of them can be the rate limiting step. However there are five major types of control discussed in literature, which are: Thermodynamic control, Nucleation control, homogeneous reaction control, Surface kinetics control and mass transport control. [9, 18, 24, 26]

3.4.1 Thermodynamic control

A thermodynamics controlled system is also sometimes referred to as a feed rate controlled system because the deposition rate is equal to the precursor feed rate. This is observed in systems where the temperature is high but the precursor supply is limited e.g. low precursor flow rate or low precursor partial pressure. In such a situation, both mass transport and surface kinetics are fast and quickly deplete the bulk gas of the precursor until the thermodynamic yield is reached. [9, 26]

3.4.2 Nucleation Control, and Homogeneous reaction Control

Under conditions of low supersaturation of the precursor, the deposition rate can be controlled by the nucleation process.

Homogeneous reaction control is observed when the deposition rate is controlled by the amount of a key species in the gas phase. This could be the case if the 'true precursor' (surface actives species) is a product of a gas phase reaction or if one of the products of the reaction actually inhibits further deposition. [26]

3.4.3 Mass Transport control

Mass transport through the boundary layer is dependent on the thickness of the boundary layer and the diffusion coefficients. A thick boundary layer and low diffusion coefficients imply slower mass transport through the boundary layer as opposed to a thin boundary layer and high diffusion coefficients. High pressure combined with high temperature in a tube CVD system leads to a mass transport controlled reaction. The high pressure directly implies low diffusion coefficients and slow gas velocities, resulting into a thick boundary layer. In such a system, the high wall temperature implies that the precursor reacts quickly and instantly upon reaching the surface of the tube; however, the reactant concentration close to the surface is low due to slow mass transport as a result of the thick boundary layer and low diffusion coefficients. If the temperature is high enough in such a system, there is a possibility of having gas phase reactions which produce the deposition material within the bulk flow, but without contributing to the growth of the surface coating. While this is exploited in the production of fine powders, it is a waste of material if the goal is to coat the wall of the tube, and can also lead to a porous and flaky coating. [18, 24]

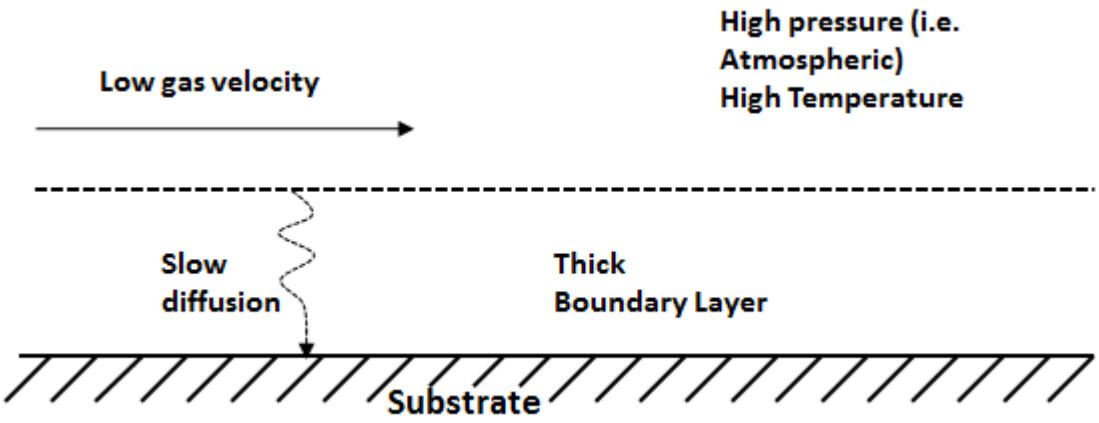

Figure 15: Mass transport limited system [18]

3.4.4 Surface Kinetics control

A low pressure and low temperature CVD system results in a reaction whose rate is governed by the surface kinetics. Low pressure in a tube CVD reactor directly implies higher gas velocity, thus a thin boundary layer; and higher diffusion coefficients. Such conditions mean that diffusion of the reactants through the boundary layer happens rather quickly as the diffusion is fast and the layer is thin. Low temperature at the surface of the tube results in slower reaction kinetics while leaving the substrate area rich in reactant concentration. This shows that the rate of reaction is being limited by the fact that the precursor is converted at a slower rate than it is supplied to the substrate, hence a deposition rate controlled by surface reaction kinetics. [18, 27]

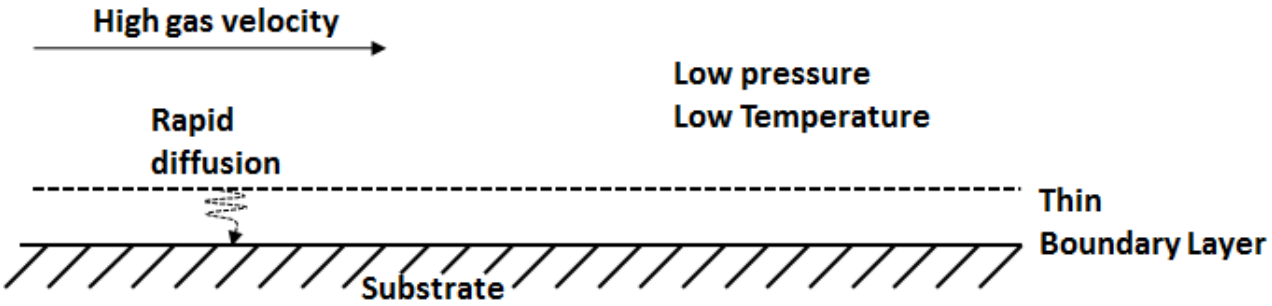

Figure 16: Reaction Limited by Surface kinetics [18]

3.4.5 Determining the rate limiting Step based on the reaction Temperature

The rate limiting step can easily be determined or controlled by adjusting the system's temperature without bothering with the pressure. High temperatures lead to very fast reactions at the surface of the tube hence making the diffusion step the rate limiting step. Low temperatures lead to the vice versa. The graph below illustrates this in a CVD system for the deposition of silicon using various precursor compounds.

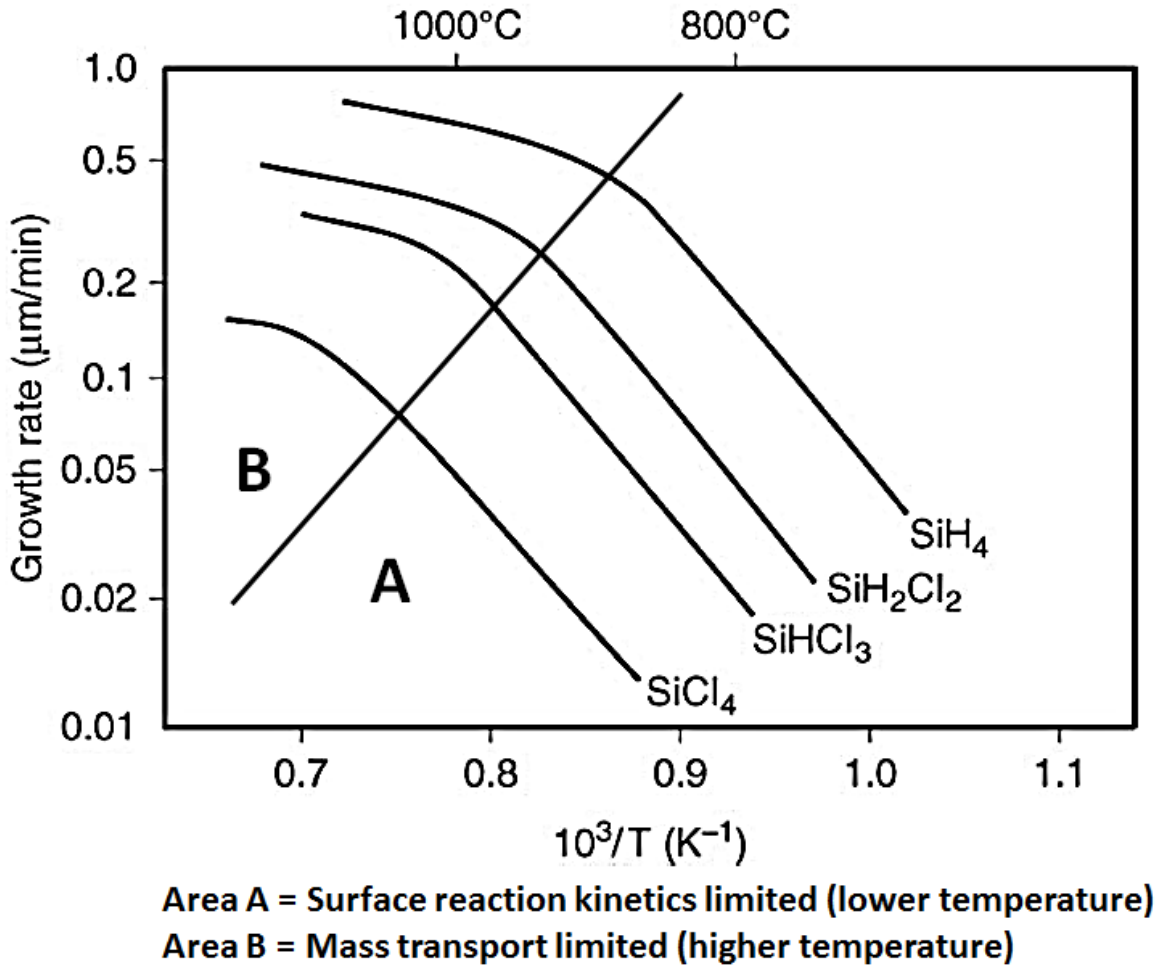

Figure 17: Arrhenius Plot for the Silicon Deposition using various Precursors [18, 26]

In region A of Figure 17– i.e. lower temperature –, the reaction rate at the surface is relatively slow and hence the rate of the deposition process is controlled by surface reaction kinetics. In this situation, the reactants can be carried swiftly through the boundary layer to the reaction surface and there is no concentration gradient in the boundary layer i.e. the concentration at the surface is identical to that of the bulk gas. The growth rate is this region increases rapidly with an increase in temperature because of the dependence of the reaction rate constant on temperature. [18, 24]

In region B – i.e. High temperature – the reaction is fast at the surface and the rate limiting step is the mass transport process from the bulk flow to the substrate. As a result of this, there is a steep concentration gradient in the boundary layer due to the fact that the surface is starved of reactants. In this section, the growth rate of the coating material, on the substrate, is directly proportional to the partial pressure of the reactant species in the carrier gas, and inversely proportional to the total pressure of the system.

In this region it can also be seen that the lighter (lower molecular weight) precursor species give higher deposition rates because they have higher diffusion coefficients and hence diffuse faster.

A curved transition region exists between sections A and B (Figure 17) where both mass transport and surface reaction kinetics play a significant role in the deposition rate. The maximum points on the B side of the graph represent the temperature at which gas phase precipitation begins to occur;

which leads to a decrease in the partial pressure of the reactant gas and hence also a decrease in deposition rates at the surface. [18, 24]

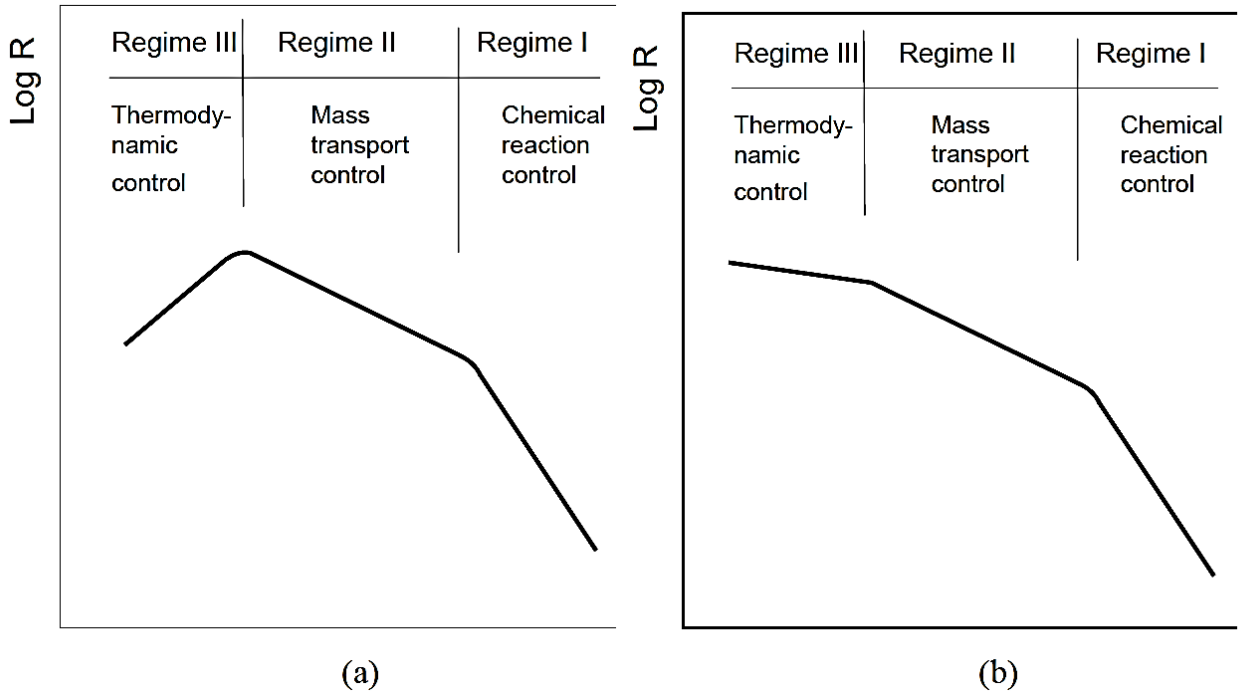

(a) Exothermic Reaction ***(b) Endothermic Reaction***

Figure 18: Arrhenius Plot (Log R Vs I/T) showing the Temperature Dependence of the deposition rate [24]

At very high temperatures (>1650 ^{0}C) the deposition process is controlled by the system's thermodynamics and is directly linked to the Gibbs free energy of the system. As the temperatures increase, the value for Gibbs free energy of the system increases (becomes less negative) for an exothermic reaction. This directly implies that the driving force for the reaction, which leads to the growth of the coating, decreases and hence the coatings growth rate decreases too.

For an endothermic reaction, increasing temperature makes the Gibbs free energy more negative which leads to the formation of the coating material in the bulk gas phase, away from the surface. The material formed in the bulk gas does not contribute to the thickness of the coating at the surface and hence leads to decreased growth rate of the coating. Figure 18 illustrates the three control regimes. [24]

3.4.6 Pressure limited System

The diffusibility of a gas is inversely proportional to its pressure. Due to this, lower pressure favours faster mass transport of reactants, through the boundary layer, to the substrate and transport of by products to the bulk flow. Thus, the effect of mass transfer variables is trivial at lower pressure and more significant at higher pressure. According to *Pierson (1999)* [18], reducing the pressure in a tube reactor from 760 Torr to 1 Torr can increase the diffusive transport of both reactants and by-products

by more than 100 fold. Thus, surface reaction kinetics is the rate limiting step in a lower pressure system since diffusion of the gaseous species happens swiftly.
However, it is emphasized that reducing the pressure of the system by decreasing the partial pressure of the reactant gas can be detrimental to the deposition rate because the rate of reaction at the surface (substrate) is directly proportional to the partial pressure of the reactant gas, in a first order reaction system. It is therefore advised to reduce the pressure at the expense of the carrier gas. [18]
Figure 19 shows the dependence of the deposition rate on the gas velocity. It is important to note that the gas flow velocity is inversely proportional to the system pressure for tubular reactors; hence the graph could also be seen as a deposition rate Vs 1/pressure.

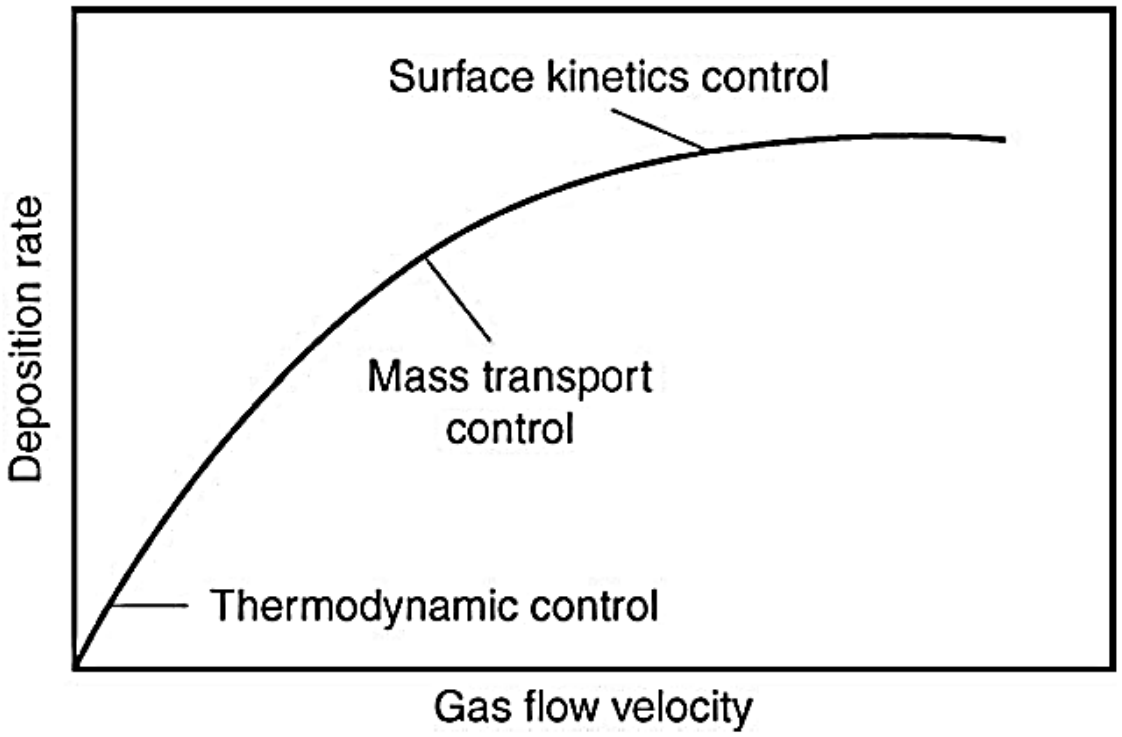

Figure 19: Effect of deposition rate on the gas flow velocity [26]

3.5 General CVD Considerations

3.5.1 Adhesion

Most CVD processes are done as surface modification techniques aimed at producing coatings that adhere seamlessly to the substrate. Several factors can affect the degree of adhesion achieved between coating and substrate and most of these are revised in this section:

In order to achieve good adherent coatings, it is important to minimize the intrinsic stresses at the interface of the coating and the substrate. Such stresses can be caused by the deposition conditions or due to a mismatch of thermal expansion coefficients between the coating and the substrate. A mismatch of thermal expansions would lead to different changes in volume upon cooling which could lead to cracks. If the required coating has a significantly different thermal expansion coefficient to the substrate then a ductile buffer layer of another material (e.g. copper) could be applied between the substrate and the final coating of the desired material. [26]

The degree of adhesion of the coating to the substrate can sometimes depend on the formation of intermetallic compounds at the interface. Some intermetallic compounds are brittle and the formation thereof has to be limited to a thin layer in order to minimize crack formation and propagation. Buffer layers can also be used to achieve a more ductile interface in this situation. [26]

Homogenous nucleation can lead to vapour phase depositions that integrate themselves into the coating to produce a powdery/ flaky coating with high porosity. Such coatings are not synonymous with high mechanical strength and should be avoided. Homogenous nucleation can be avoided by lowering the precursor concentration (avoiding saturation) and by lowering the reaction driving force. [18, 26, 27]

Several CVD techniques use hydrogen gas as part of the substrate cleaning procedure (oxide layer reduction) and some metals are well known to absorb hydrogen. [22] If the coating process is performed at a temperature where the hydrogen is liberated, poor adhesion will be achieved. In other cases where hydrogen is part of the deposition process care should be taken to extract dissolved hydrogen, prior to cooling, by applying high vacuum lest the hydrogen is liberated with in the material leading to internal stresses. [26, 29]

Other more obvious factors that affect the adhesion of the coating to the substrate are the presence of an oxide layer on the substrate surface, or the presence of other contaminants such as oils and grease. The detrimental effects of these can be eliminated by applying an appropriate cleaning procedure that respects the chemical properties of the substrate. [26]

3.5.2 System Design

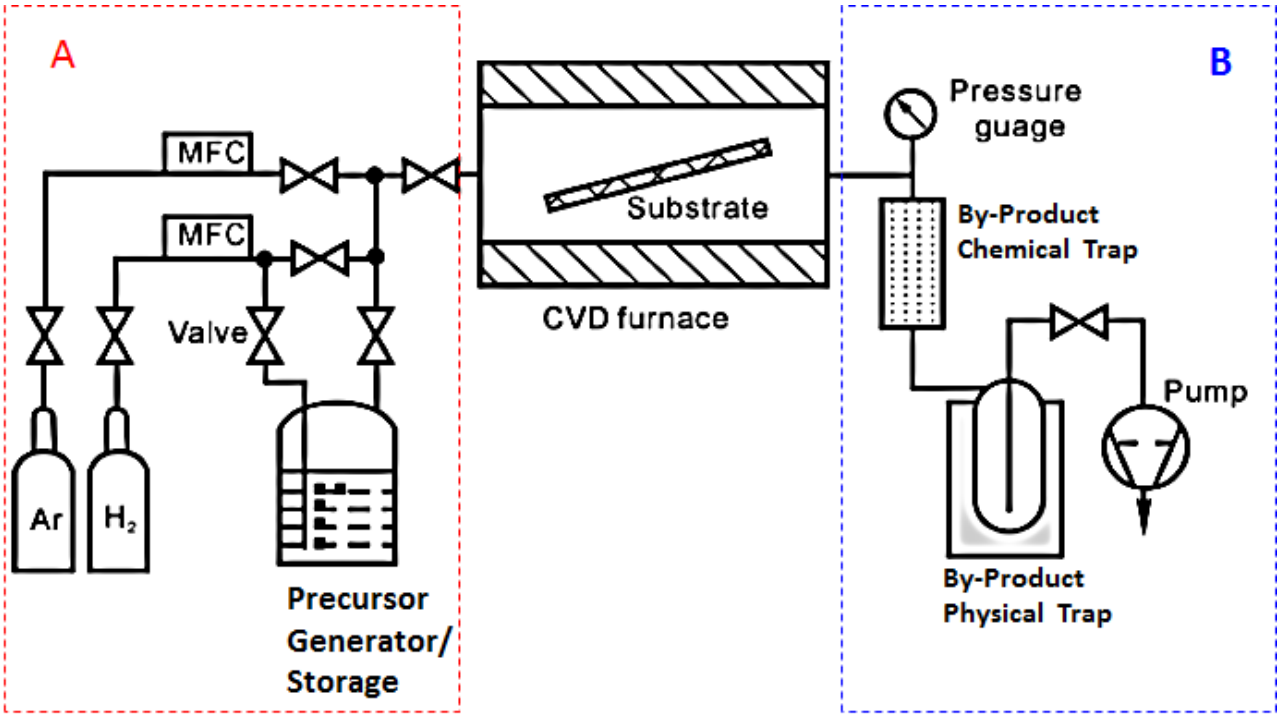

Figure 20: A general CVD System. (Adapted Diagram; MFC – Mass Flow Controller) [24]

The specific features of any given CVD system always depend on its purpose, economy and process tolerances. These can be summed up as: [26]

- Required purity of the deposit
- Shape and size of the substrate
- The acceptable leak rate of air into the system
- Chemical and physical properties of the reactants

However despite the differences found between systems, there is a general format that all CVD systems follow. They all have a CVD furnace/reactor, a gas supply area and an exhaust handling area.

The gas supply area meters and provides the required amounts of each process gas. It quite often contains valves, flow meters, pressure gauges and a precursor generator or bubbler. The pipes leading from this section to the CVD furnace are usually heated to keep the precursor volatile and to preheat the gases prior to entering the furnace/ reactor. The gas supply area is labelled A in Figure 20.

The CVD furnace/reactor is the focal point of the system and is designed to hold the substrate in the best orientation required for coating. Sometimes the substrate is rotated within the furnace to achieve a uniform coating.

The exhaust from CVD systems is usually reactive, poisonous and harmful to the environment, and has to be dealt with prior to venting. This, combined with pressure stabilization and a pumping unit, are the main purposes of the exhaust area of a CVD system. The exhaust cleaning can be achieved by chemical scrubbing and/or by using liquid nitrogen cold traps. A vacuum pump is usually applied as the last step to provide the required suction; and sometimes liquid ring pumps with chemical agents are used to achieve a last step of scrubbing prior to venting.

3.6 CVD of Tantalum in Literature

The CVD of tantalum by thermal decomposition of tantalum (V) chloride at 2000 ^{O}C is reported in work dating back to 1934. The same review reports that the obtained deposits were soft and ductile, and that the deposition temperature could be lowered by thermal decomposition of the penta-bromide and penta-iodide. [30]

Work, from 1905 and 1907, on the CVD of tantalum by reduction of the penta-chloride in a hydrogen atmosphere is also mentioned. It is claimed that hydrogen free tantalum deposits could be obtained by operating between 1200 ^{O}C - 1450 ^{O}C, and that deposits obtained below 1200 ^{O}C were brittle unless rendered ductile by vacuum annealing. With respect to hydrogen reduction of the halides, no technical advantage was gained by using the penta-bromide or penta-iodide, while also being more expensive to produce than the chloride that was synthesized by a direct reaction between Ta metal chips and chlorine gas at temperatures between 200 - 300 ^{O}C. The reduction process is reported to set in at 600 ^{O}C where it is very slow, and rapidly increases in rate with temperature. [30] [31]

C. F. Powell goes ahead to mention the occurrence of non-adhesive powdery deposits at higher temperatures and suggests that it is caused by reduction of the chloride at a considerable distance from the surface due to super sufficient heating. He sums up by stating that low flow rates favour higher efficiency (yield > 60%) and give dark uneven deposits on large objects; while higher (more turbulent) gas flow rates give more uniform deposits but at lower efficiency (yield < 25%). [30, 31]

Stolz and Heiber [32] also study the CVD of tantalum using the chloride reduction method in order to achieve corrosion resistant coatings. They state that such coatings need to be dense and pin hole free and that the best results are achieved at pressures between 10 – 150 mbar. They also mention that in order to achieve the high technical purity required for corrosion resistant coatings (>99.5%), the air leak rate into the system must be below 5 x 10^{-3} mbar l s^{-1} and the piping system that must be resistant to $TaCl_5$ (for example stainless steel). [32]

The use of tantalum (V) fluoride as a precursor is reported by *Ugolini et. al.* [33] for deposition on Si and SiO_2 at 400 ^{O}C.

Plasma-assisted CVD of tantalum from the reduction of tantalum (V) bromide is also reported by *Kaloyeros et. al.* [34] and *Chen et. al.* [35] for microelectronic structures where the substrate cannot tolerate high temperatures.

Most recent research on tantalum CVD has been focused on coating materials such as stainless steel and titanium to improve their biocompatibility for use as medical implants. [13, 36]

Other worthy mentions include:

- Work by *Suh et. al.* [7] and *R. A. Levy* [8] on plasma assisted CVD of Ta by $TaCl_5$ reduction for gun barrel protection.
- Work by *Park et. al.* [37] on the Preparation of tantalum nano-powders through reduction of $TaCl_5$.

In all the reviewed literature concerning Ta CVD by the reduction of a halide, the general stoichiometric equation is given as: [8, 29, 38, 39]

$$TaX_5 + \frac{5}{2}H_2 \rightarrow Ta + 5HX \qquad \text{Equation 4}$$

Where '*X*' is the halogen species F, Cl, Br or I. [8, 29, 38, 39]

3.6.1 Precursor Considerations

The choice of precursor quite often plays a very significant role in the design of a CVD system. It is always desirable to have a precursor that has a high vapor pressure, for ease of transport, and is easily deposited once the substrate is reached. However these considerations are only worth taking if the field of choice achieves the desired quality of coating and requires reasonable containment measures.

Organo-metallic precursors are not considered in the production of high purity tantalum deposits because of tantalums affinity towards oxygen, carbon and nitrogen. Such deposits would contain levels of carbon that could be detrimental to desired properties such as ductility and corrosion resistance. [25]

Using tantalum (V) fluoride as a precursor, although tried, is unrealistic due to the difficulties that arise when dealing with the process byproducts. Hydrogen fluoride gas is very reactive and very difficult to contain.

This only leaves two realistic precursor options to choose from: tantalum (V) chloride and tantalum (V) bromide.

Levy [8] studied the properties of TaF_5, $TaCl_5$ and $TaBr_5$, and produced data showing that the halides have vapour pressures in the order of TaF_5 > $TaCl_5$ > $TaBr_5$ while the order is reversed when

considering the ease of deposition. Figure 21, Figure 22 and Figure 23 show that TaF_5 is the most volatile, however, also the most energy requiring to deposit. The same figures show that the bromide and chloride require comparable amounts of energy to deposit however the chloride gains advantage in being much more volatile. With all these factors taken into consideration, using $TaCl_5$ as precursor is the most prudent choice if the substrate can handle the temperature required for deposition. [8, 29]

Table 4: Properties of the halides of tantalum [8]

Precursors	Melting point (°C)	Boiling point (°C)	Heat of Formation (ΔHf, kcal/mol)
TaF_5	97	230	-455
$TaCl_5$	216	242	-205
$TaBr_5$	265	349	-143

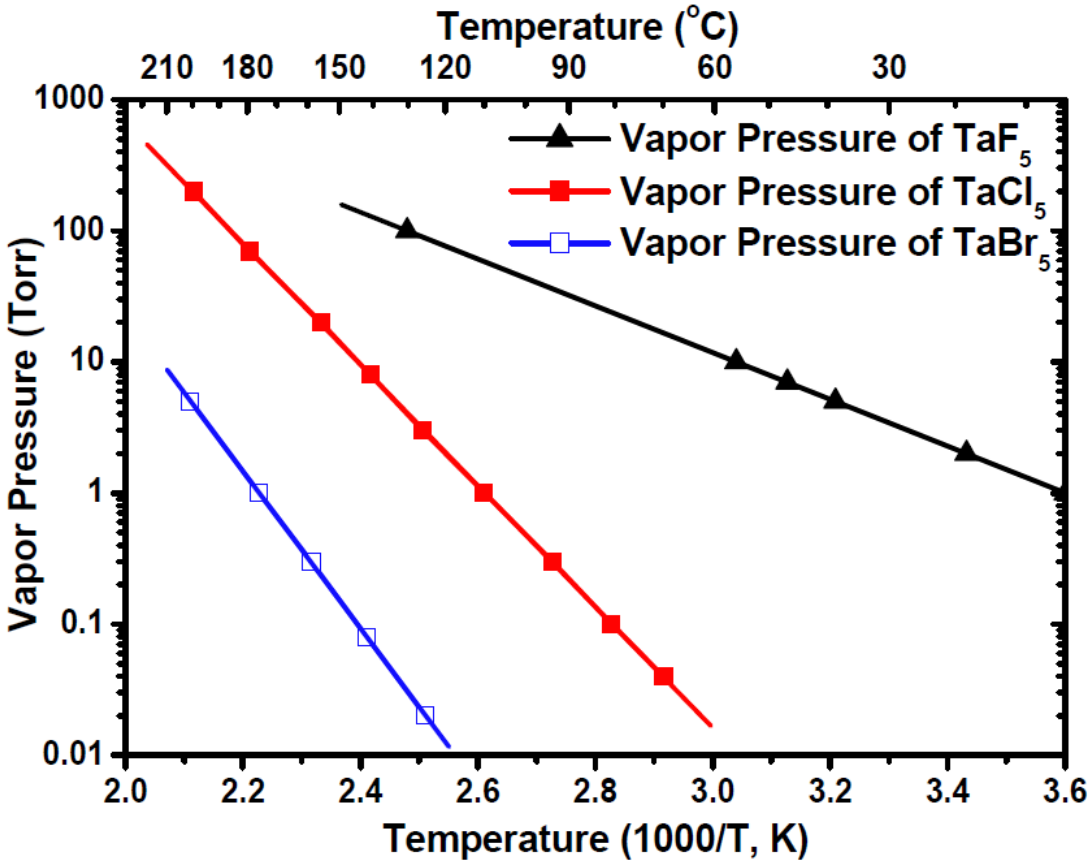

Figure 21: Vapour pressures of TaF_5, $TaCl_5$ and $TaBr_5$ [8]

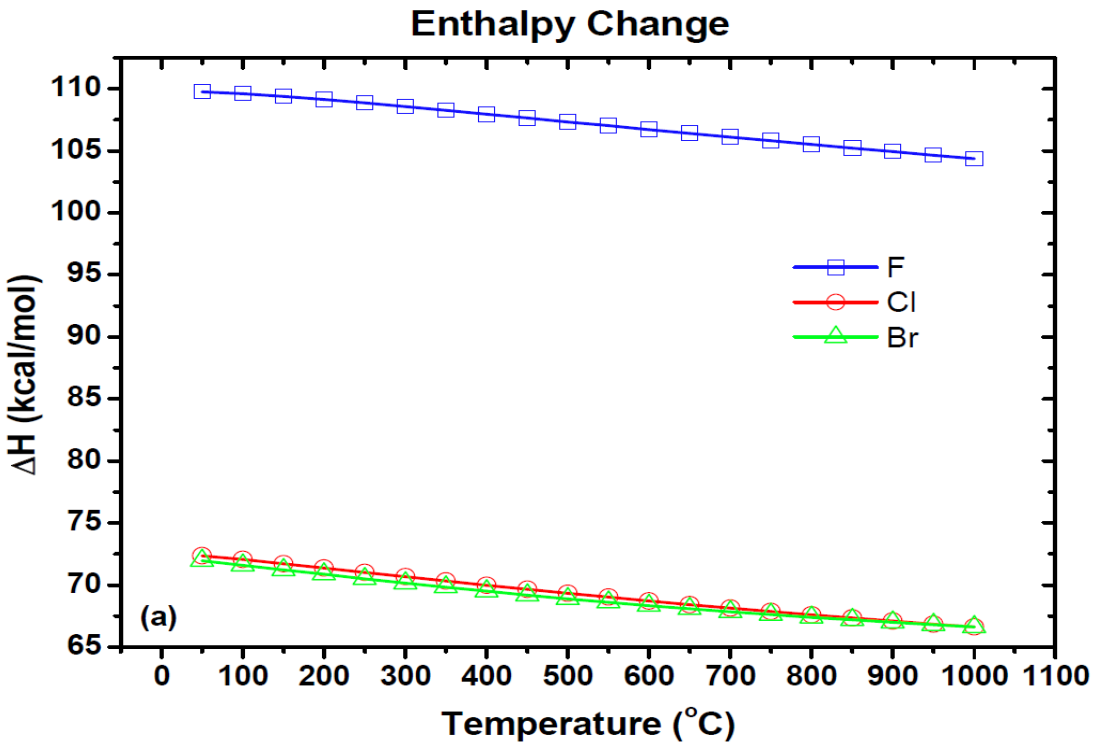

Figure 22: Enthalpy change of deposition reaction (according to Equation 4) for TaF_5, $TaCl_5$ and $TaBr_5$ [8]

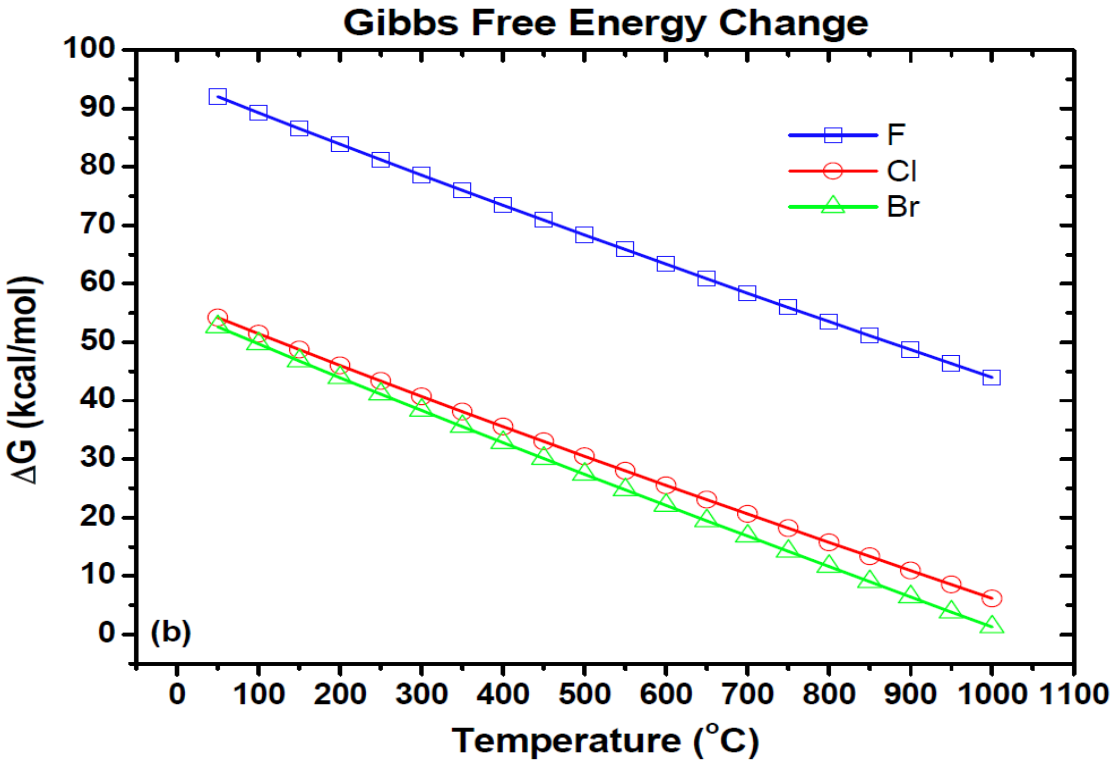

Figure 23: Gibbs free energy change of deposition reaction (according to Equation 4) for TaF_5, $TaCl_5$ and $TaBr_5$ [8]

3.6.2 Gas Oxidation States under CVD conditions (chlorides of tantalum – hydrogen System)

At approximately 600 ^{O}C, tantalum (V) chloride is reduced in a hydrogen atmosphere to form both tantalum and lower oxidation state chlorides. [31] It is therefore sensible to infer that at the higher temperatures required during CVD, the gas mixture is significantly different from what is fed into the reactors at lower temperature.

Eriksen [29] did thermodynamic calculations to determine the development of the gas mixture with temperature at 20 mbar and it was found that at 500K (227 ^{O}C) $TaCl_5$ is the dominant chloride species however; the lower chlorides ($TaCl_4$, $TaCl_3$ and $TaCl_2$) start to gain prominence at 800K (527 ^{O}C) and are the dominant species by 1100K (827^{O}C). This leads to a situation where the actual surface active species are a product of a gas phase reaction (or a series of gas phase reactions) between the precursor and hydrogen. The results from the study are shown in Figure 24, Figure 25 and Figure 26.

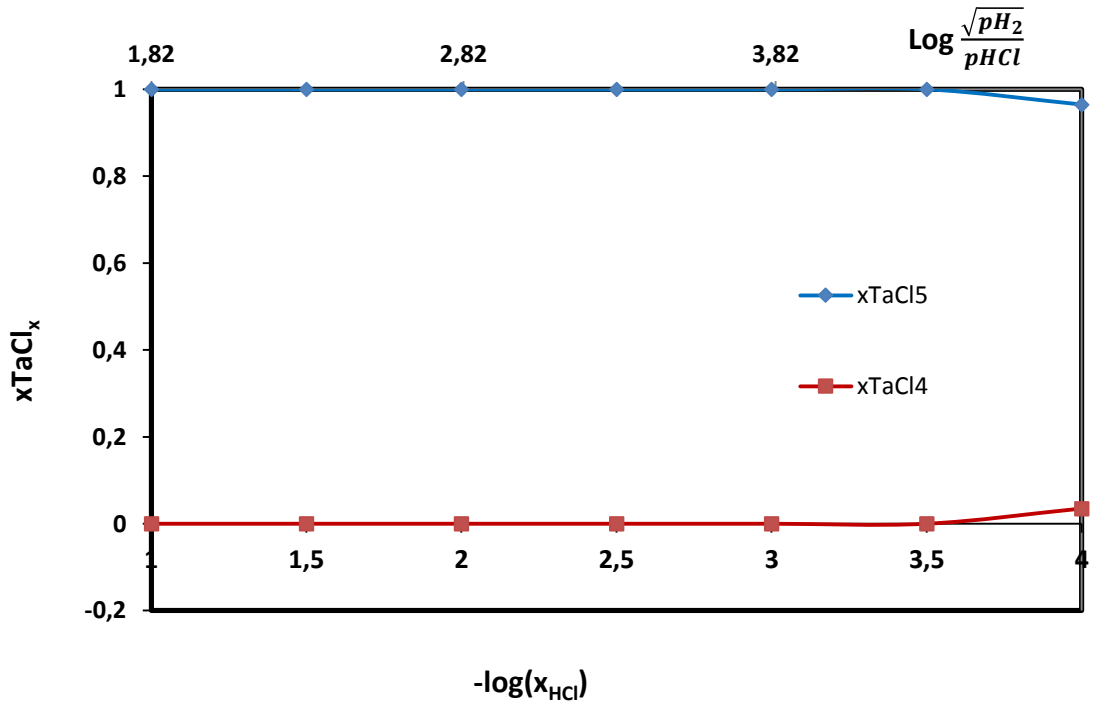

Figure 24: The relative abundance of tantalum chlorides at equilibrium at 20 mbar and 500K [29]

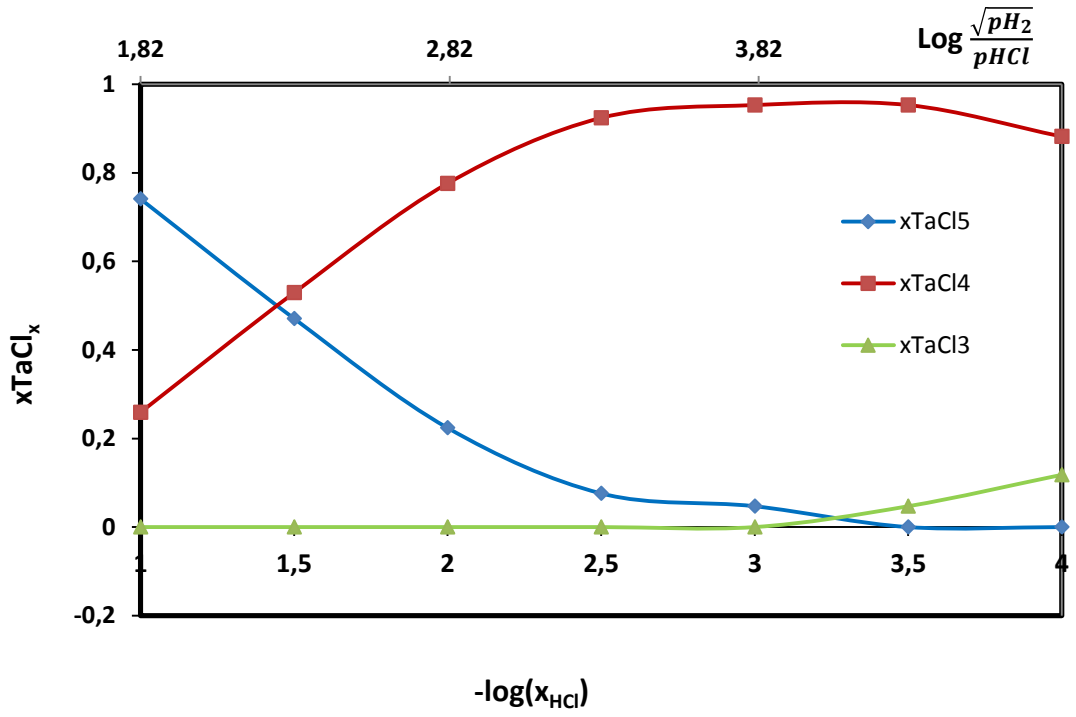

Figure 25: The relative abundance of tantalum chlorides at equilibrium at 20 mbar and 800K [29]

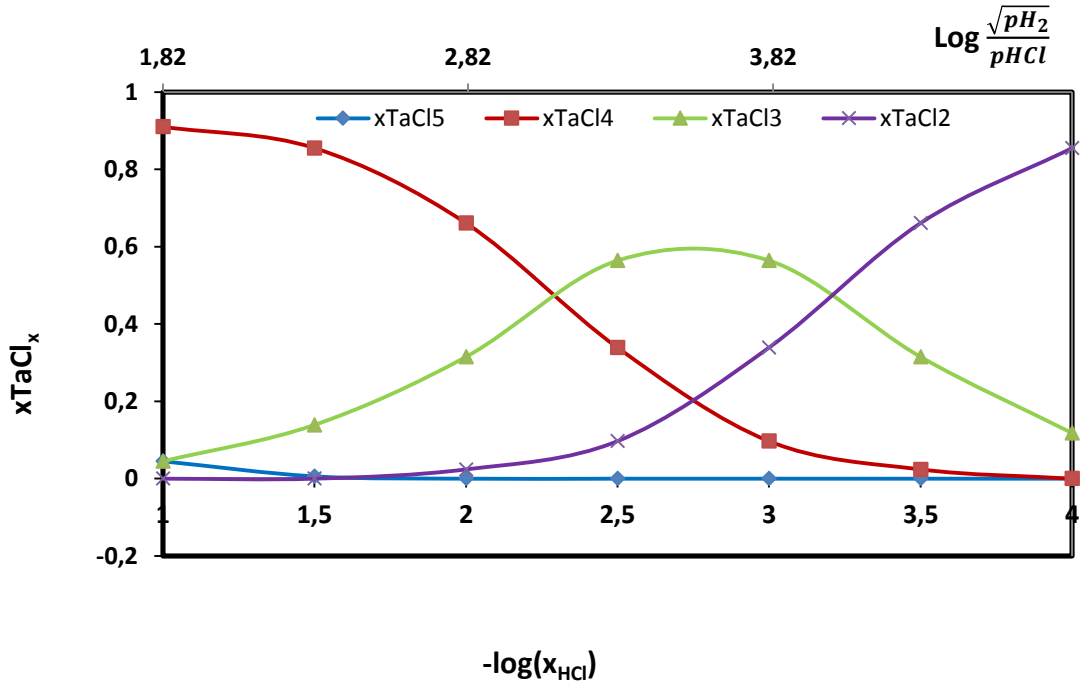

Figure 26: The relative abundance of tantalum chlorides at equilibrium at 20 mbar and 1100K [29]

4 MODELLING

4.1 Model Definition

A mathematical model is generally a set of equations that tries to describe a natural phenomenon or the behaviour of a system. Models are made to help further understand a system/ phenomenon by attempting to predict an output (behaviour) based on a known input (stimulus). A common example of the application of mathematical models is in weather forecasting.

There are many advantages to modelling, with the most obvious ones being that they help to better understand a system/phenomenon and they can help to save money by predicting unwanted outcomes thus enabling the user to avoid or work around such outcomes.

Regardless of their usefulness, all models have limitations because nature quite often involves more variables than can be computationally accounted for. Models therefore usually have ranges of validity out of which they gradually start to fail. With respect to this, model outputs are to be interpreted with such limitations taken into account in order to avoid error. An example of this is in the attempt to predict the velocity of an electron and its position. One uses Einstein's relativity theory to predict the speed of the electron while using quantum mechanics to predict its most likely position. The two models contradict each other when used vice versa but work with great accuracy when used properly.

4.2 Modelling the Chemical Vapour Deposition of tantalum

Figure 8 (on page 11) shows a schematic of the steps involved in a CVD process and any mathematical model for CVD has to be able to account for these steps as any of them could be the rate limiting/determining step. Since the model being developed is to describe a continuous CVD system, a steady state model has to be implemented. The overall result of this is a simulation tool that covers the entire CVD reactor as outlined:

1) The first part of the model describes the Thermal characteristics of the reactor i.e. Thermal radiation from the reactor wall to the substrate, thermal conduction in the substrate material and thermal conduction/convection of the gases.
2) The second part (which is coupled with the first) accounts for the flow of the gases in the system by forced convection as they are being heated.
3) The third part accounts for mass transport of the active species by diffusion, while taking into account the thermal and flow solutions from part 1 & 2.
4) The fourth part (coupled with part 3) accounts for the surface reaction phenomena and mass balances while also taking into account the solutions from parts 1 & 2.

The outlined model, technically described, is a Computational Fluid Dynamics (CFD) model coupled to surface-to-surface radiation, diffusion and reaction kinetics. The CFD module and the surface-to-surface radiation module are fully coupled together, and so are the mass transport and reaction kinetics modules. However the later coupling imports the solution of the former.

The entire model is implemented using propriety software called COMSOL MULTIPHYSICS®. The use of this software removes the necessity to write MATLAB® source code but does not remove the need of knowledge in the field of study. The user interfaces for the different sets of physics that are available in COMSOL® require a knowledge of the equations and solvers in the background. Furthermore due to the round nature of the system the model is implemented in a 2 dimensional axial symmetric geometry i.e. 2-D Axial Symmetry.

Sections 4.2.1 – 4.2.3 are dedicated to explaining the approach used within the software to solve the Mass, energy (thermal), and momentum transport.

4.2.1 Thermal Modelling

4.2.1.1 Surface to surface Radiation

The amount of energy emitted by a body, in the form of electromagnetic waves (photons), at a certain temperature is generally called thermal radiation. Black bodies emit as much energy as they absorb, however black body radiation is an idealized concept and is never met in practice; grey body radiation is most common and is generally characterized by an emissivity value. The emissivity is the fraction of energy emitted by a grey body compared to that of a black body at the same temperature. Hence a black body has an emissivity of 1 while the emissivity of a grey body will range between 0 – 1.
Based on the Stefan-Boltzmann law [28], the amount of energy emitted by a grey body at a given temperature is described as:

$$Flux = \varepsilon \cdot \sigma \cdot T^4 \qquad \left[J \cdot s^{-1} \cdot K^{-4}\right] \qquad \text{Equation 5}$$

Where:

ε is the emissivity, σ is the Stefan - Boltzmann constant *and* T is the temperature in kelvin.

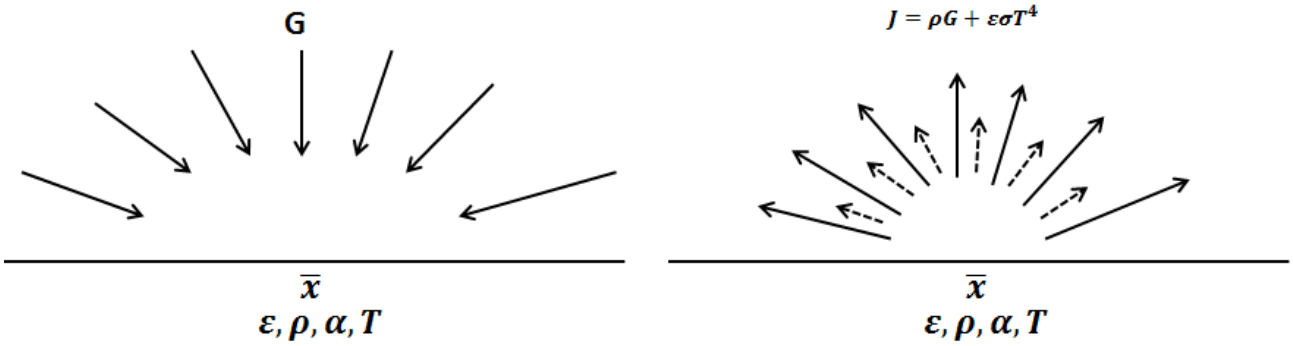

Figure 27: Illustration of radiation to and from a point $\bar{x}$. [40]

The above figure considers a hypothetical point 'x' with a reflectivity $\boldsymbol{\rho}$ and absorptivity $\boldsymbol{\alpha}$. The incoming flux is $\boldsymbol{G}$ and the total outgoing flux is the radiosity, $\boldsymbol{J}$. The total outgoing flux is the sum of the reflected radiation and the emitted radiation, the reflected radiation is the product of the incident flux and the reflectivity. This hypothetical situation is always true for transparent bodies.

$$J = \rho G + \varepsilon\sigma T^4 \qquad \text{Equation 6}$$

For opaque bodies, the absorptivity has to also be taken into consideration. Most opaque objects tend to also behave as ideal grey bodies; hence the absorptivity and emissivity are equal such that $\alpha = \varepsilon = 1 - \rho$.

Hence:

$$J = (1-\varepsilon)G + \varepsilon\sigma T^4 \qquad \text{Equation 7}$$

The net inward flux of the body, $\boldsymbol{q}$, is the difference between the incoming and outgoing radiation and is therefore given by:

$$q = G - J$$

$$q = G - (1-\varepsilon)G - \varepsilon\sigma T^4 = G(1-1+\varepsilon) - \varepsilon\sigma T^4 = \varepsilon G - \varepsilon\sigma T^4$$

$$q = \varepsilon(G - \sigma T^4) \qquad \text{Equation 8}$$

Comsol® uses Equation 8 as a radiation boundary condition.

Surface to surface radiation is relatively difficult to model because it includes radiation from both the ambient surroundings and other surfaces. In the case of a 2-D axial-symmetric geometry, Comsol® creates a virtual 3-D geometry from which it computes the irradiation and the view factors. The results of this are then evaluated using the 2-D integrals and presented as such.
For any given point on a surface, the irradiation flux can be generally expressed as:

$$G = G_m + F_{amb}\sigma T^4{}_{amb} \qquad \text{Equation 9}$$

Where

G is the total irradiation flux

G_m is the mututal radiation arriving from other surfaces in the geometry, *and*

F_{amb} is the ambient view factor

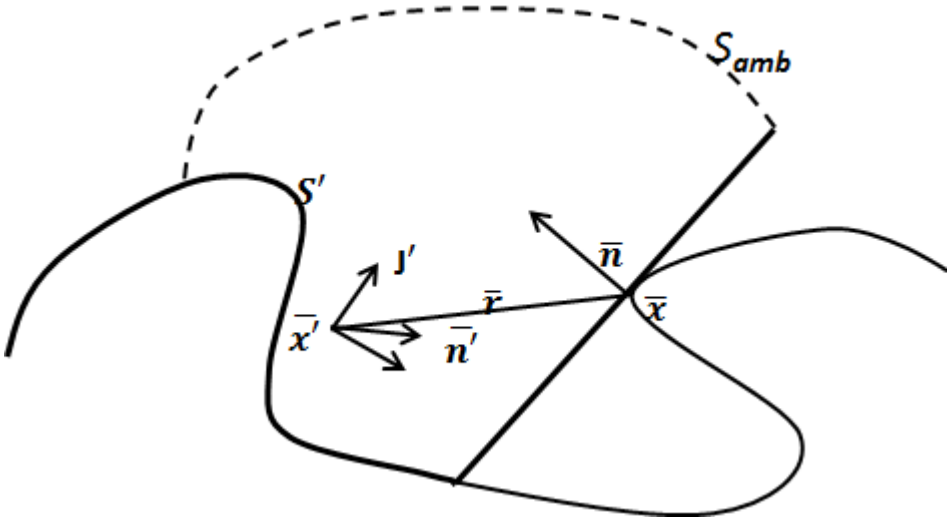

Figure 28: Example geometry for surface to surface radiation [40]

The geometry in Figure 28 shows a point $\bar{x}$ with a normal vector $\bar{n}$ and a point $\bar{x}'$ with a normal vector $\bar{n}'$.

$\bar{r}$ is the vector from $\bar{x}$ to $\bar{x}'$, and J' is the radiosity of $\bar{x}'$.

The amount of radiation reaching point $\bar{x}$ from $\bar{x}'$ depends on the amount of J' that is projected on $\bar{x}$ along the vector $\bar{r}$. From this, G_m can be expressed as:

$$G_m = \int_{S'} \frac{\left(-\bar{n}' \cdot \bar{r}\right)\left(\bar{n} \cdot \bar{r}\right)}{\pi \left|\bar{r}\right|^4} J' dS \qquad \text{Equation 10}$$

It then follows that:

$$F_{amb} = 1 - F' = 1 - \int_{S'} \frac{\left(-\bar{n}' \cdot \bar{r}\right)\left(\bar{n} \cdot \bar{r}\right)}{\pi \left|\bar{r}\right|^4} dS \qquad \text{Equation 11}$$

Where F' is the view factor to $\bar{x}'$ from $\bar{x}$.

Equation 10 and Equation 11 are expressed in 3-D form, but can also be expressed in a 2-D form such that:

$$G_m = \int_{S'_\perp} \frac{\left(-\bar{n}' \cdot \bar{r}_\perp\right)\left(\bar{n} \cdot \bar{r}_\perp\right)}{2\left|\bar{r}_\perp\right|^3} J' dS \qquad \text{Equation 12}$$

And

$$F_{amb} = 1 - F' = 1 - \int_{S'_\perp} \frac{\left(-\overline{n'} \cdot \overline{r_\perp}\right)\left(\overline{n} \cdot \overline{r_\perp}\right)}{2\left|\overline{r_\perp}\right|^3} dS \qquad \text{Equation 13}$$

Where $S'_\perp$ denotes the line integral along the geometry's boundaries.

Combining Equation 7 and Equation 9 then gives:

$$J = (1-\varepsilon)\left(G_m + F_{amb}\sigma T^4{}_{amb}\right) + \varepsilon\sigma T^4 \qquad \text{Equation 14}$$

Comsol® applies Equation 14 to all the boundaries involved in surface to surface radiation and the resulting system of linear equations is solved in parallel with the temperature equation. [40]

4.2.1.2 Conduction and Convection

The heat transfer is governed by the first law of thermodynamic; which asserts the conservation of energy. The law is expressed in terms of temperature because it suits this application better.

$$\rho C_P\left(\frac{\partial T}{t} + (\mathbf{u}\cdot\nabla)T\right) = -(\nabla\cdot\mathbf{q}) + \boldsymbol{\tau}:\mathbf{S} - \frac{T}{\rho}\frac{\partial\rho}{\partial T}\bigg|_P\left(\frac{\partial p}{\partial t} + (\mathbf{u}\cdot\nabla)p\right) + \mathbf{Q} \qquad \text{Equation 15}$$

Where:

- *Cp* is specific heat capacity at constant temperature
- ***q*** is the heat flux by conduction vector
- *Q* accounts for heat sources other than viscous heating
- ***S*** is the strain rate tensor such that: $S = \frac{1}{2}\left(\nabla\mathbf{u} + (\nabla\mathbf{u})^T\right)$
- $\boldsymbol{\tau}$ the viscous stress tensor such that: $\tau = 2\mu\mathbf{S} - \frac{2}{3}\mu(\nabla\cdot\mathbf{u})\mathbf{I}$
- **u** is the velocity vector
- *p* is the pressure
- ρ the density
- *T* is absolute temperature

The second term on the right hand side of Equation 15 represents viscous heating; which is of no great significance in this model and can safely be ignored. Thus the equation then becomes:

$$\rho C_P\left(\frac{\partial T}{t} + (\mathbf{u}\cdot\nabla)T\right) = -(\nabla\cdot\mathbf{q}) + \mathbf{Q} \qquad \text{Equation 16}$$

q is the heat flux due to thermal conductivity and is based on Fourier's law of heat conduction such that:

$$q_i = -k\frac{\partial T}{\partial x_i}$$ Equation 17

Where *k,* the thermal conductivity; is the proportionality constant between the temperature gradient and the heat flux.

Combining Equation 16 and Equation 17 then gives:

$$\rho C_P\left(\frac{\partial T}{t} + (\mathbf{u}\cdot\nabla)T\right) = \nabla\cdot(k\nabla T) + \mathbf{Q}$$

$$\Downarrow$$ Equation 18

$$\rho C_P\frac{\partial T}{t} + \rho C_P\mathbf{u}\cdot\nabla T - \nabla\cdot(k\nabla T) = \mathbf{Q}$$

The Comsol® heat transfer interface solves the above equation for the temperature, T. The velocity vector 'u' is obtained from the laminar flow solution and accounts for forced convection due to flow [40].

4.2.2 Laminar flow

The fluid flow is modelled by solving the Navier-Stokes equations in their compressible formulations i.e. varying density. The two equations solved are the continuity equation and the momentum equation.

Continuity Equation:

$$\frac{\partial\rho}{\partial t} + \nabla\cdot(\rho\mathbf{u}) = 0$$ Equation 19

Momentum Equation:

$$\rho\frac{\partial\mathbf{u}}{\partial t} + \rho\mathbf{u}\cdot\nabla\mathbf{u} = -\nabla p + \nabla\cdot\left(\mu\left(\nabla\mathbf{u} + (\nabla\mathbf{u})^T\right) - \frac{2}{3}\mu(\nabla\cdot\mathbf{u})\mathbf{I}\right) + \mathbf{F}$$ Equation 20

It should be noted that by changing Equation 19 to '$\rho\nabla\cdot\mathbf{u} = 0$' the above equations can also be applied to incompressible flow. [28] [40]

Where:

- ρ is the density
- $\mathbf{u}$ is the velocity vector
- p is the pressure
- $\mathbf{F}$ is the force vector
- T is the absolute temperature
- t is time

4.2.3 Mass Transport

The mass transport in the system is mapped by solving a mass balance that accounts for diffusion, convection and generation or consumption.

$$\frac{\partial c}{\partial t} + \mathbf{u} \cdot \nabla c = \nabla \cdot (D \nabla c) + R \qquad \text{Equation 21}$$

Where:
C is the concentration of the species
D is the diffusion coefficient
u is the velocity field vector
R is the reaction rate expression for the species

The first term on the left hand side of Equation 21 represents the accumulation of the species. Since this is a steady state model (for a continuous process), there is no actual change of 'state' with time and the concentration of a given species, at a specific point, does not change with time. Due to this no time dependent solution is required and this term amounts to zero.
The second term on the left hand side expresses the convective mass transport due to the velocity field **u**. The velocity vector is obtained from the momentum transport (laminar flow) solution. It is however important to note that in the boundary layer, close to the tube wall, this velocity vector is zero and mass transport only happens by diffusion.
The first term on the right hand side of the equation represents the mass transport by diffusion. It is solely dependent on the diffusion coefficient D and the concentration gradient. For isotropic diffusion D is a constant but can be entered as a tensor for other forms of diffusion.
The last term in the equation represents generation or consumption of the species and is a reaction rate expression.
In the situation where **u=0** i.e. the boundary layer in the tube, the mass balance equation becomes:

$$\frac{\partial c}{\partial t} = \nabla \cdot (D \nabla c) + R \qquad \text{Equation 22}$$

Generally, Comsol® implements this model by solving Equation 21 while coupling it with the laminar flow Equation 19 and Equation 20. [27, 40] The accuracy of the model will then depend on the precision of the inputs such at the viscosity, thermal conductivity or even the reaction term, R.

4.2.4 Reaction Mechanism and Kinetics

Section 3.6.2 shows the prevalence of the different chlorides of tantalum in the temperature range of 500 – 1100 K. Any of the prevailing tantalum chloride species could be surface active and lead to

a deposition; thus any model across this temperature range must account for the compositional development of the gas mixture and the subsequent surface reactions that lead to the formation of solid tantalum.

Figures 25 & 26 show that $TaCl_5$, $TaCl_4$, $TaCl_3$ and $TaCl_2$ are all thermodynamically stable in the CVD temperature range of 800 – 1100 K and must therefore be accounted for in the model. This leads to a model that involves both homogeneous gas phase reactions and heterogeneous surface reactions.

The homogenous gas phase reactions are implemented such that the reduction reactions are progressive from the higher chlorides to the lower chlorides as shown here:

$$TaCl_{5(g)} + \frac{1}{2}H_{2(g)} \rightarrow TaCl_{4(g)} + HCl_{(g)} \qquad \text{Equation 23}$$

$$TaCl_{4(g)} + \frac{1}{2}H_{2(g)} \rightarrow TaCl_{3(g)} + HCl_{(g)} \qquad \text{Equation 24}$$

$$TaCl_{3(g)} + \frac{1}{2}H_{2(g)} \rightarrow TaCl_{2(g)} + HCl_{(g)} \qquad \text{Equation 25}$$

The heterogeneous surface reactions are implemented such that each of the four chlorides of tantalum has an opportunity to react to form solid tantalum at the surface:

$$TaCl_{5(g)} + \frac{5}{2}H_{2(g)} \rightarrow Ta_{(s)} + 5HCl_{(g)} \qquad \text{Equation 26}$$

$$TaCl_{4(g)} + 2H_{2(g)} \rightarrow Ta_{(s)} + 4HCl_{(g)} \qquad \text{Equation 27}$$

$$TaCl_{3(g)} + \frac{3}{2}H_{2(g)} \rightarrow Ta_{(s)} + 3HCl_{(g)} \qquad \text{Equation 28}$$

$$TaCl_{2(g)} + H_{2(g)} \rightarrow Ta_{(s)} + 2HCl_{(g)}$$ Equation 29

The homogeneous gas phase reactions are implemented as simple first order reactions while the heterogeneous surface reactions are based on Langmuir's adsorption model as described in the next subsection.

4.2.5 Surface Reaction Kinetics

Langmuir's adsorption-desorption model provides a simplified way in which heterogeneous surface reactions can be understood, and it is widely used in the study of surface reactions such as CVD and heterogeneous catalysis. The model assumes that:

- The substrate surface can be viewed as a definite collection of sites upon which the reactants can be adsorbed, ***N***.
- The fraction of the adsorption sites covered by the gaseous species is the Coverage, ***Θ*.**
- All the sites have the same adsorption enthalpy, which is independent of the coverage.
- The adsorption rate (***u*ads**) is proportional to the partial pressure of the adsorbing species and the number of available free sites; while the desorption rate (***u*des**) is only proportional to the number of covered sites.

This can then be represented as:

$$u_{ads} = k_{ads} \cdot (1-\Theta) \cdot NP \quad \text{and} \quad u_{des} = k_{des} \cdot \Theta \cdot N$$ Equation 30

Where ***k*ads** is the adsorption constant, ***k*des** is the desorption constant and ***P*** is the pressure.
At equilibrium (steady state operation in a continuous system) the rate of adsorption and desorption are equal, thus giving:

$$k_{ads} \cdot (1-\Theta) \cdot NP = k_{des} \cdot \Theta \cdot N$$ Equation 31

When the partial pressure is used and a unified constant, $k = \frac{k_{ads}}{k_{des}}$, is added to replace the two constants then the above equation can be rewritten as:

$$\Theta_i = \frac{k_{ads} p_i}{k_{des} + k_{ads} p_i} \Rightarrow \Theta_i = \frac{k p_i}{1 + k p_i}$$ Equation 32

The above equation is vital in determining the subsequent order of the deposition reaction. From the equation is can be derived that:

- When ***kads*** (adsorption constant) is large, the constant ***k*** is also large and hence the coverage tends to approach 1. With a well-covered surface, the rate of the reaction then doesn't depend on the partial pressure of the reacting species.
- When ***kads*** is small, ***k*** is small too and thus the coverage is also low. In this situation, the rate of reaction is very dependent on the partial pressure of the reacting gas.

Adsorption is an exothermic reaction and therefore the adsorption constant diminishes when temperature is increased; therefore increasing temperatures decreases the surface coverage. In such a situation, the partial pressure of the gaseous species contributes a lot to the coverage, upon which the rate of the heterogeneous reaction is dependent. As a result of this dependence on the partial pressure, a heterogeneous reaction – such as high temperature CVD – can be treated as a first-order reaction.

For situations where the coverage is high (close to 1) the reaction can be treated as zeroth-order as it doesn't depend on the reactant partial pressure. [24]

The pressure term in Equation 32 is interchangeable with the concentration of the adsorbate. From the equation it can then be deduced that at high partial pressures or concentrations, the coverage approaches 1 which makes the reaction rate zeroth order with respect to the reactant concentration at the surface. For low partial pressures or concentrations, $\Theta \approx kp_i$, and the reaction is then first order with respect to the surface concentration of the precursor.

In situations where more than one gas adsorbs onto the substrate surface, Equation 32 can then be rewritten as:

$$\Theta_i = \frac{k_i p_i}{1 + \sum_{j=1}^{n} k_j p_j} \qquad \text{Equation 33}$$

Where j is each adsorbing species.

4.3 Estimation of the Gas Properties

Obtaining the correct input data for a model is of vital importance if the model is to perform reliably. In this case one of the most critical aspects of implementing a CVD model is determining the physical properties of the gas mixture being used. Quite often assumptions and simplifications are made because estimating physical properties such as the viscosity, thermal conductivity and diffusion coefficient, of a multicomponent gas mixture, involves very tedious empirical calculations that seldom overcome the inaccuracy caused by simplification. The gas mixture being modeled in this

project is a $TaCl_X$ – H_2 – Ar system that gradually develops HCl. The most abundant gas in the mixture is hydrogen (Mole fraction >90%) while the heaviest is $TaCl_5$ (M=358.5 g/mole) although it only constitutes 2 – 4 mole % of the original mixture. For all property estimation, the contribution of HCl is considered negligible because of its low composition and low molecular weight.

For estimating the temperature dependence of the viscosity, thermal conductivity and specific heat capacity, only a binary mixture of hydrogen and argon are considered. This is a valid simplification in High temperature CVD because the precursor reacts fast at the surface and quickly becomes part of it, implying that it's contribution to the shear stress/ shear strain relation is minimal because it is not 'dragged' along the surface.

A similar simplification is made for determining the diffusion coefficient of $TaCl_X$ ($TaCl_5$ – $TaCl_4$ – $TaCl_3$ – $TaCl_2$). Only a binary mixture of hydrogen and $TaCl_5$ is considered and all the chlorides of tantalum are assumed to have the same diffusion coefficient. This is done for simplicity as calculations for tertiary or higher component mixtures are very complex and seldom avail significant improvements in accuracy.

The density is calculated based on the original (feed) mixture with all components taken into account.

The various properties are calculated in the temperature range of 500 – 1100K and, their values and dependence on temperature are compared to that of hydrogen. Once a consistent correlation is established, the data is entered into the model by applying correction factors (proportionality constants) to the already inbuilt properties of hydrogen; thus mimicking the properties of the mixture. This achieves the desired goal without having to create a new material in the program's (COMSOL®) material library.

4.3.1 Viscosity

The dynamic viscosity of a fluid describes the relationship between the shear rate and shear stress of the fluid. 'Thicker' fluids such as crude oil are described to be more viscous (higher viscosity) than 'thinner' fluids such as water or gases. The SI unit for viscosity is Pa·s.

The viscosity of the gas mixture is determined by using the method of Reichenberg which has been shown to only produce deviations of around 0.8%. [41] [42] The general equation for the viscosity of multi-component mixtures is:

$$\eta_m = \sum_{i=1}^{n} K_i \left(1 + 2\sum_{j=1}^{i-1} H_{ij} K_j + \sum_{j=1 \neq i}^{n} \sum_{K=1 \neq i}^{n} H_{ij} H_{ik} K_j K_k \right) \quad \text{Equation 34}$$

$$K_i = \frac{y_i n_i}{y_i + \eta_i \sum_{k=1 \neq i}^{n} y_k H_{ik} \left[3 + \left(2M_k / M_i \right) \right]} \quad \text{Equation 35}$$

Where:

η_m is the mixture viscosity, n is the number of components, η_i is the viscosity of the pure i, M_i is the molecular weight of i, and y_i is the mole fraction of i in the mixture.

H_{ij} from Eq. 34 is an arbitrary term expressed as:

$$H_{ij} = \left[\frac{M_i M_j}{32\left(M_i + M_j \right)^3} \right]^{\frac{1}{2}} \left(C_i + C_j \right)^2 \times \frac{\left[1 + 0.36 T_{rij} \left(T_{rij} - 1 \right) \right]^{1/6} F_{Rij}}{\left(T_{rij} \right)^{1/2}} \quad \text{Equation 36}$$

And $T_{rij} = \frac{T}{\left(T_{ci} T_{cj} \right)^{1/2}}$ Equation 37

Two more component properties are introduced such that:

$$U_i = \frac{\left[1 + 0.36 T_{ri} \left(T_{ri} - 1 \right) \right]^{1/6} F_{Ri}}{\left(T_{ri} \right)^{1/2}} \quad \text{Equation 38}$$

$$C_i = \frac{M_i^{1/4}}{\left(\eta_i U_i \right)^{1/2}} \quad \text{Equation 39}$$

Where:

$$T_{ri} = \frac{T}{T_{ci}} \quad \text{Equation 40}$$

T is the temperature in question and T_{ci} is the critical temperature of i.

F_{Ri} is the polar correction factor such that:

$$F_{Ri} = \frac{T_{ri}^{3.5} + \left(10 \mu_{ri} \right)^7}{T_{ri}^{3.5} \left[1 + \left(10 \mu_{ri} \right)^7 \right]} \quad \text{Equation 41}$$

μ_{ri} is the reduced dipole moment of i and is expressed as:

$$\mu_{ri} = 52.46 \frac{\mu^2 P_c}{T_c^2}$$ Equation 42

Where μ is the dipole moment in debyes, P_c is the critical pressure in bars and T_c is the critical temperature in Kelvin.

Equations 35 – 42 provide the required fields of solving Equation 34 and once substituted the viscosity of the mixture is obtained in micro Poise [μP].

The simplified versions of Eq. 34 and Eq. 35 for binary mixtures respectively are:

$$\eta_m = K_i \left(1 + H_{ij}^2 K_j^2\right) + K_j \left(1 + 2H_{ij} K_i + H_{ij}^2 K_i^2\right)$$ Equation 43

$$K_i = \frac{y_i n_i}{y_i + \eta_i \{y_j H_{ij} [3 + (2M_k / M_i)]\}}$$ Equation 44

Based on these calculations, the viscosity of the mixtures was determined and a linear correlation was established with the same volume of Hydrogen gas. The correction factor is then the value that is multiplied by the viscosity of pure Hydrogen to get that of the mixture.

4.3.2 Thermal conductivity

Thermal conductivity is a measure of a materials ability to conduct heat. It is generally obtained by applying Fourier's law of heat conduction and can be described as the constant of proportionality between the temperature gradient and the heat flux. It has the SI unit W/(m·K).
The thermal conductivity of the binary mixture is found by using the Mason and Saxena method which has been Shown to have an error in the region of 3.6 – 4.2%. [41, 43]
The method relies on the Wassiljewa equation: [41]

$$\lambda_m = \sum_{i=1}^{n} \frac{y_i \lambda_i}{\sum_{j=1}^{n} y_j A_{ij}}$$ Equation 45

Where:

λ_m and λ_i are the thermal conductivities of the mixture and component *i* respectively.

y_i and y_j are the mole fractions of components *i* and *j* respectively.

And A_{ij} is a function such that:

$$A_{ij} = \frac{\left[1 + (\lambda_{tri} / \lambda_{trj})^{1/2} (M_i / M_j)^{1/4}\right]^2}{\left[8(1 + M_i / M_j)\right]^{1/2}}$$ Equation 46

Where:

M is the molecular weight in *g/mol*

λ_{tr} is the monatomic value of the thermal conductivity; which is unnecessary to calculate because:

$$\frac{\lambda_{tri}}{\lambda_{trj}} = \frac{\eta_i}{\eta_j}\frac{M_j}{M_i}$$ Equation 47

Where η is the dynamic viscosity.

It is important to mention that the thermal conductivity and dynamic viscosity of a dilute gaseous mixture have the same temperature dependence and are independent of the pressure given that it is low enough for the mixture to be dilute.

Substituting Equation 46 and Equation 47 into Equation 45 provides a reliable method for determining the thermal conductivity of the dilute gas mixture. By comparing the calculated values of the mixture to those of pure hydrogen gas, at the corresponding temperature; a correction factor is obtained that can be multiplied by the thermal conductivity of hydrogen to get that of the mixture within the desired temperature range.

4.3.3 Density

The density of the mixtures is determined by using the normal density equation:

$$\rho = \frac{m}{V}$$ Equation 48

Where ρ is the density, V is the volume and m is the mass; n is the number of moles and M is the Molar weight.

$$\rho_{mix} = \frac{m_1 + m_2 + m_3 + \ldots}{V_{total}} \quad and \quad m = n \cdot M$$

$$\Downarrow$$

$$\rho_{mix} = \frac{n_1 M_1 + n_2 M_2 + n_3 M_3}{V_{total}}$$ Equation 49

4.3.4 Specific Heat Capacity

The specific heat capacity of a material is the amount of heat energy required to raise the temperature of a unit mass of the material by one Kelvin. It is sometimes referred to as the heat capacity at constant pressure for compressible fluids. The specific heat capacity of an ideal binary mixture of gases is determined by calculating the contribution of each part of the mixture based on its mole fraction. This mixture of hydrogen and argon can be assumed to be entirely ideal because of the high

temperature and low pressure at which the gases are. Furthermore, there is no chemical interaction between the gases; and the concentration of argon in the mixture is very low (i.e. less or equal to 3.2%) because it is only used to reduce the partial pressure of the precursor while still in the precursor generator, prior to mixing with excess hydrogen.

$$Cp_{Mix} = x_i \cdot Cp_i + x_j \cdot Cp_j \qquad \text{Equation 50}$$

Where:

Cp_{Mix} is the specific heat capacity of the mixture

Cp_i and **Cp_j** are the specific heat capacities of the pure components

x_i and x_j are the mole fractions of component ***i*** and ***j*** respectively.

Based on Equation 50, values for the mixture are calculated within the relevant temperature range of 500 – 1100 K and a correlation between these values and those of pure hydrogen, at the same temperature and pressure, is made. Based on this correlation a correction factor is determined; by which the specific heat capacity of hydrogen is multiplied to get that of the mixture under the same conditions.

The ratio of specific heats is the quotient of the specific heat at constant pressure to the specific heat at constant volume. The standard value for ideal gases is 1.4. [44] It is also a general rule that:

$$C_v = C_p - R \qquad \text{Equation 51}$$

Where C_V is the heat capacity at constant volume and *R* is the gas constant.

4.3.5 Diffusion Coefficient

Diffusion is the mass transfer of a species from a region of higher concentration to one of lower concentration. It is mathematically governed by Fick's law where the diffusion coefficient is the constant of proportionality between the concentration gradient and the net flux [28].

$$J = D \cdot \frac{\partial C}{\partial x} \qquad \text{Equation 52}$$

Where:

J *is the net flux* in $\mathrm{mol}/\mathrm{m}^2 \cdot s$

D *is the Diffusion Coefficient in* m^2/s and

$\frac{\partial \mathbf{C}}{\partial \mathbf{x}}$ *is the* **C***oncentration gradiet along the direction of diffusion,* **x**

Getting a reliable estimate for the diffusion coefficient of Tantalum (V) Chloride in the Hydrogen – Argon carrier gas system is vital for the implementation of the CVD model since diffusion is the means of transport by which the reactant species in the bulk flow reach the surface.

The standard '*Chapman and Enskog'* equation has been shown to be a reliable and relatively less tedious method of estimating diffusion coefficients of dilute binary gas mixtures at low pressures. [42, 45-47]

$$D_{AB} = 1.858 \cdot 10^{-3} \frac{\sqrt{T^3 \left(1/MW_A + 1/MW_B\right)}}{p\sigma_{AB}{}^2 \Omega_{AB}} \quad in\ cm^2/s \qquad \text{Equation 53}$$

Where:

T is the temperature in Kelvin; ***p*** the pressure in atmosphere (atm), ***MW*** the molecular in *g/mol*. σ_{AB} is the collision diameter between species A and B in *Å*. Ω_{AB} is the collision integral and is dimensionless.

The collision diameter, σ_{AB}, is the normal average of the collision diameters of species A and B such that:

$$\sigma_{AB} = \frac{1}{2}\left(\sigma_A + \sigma_B\right) \qquad \text{Equation 54}$$

[48]

The collision integrals, Ω_{AB}, are taken from tables that relate them to the reduced temperature ***T****. [29] The reduced temperature is calculated using the energy of interaction, $\boldsymbol{\varepsilon}$, based on the Lennard-Jones, 'L-J', parameters as estimated by *S. Eriksen*. [29]

$$\frac{\varepsilon}{k} = 0.77 \cdot T_C \qquad \text{Equation 55}$$

Where ***k*** is the Boltzmann constant and $\boldsymbol{T_C}$ is the critical temperature.

The energy of interaction between species A and B is then described as: [29, 48]

$$\varepsilon_{AB} = \sqrt{\varepsilon_A \varepsilon_B} \qquad \text{Equation 56}$$

And

$$T^* = \frac{kT}{\varepsilon_{AB}} \qquad \text{Equation 57}$$

For this project, none of the L-J parameters (ε and σ) were calculated but were rather taken from literature. [29]

5 EXPERIMENTAL

5.1 The CVD Pilot Plant

Figure 29, below, is a simplified flow chart depicting the design of the pilot plant used for the experiments in this project. It consists of two main sections i.e. the gas supply section, labeled '*A*', and the main process area. The flow chart only shows features that are directly relevant to the CVD process and leaves out some manual valves, the radiation shields and the by-pass line used to independently evacuate the gas supply section. The machine is designed and built by *Eriksen* [29].

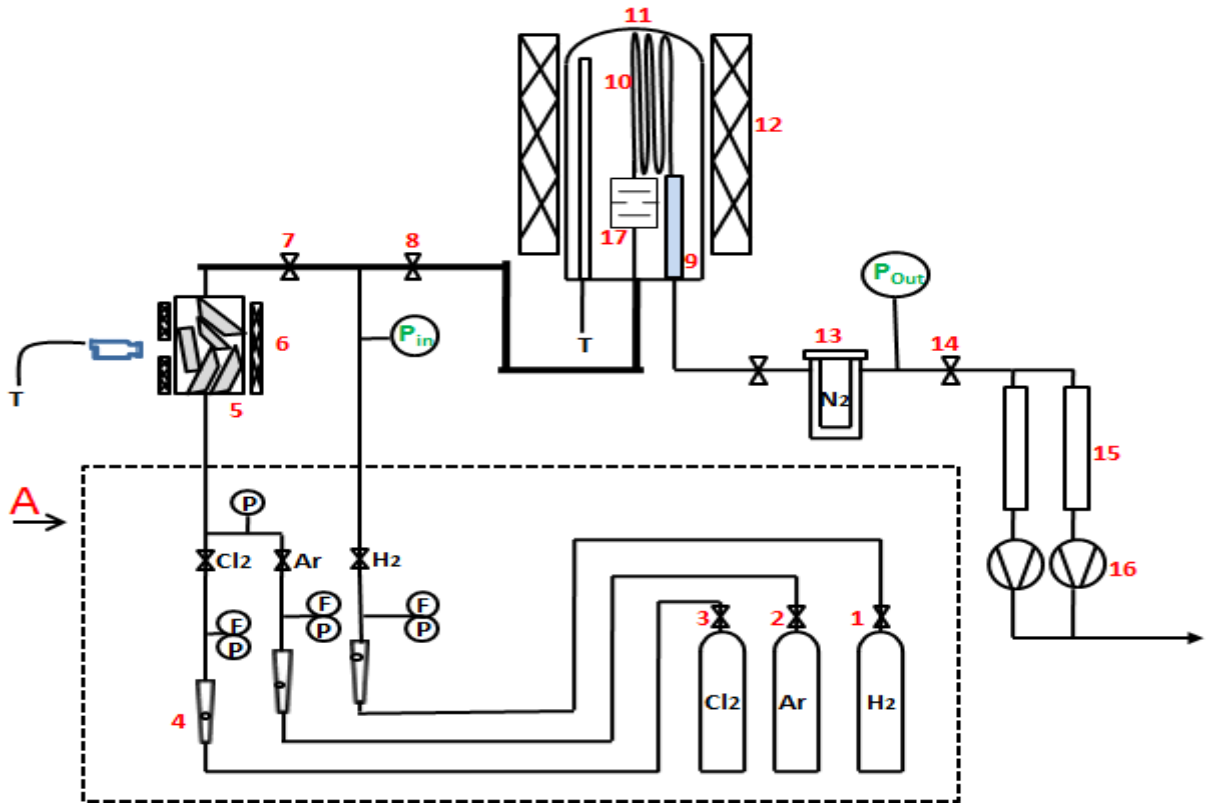

Figure 29: Flow Chart for the CVD pilot plant.

Key:

1, 2, 3 – Gas Feed control valves
4 – Rotameters
5 – Chlorination reactor ($TaCl_5$ generator)
6 – Heating element for the generator
7, 8, 14 – Control valves
9 – Exhaust Pipe
10 – Coiled Tube (substrate)
11 – CVD Reactor
12 - Furnace
13 – Cold Trap (with liquid N_2)
15 – Filters
16 - Vacuum pumps
17 - Pre-heater
P & F – Pressure and Flow controllers
P_{in} and P_{out} – Inlet and Outlet Pressure sensors
T – Temperature Sensor

5.1.1 The Gas supply

The gas supply area is marked 'A' in Figure 29 and mainly consists of flow meters, pressure gauges and three pressurized gas cylinders i.e. Argon (*AGA, 99.99%*), Chlorine (*Air Liquide or Praxair, 99.99%*) and Hydrogen (*AGA, 99.9%*). Since the pilot plant is fully automated the flow rates of the gases are automatically controlled by PID controllers. It is however important to note that although the Argon and Hydrogen feed lines employ regular thermal mass flow controllers, the Chlorine line is fitted with a Coriolis type mass flow meter due to the reactive nature of the gas.
A safety feature is also implemented such that the hydrogen and chlorine feeds are cut off if the tantalum chloride generator pressure exceeds a predetermined safety limit.

5.1.2 The Chlorination Reactor

The chlorination reactor is a quartz glass chamber preloaded with tantalum metal and fitted with a heating jacket. The temperature is measured by an infrared thermometer fitted with a laser to assist with aiming. Chlorine and argon are fed through the bottom of the chlorinator while $TaCl_5$ and the argon leave through the top. The top of the chlorinator is insulated to prevent condensation of the chloride onto the reactor walls. The piping from the chlorinator to the main reaction chamber is also heavily insulated and heat traced at 200^{O}C to keep the precursor in gaseous state. Hydrogen is added after the chlorinator, in a T-piece after valve (labelled 7), to act as a carrier gas and later on a reducing agent.

5.1.3 Main Reaction Chamber

The main reaction chamber is cylindrical steel vessel closed on one end and open at the other end. It has a 200 mm inside diameter and height of 1400 mm. It stands with the open end at the bottom which is sealed off by a stationary water cooled stainless steel flange with a rubber gasket (O-ring). The flange has openings for the inlet stream, exhaust and a thermowell. There is also one more opening for the preheater thermal couples. All the openings are tightly sealed with rubber gaskets or PTFE tape to prevent leakage from the surrounding into the system. Three temperature control thermocouples (for the top, middle and bottom sections of the chamber) are fitted into the thermowell; and one adjustable thermal couple is also fitted to be used for measuring the temperature gradient in the chamber. Although not shown in Figure 29, there is a stand with four horizontally orientated 1 mm thick steel plates arranged in vertical order to protect the bottom flange from the heat radiation of the chamber.
When the preheater is in use, a 430 mm long stainless steel tube of 10 mm inside diameter leads the reactants from the inlet opening to the entrance of the preheater. The preheater is an 100 mm by 100 mm stainless steel cylindrical enclosure with 3 graphite baffles inside to distribute the flow of the gases along its walls. This ensures that the reactants are heated up to the required temperature before contact with the substrate is established.

The stainless steel tube to be coated is connected to the top sealing flange of the pre-heater where a restriction throttle (2 – 3.5 mm diameter) is fitted. This helps to ensure the right pressure in both the pre-heater and inside the tube. The exit of the tube is connected to the exhaust (suction end).
In the experiments where the preheater has been eliminated, the tube to be coated is connected directly to the inlet orifice of the bottom flange.

5.1.4 The Furnace

The electric furnace is placed and supported over the CVD reactor. It has three heating regions i.e. the top, middle and bottom, to ensure a uniform temperature along the height of the chamber. Each of the heating regions is fitted with a thermocouple and is independently controlled by a PID controller for overheating protection.

5.1.5 The Cold trap and the filters

The cold trap consists of an inner section in which the liquid nitrogen is held and an outer 'jacket' section through which the exhaust gases flow. The purpose of the cold trap is to freeze and hold the HCl by product and the unreacted $TaCl_5$ before they can reach the pumps. An activated filter is also installed before each of the two pumps to retain the coarse particles in the exhaust and to bind any HCl that passes the cold trap.
The liquid nitrogen in the cold trap is supplied from an 150 liter pressurized container with an automatically controlled feed valve.
Also available is a travelling winch, supported on the ceiling by moving rails, which allow the winch to be moved around freely while positioning or removing the main reaction chamber and the furnace.

5.2 Experimental procedure

5.2.1 Calibration and installation

The CVD machine consists of 3 flow meters, several pressure sensors and ball valves, among other things. For it to work well, the flow meters and the pressure sensors have to regularly be calibrated to ensure that they are showing the correct values. In this project, it is the practice that such calibrations are done every time there is a major change in the process parameters, or every fourth run.
The valves also have to occasionally be rid of solidified $TaCl_5$ to avoid the build-up of friction between the valve body and the ball's seat, which makes regulation difficult.
In some experiments a preheater is used to heat the gas before it is admitted to the substrate; the preheater installation is shown in Figure 30.

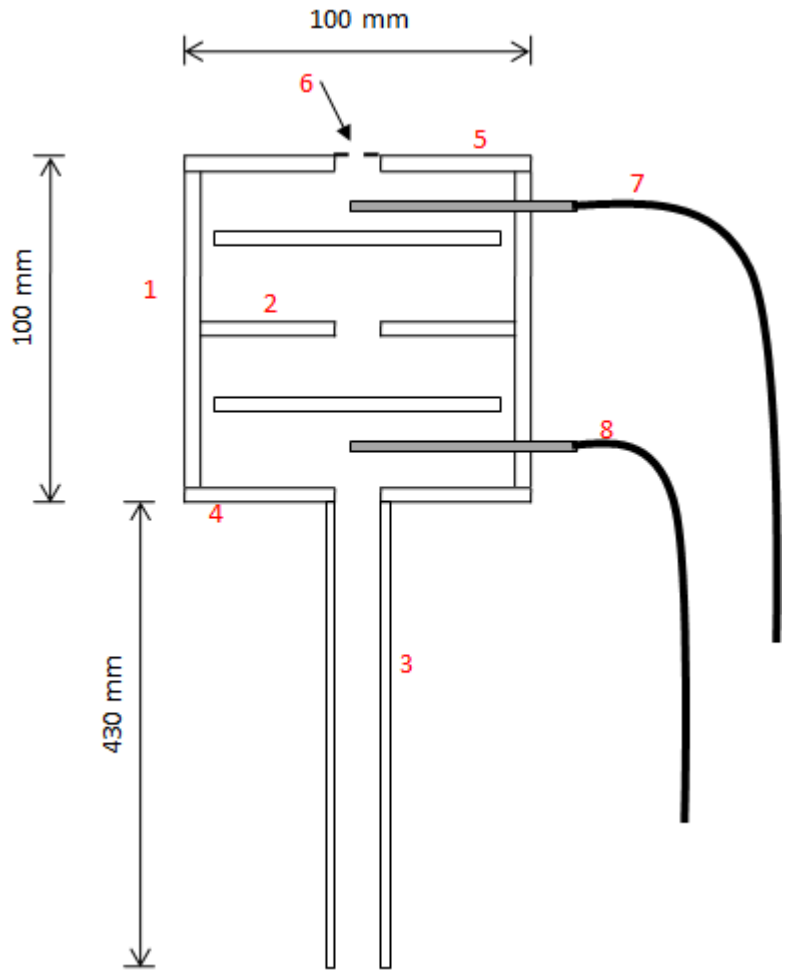

Figure 30: Preheater Installation.

Where:

1) Cylindrical preheater wall
2) Graphite baffles
3) Stainless steel Inlet tubing
4) Preheater's bottom flange
5) Preheater's top flange
6) Restriction
7) Outlet Thermal couple
8) Inlet Thermal couple

5.2.2 Substrate Preparation

5.2.2.1 Tube Bending

Stainless steel (AISI 316) Swagelok® tubes of 10mm internal diameter, 12mm outside diameter and 4.5m - 6m length are used to investigate tantalum CVD in long narrow channels. The length to diameter ratio in this case is 450 - 600.

The first step of preparation is to bend the steel tubes into coils so that they can fit into the reaction chamber. This is done using a standard manual tube bender, while care must be taken to make sure that the tube is bent in a self-draining fashion. The drainability of the tube is important for the subsequent cleaning steps, which involve the use of aggressive aqueous media. A continual slope also aids in getting rid trapped of air bubbles during the cleaning steps.

5.2.2.2 Cleaning

The cleaning step is very important in all CVD processes in order to remove unwanted materials from the surface that could compromise the coating's integrity. This helps to prevent contamination of the deposited layer by impurities and to also ensure that the layer adheres to the substrate. The presence of substances such as oil/ grease, dirt and oxide layers can be detrimental to both the physical and chemical properties of the coating. With that taken into account, it is therefore important to thoroughly clean every sample as the success of the process could very well be hinged on this.

The cleaning process consists of two main steps between which the substrate is rinsed with demineralised water. The cleaning steps are follows:

1) Degreasing with a hot alkaline solution at 80^{0}C for 10 minutes
2) Rinsing thoroughly with distilled at room temperature
3) Pickling with an acid solution at room temperature for 5 minutes
4) Rinsing again with demineralised water at room temperature until one is satisfied that all the acid has been removed.

When cleaning the tubes, the cleaning fluids are first allowed to flow through the tube to flush out any undesirable substances and then the treatment time (10 minutes and 5 minutes, respectively) can commence.

The alkaline degreasing solution consists of:

- 1000 mL demineralised water
- 100 g Gardoclean® 387 (Chemetall)

The dry acid pickling solution consists of:

- 80 g mixture of $NaHF_2$ and $NaHSO_4$ (Engtech Scandinavia)
- 1000 mL destilled water

After the final rinse, the substrates are dried by using compressed air and are then left to stand overnight in a clean and dry environment so that any remaining water can evaporate.

5.2.2.3 Reactor Loading

After drying, the tube is installed into the CVD chamber as shown in Figure 29 (in some experiments the preheater is removed).

The main reaction chamber (*marked '11' in* Figure 29) is then lowered into position by using the winch. This is then followed by lowering the furnace into its position above/ around the chamber, putting the liquid nitrogen tank in place and connecting the relevant control, feedback and power supply lines.

The system is then evacuated until approximately 50 microbar in the main chamber and left to stand for a few hours so that a leak test can be performed. It is common practice that the system is left to stand overnight so that the leak test is performed the morning of the experimental run. A leak rate below $2.5x10^{-3}$ mbar•L/s is acceptable.

5.2.2.4 Startup

Once the leak test is approved, the process can be started. Since the pilot plant is fully automated, all the process parameters are entered into a user interface as part of a recipe on which the machine runs. The operator's job is mainly to monitor and follow the instructions of the operating program.

In the first step of the run, the entire system is evacuated while the cold trap is filled with liquid nitrogen and the furnace starts heating up towards the desired temperature. The heat tracing on the tubing between the chlorinator and the reaction chamber is set at 200°C while the chlorinator is heated up to 400°C. The heating time can range between 1 – 1.5 hours depending of the desired temperature in the chamber.

When the chamber reaches the desired temperature, valve 7 (Figure 29) is closed and hydrogen is allowed to flow through the deposition reactor at a pressure of 20 mbar for 20 minutes. This helps to get rid of any oxides left on the substrates or to reduce other unwanted materials that might have been persistent through the cleaning process.

When the 20 minutes are over, the hydrogen flow is stopped and chlorine is allowed to flow into the chlorinator. The start of the chlorination reaction is marked by a steep increase in the chlorinator's temperature accompanied by a sharp fall in pressure. The increase in temperature is due to the exothermic nature of the chlorination reaction while the decrease in pressure is due to the stoichiometry of the reaction i.e. 2.5 moles of chlorine gas form 1 mole of $TaCl_5$.

$$Ta_{(s)} + 2.5Cl_{2\,(g)} \rightarrow TaCl_5 \qquad \textbf{Equation 58}$$

5.2.2.5 Deposition of Tantalum

When the chlorination reaction starts, argon and hydrogen are allowed to flow as shown in Figure 29. Due to the exothermic nature of the chlorination process, the chlorinator's electric heating can be turned off once the process begins and the temperature thereof tends to settle between 550 – 600 ^{O}C.

Process parameters such as gas flows, pressures and temperature are left constant throughout the deposition process. The level of liquid nitrogen in the cold trap is continuously monitored and controlled by a level switch, which sets off an alarm and re-fills the container if the level falls below the required height.

5.2.2.6 Cooling down

After the deposition process has run for the desired amount of time, the chlorine feed is cut off. The chlorinator is purged with argon for 3 minutes and then valve 7 is closed prior to stopping the argon flow. This helps to prevent contact between the hot tantalum metal in chlorinator with hydrogen. At this stage, the heat tracing along the main reactor's feed line is turned off and the hydrogen supply is ceased 3 minutes after that by closing valve 8.

At this point, the reactor has to be cooled down intelligently in order to avoid the destruction of the deposited tantalum due to the release of dissolved hydrogen within the layer's matrix. To achieve this, the pressure control valve '14' is set to fully open and the system is evacuated to the lowest possible pressure, ca. 80 μbar, and then left for 10 minutes. This facilitates the removal of any hydrogen that is dissolved in the newly deposited tantalum layer, hence there is no hydrogen to come out of solution during the cooling process and crack the tantalum. [21, 22, 32]

The furnace is then taken off to allow faster cooling of the chamber. The cold trap is also removed and placed under a fume hood where it is flooded with tap water while both the liquid nitrogen and frozen HCl are allowed to escape before it is cleaned, dried and reconnected to the machine.

When the chamber has cooled below 200^{O}C, it can removed and the substrate taken out for analysis. The bottom flange of the vacuum chamber is also cleaned and the chamber is put back into place. The final step is to evacuate the entire system and turn off the machine.

5.2.3 Characterization of Tantalum Deposits

5.2.3.1 Thickness by Optical Microscopy

The tantalum layer thickness, at points of interest, is determined by cutting out samples and analysing them under a light microscope.

For this, 20 mm long sections are cut out and mounted into acrylic resin for edge retention while grinding. The samples are first grinded using coarse grit paper to remove edge effects from the cutting tools and then finer grinding matrices are used to achieve as smooth a surface as possible.

The samples are then etched to create a clear distinction between the tantalum and the steel. The prepared samples are then analysed under a calibrated light microscope to determine the thickness of the tantalum layer.

Sample Preparation Steps for Optical microscopy:

- Clean the samples with absolute ethanol to remove grease from the cutting tools
- Mount the samples in Acrylic hot mounting resin (SpeciFast – By Struers), Heating time of 5 minutes and cooling time of 6 minutes under 25 kN pressure.
- Grind the samples progressively, first to eliminate the edge effects of the cutting tools and then to polish the surface using: Silicon carbide abrasive water cooled grit paper (Struers); FEPA P# 30, 220, 500, 1200 and 2400
- The samples are then etched in an acidic solution and then viewed in a microscope. The etching is done by exposing the sample to a mixture of: 50 ml concentrated Hydrochloric acid, 5 ml concentrated Nitric acid, 50 ml demineralised water and 4 drops of Dr. Vogel's sparbejdse. Exposure time is 4 seconds.

5.2.3.2 Analysis by Scanning Electron Microscopy

Some tube samples are also analysed by means of a scanning electron microscope (SEM) to determine the nature of the layer and it's interaction with the substrate.

The sample preparation methods for SEM imaging are as follows:

Sample Preparation Steps for SEM imaging (Tube samples):

- Clean the sample with absolute ethanol to remove grease from the cutting tools
- Mount the sample in Phenolic hot mounting resin with carbon filler (PolyFast – By Struers), Heating time of 5 minutes and cooling time of 6 minutes under 25 kN pressure.
- Grind the sample progressively, first to eliminate the edge effects of the cutting tools and then to polish the surface using: Silicon carbide abrasive water cooled grit paper (Struers); FEPA P# 30, 220, 500, 1200 and 2400

5.3 Plate Heat Exchanger Trials

Figure 31: Alfa Laval® CB30 Heat Exchanger. Dimensions are in mm (inches)

The plate heat exchangers are treated like any other substrate however; they do not need to be cleaned because the manufacturing process renders them clean enough for CVD. The CB30 heat exchanger to be coated consists of 20 copper brazed stainless steel plates (AISI 316), and therefore 9 flow channels to be coated. The heat exchanger actually has a total of 19 channels however only one side of it is coated since only the side in contact with aggressive chemicals needs to be protected from corrosion. The utility side (10 channels) is left untreated and hence only the 9 process channels are treated. The coating process is achieved with help from Tantaline® A/S while the analysis of samples after coating is achieved with the help of Alfa Laval®, Lund – Sweden.

6 Results and Discussion

6.1 Deposition Rate Profiles with a Preheater in use

The preheater described in section 5.2.1 was installed to make sure that the gases (precursor and carrier gas) reach the substrate at the desired temperature. This was done at the opportunity cost of losing some of the precursor to deposition in the preheater. The experiments with the preheater were done as a continuation to a prior project, by the author, to further study the variations in the tantalum deposition profile due to temperature. The results from the prior project are shown in appendix A and were done at temperatures of 775 and 825 ^{O}C at 25-mbar pressure. The preheater experiments in this project were done at 900 and 950 ^{O}C, at 25-mbar pressure, and at the same reactant compositions as the former experiments so that they can be comparable. These are shown in figure 32.

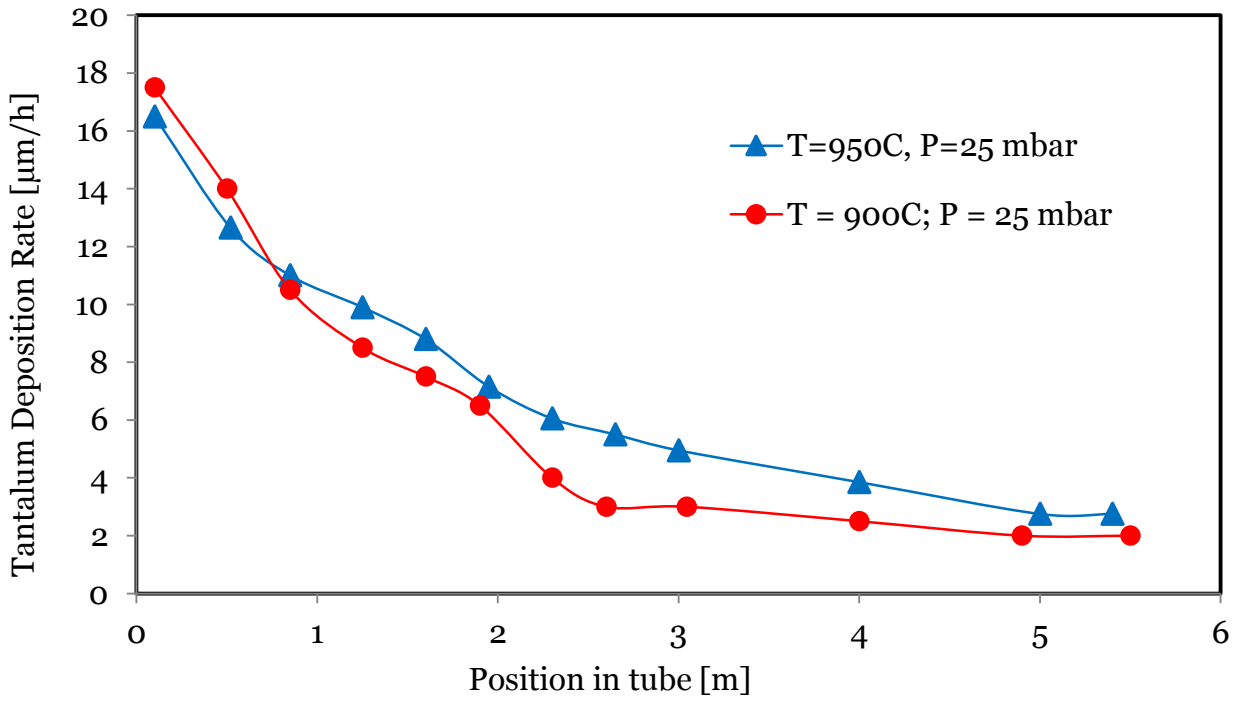

Figure 32: Tantalum deposition rates along the tube length at 900 and 950^{O}C; with a preheater installed.

Based on these profiles and those shown in appendix A, it was concluded that the experiments involving a preheater were too similar for any kinetic study to be done. It was deemed that the part of the reaction that is very temperature dependent was actually happening within the preheater, which was not considered for analysis due to the impracticality of it. Analysing the deposition rates within the preheater would require cutting it open and therefore building an entirely new one for every experiment.

The preheater was then eliminated from all subsequent experiments and the reactants were allowed to enter the tubes at 200 ^{O}C and heat up therein towards the desired reaction temperature.

6.2 Deposition Rate Profiles without a Preheater

Prior work by *Eriksen* [29] and work experience from the project partner Tantaline A/S have shown that at 825 ^{O}C and 25 mbar, the reaction conditions are optimal for most tantalum CVD applications. That is why this region was chosen as a starting point for studying the CVD of tantalum in long narrow channels.

It is important to note that all volumetric flow rates mentioned in this project are given at standard temperature (273.15 K) and pressure (0.987 atm). The values shown as process pressure are not related to the feed volumetric flows but rather the pressure measured right at the exit of the tubular reactor. Looking at figure 29, the flow rates of the reactants and carrier gas are measured in the gas supply area marked 'A' while the system pressure is measured between the cold trap and the valve marked '14'.

As a starting point, experiments were done to investigate the effect of substrate temperature on the deposition rate at constant pressure and reactant feed rates. These were done at a pressure of 25 mbar, and the reactant feed rates were 150 L/h of Hydrogen, 5 L/h of Argon and 50 grams/ h of Chlorine; while the temperature was varied from 700 – 950 ^{O}C.

An experiment done at 700 ^{O}C did not result in any measurable amount of tantalum deposited in the tube. The reaction yield/ conversion was estimated at 4 % based on weight gain, and the reactor's feed line was blocked due to condensation of the precursor before reaching the tube. This happened because at 700 ^{O}C the bottom of the reactor gets too cold to sustain the precursor in the gas phase hence the condensation. A new reactor design would be required to run experiments at this temperature.

All the other experiments were done successfully and some were repeated several times to ensure the reproducibility of the data.

Figures 33 – 37 show the deposition profiles of each temperature while figure 38 shows a comparison of the mean profiles on the same axes.

A second set of experiments was done to determine the effects of system pressure on the deposition profile. In these, the feed rates and temperature were kept constant while the pressure was varied. The chosen pressures were 100 mbar, 300 mbar and 990 mbar (ca. 1 atm) while the temperature was set at 800 ^{O}C. The reactant feed rates were 300 L/h of Hydrogen, 80 L/h of Argon and 50 grams/ h of Chlorine. The hydrogen flow rate was increased from the 150 L/h used in the previous runs to 300 L/h in order to lower the partial pressure of the precursor without compromising the precursor feed rate; and likewise the argon flow was increased from 5 – 80 L/h. This is important because it

helps prevent condensation of the precursor at the reactor inlet and reduces the chances of having gas phase deposition. The data for the pressure tests is shown in Figure 39.

A third set of experiments was carried out to investigate the effect of reactant partial pressure and precursor residence time. To achieve this, two experiments were run at a temperature of 800 ^{O}C but with different feed rates and system pressure. The experiment earlier done at 800 ^{O}C and 25 mbar (150 L/h of Hydrogen, 5 L/h of Argon and 50 grams/ h) was taken as a point of reference from which variations were made. The first variation was to triple the hydrogen feed rate from 150 L/h to 450 L/h while also tripling the system pressure from 25 mbar to 75 mbar (76 mbar). This results in a system in which the feed partial pressures and instantaneous residence times of all the gas components is the same as in the reference run at 25 mbar but at a higher deposition pressure.

The second variation was to triple the hydrogen feed rate from 150 L/h to 450 L/h while leaving the system pressure constant at 25 mbar. This would reduce the precursor partial pressure by a factor of three without affecting the instantaneous residence time. During this run, the lowest pressure that could be achieved was 34 mbar because the pumps could not reach 25 mbar at such high flow rates. The results of this are shown in Figure 40.

6.2.1 Effects of Temperature at Constant Pressure and Feed rate

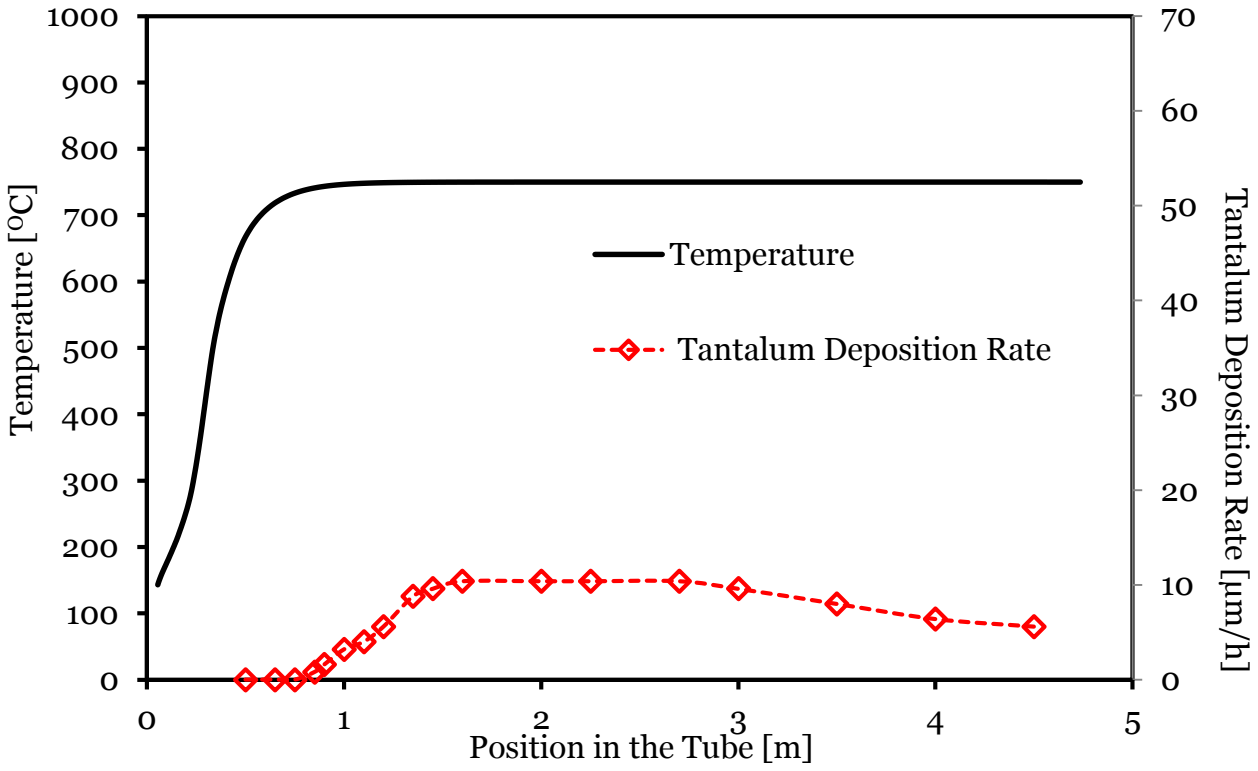

Figure 33: Tantalum deposition rate profile at 750 ^{O}C and 25-mbar

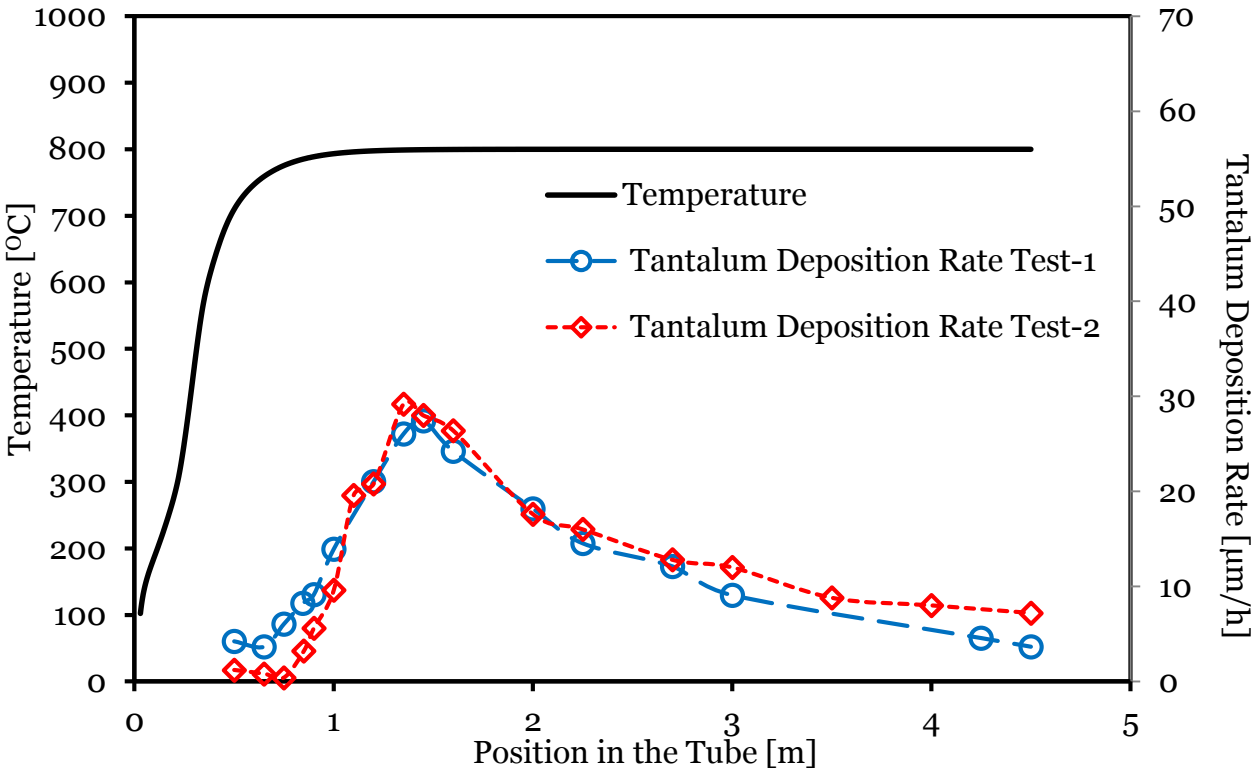

Figure 34: Tantalum deposition rate profile at 800 °C and 25-mbar

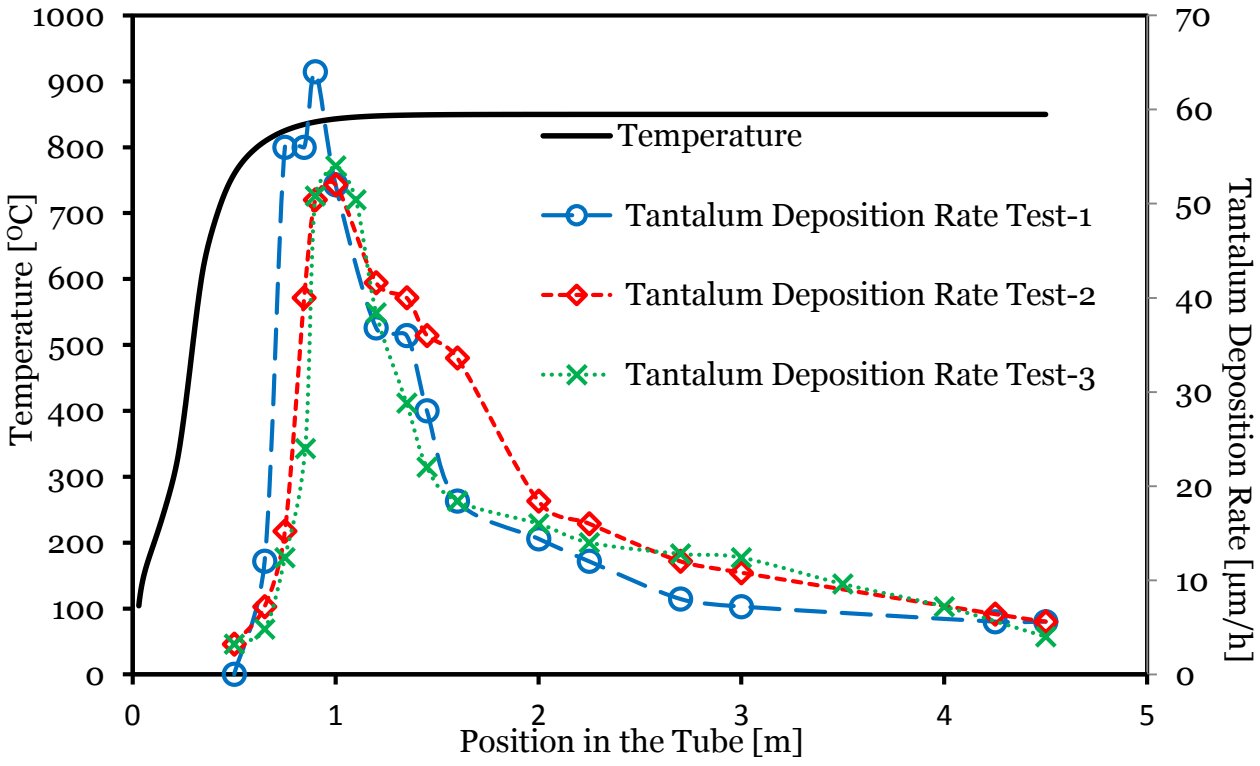

Figure 35: Tantalum deposition rate profile at 850 °C and 25-mbar

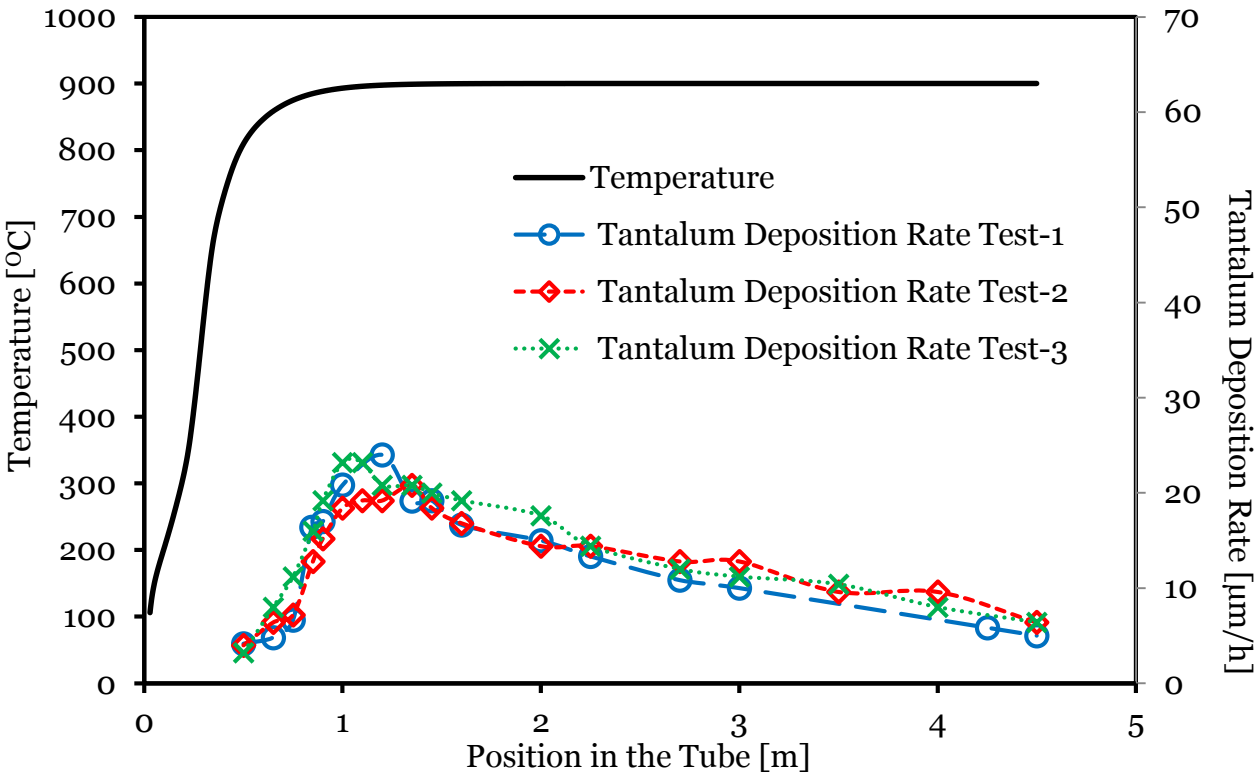

Figure 36: Tantalum deposition rate profile at 900 °C and 25-mbar

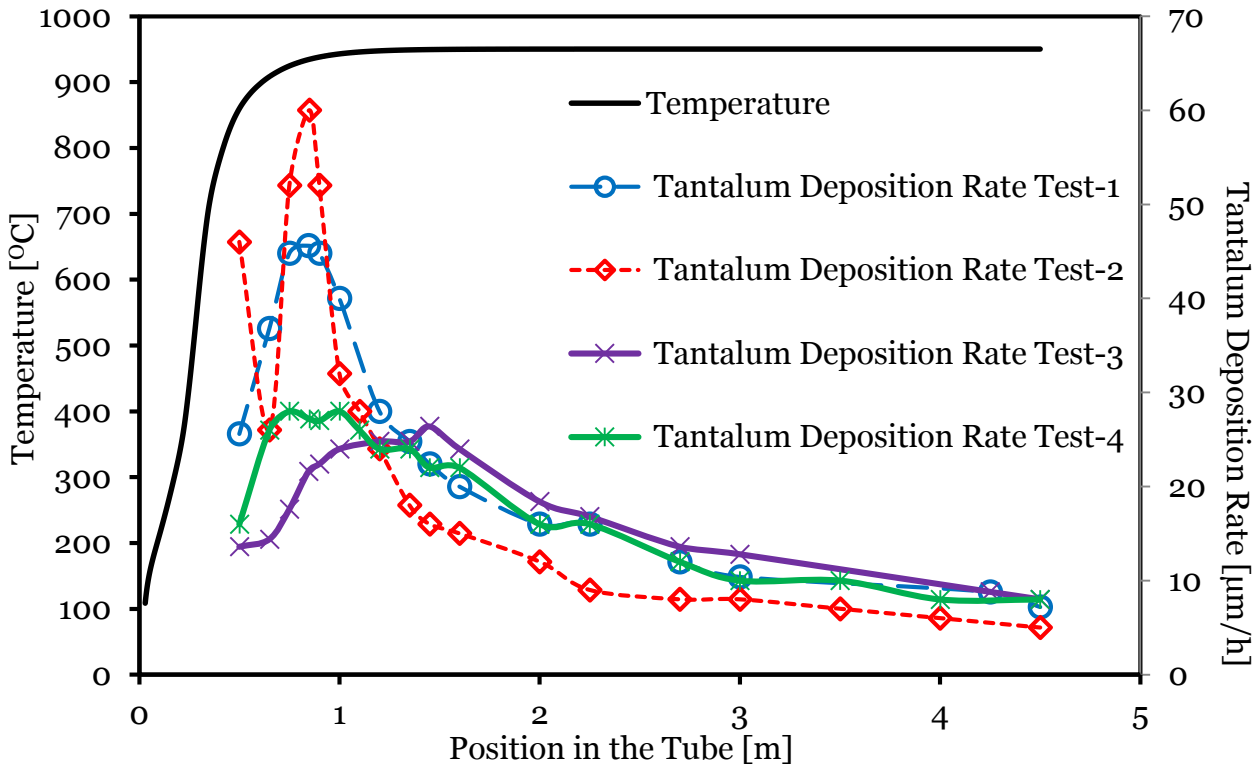

Figure 37: Tantalum deposition rate profile at 950 °C and 25-mbar

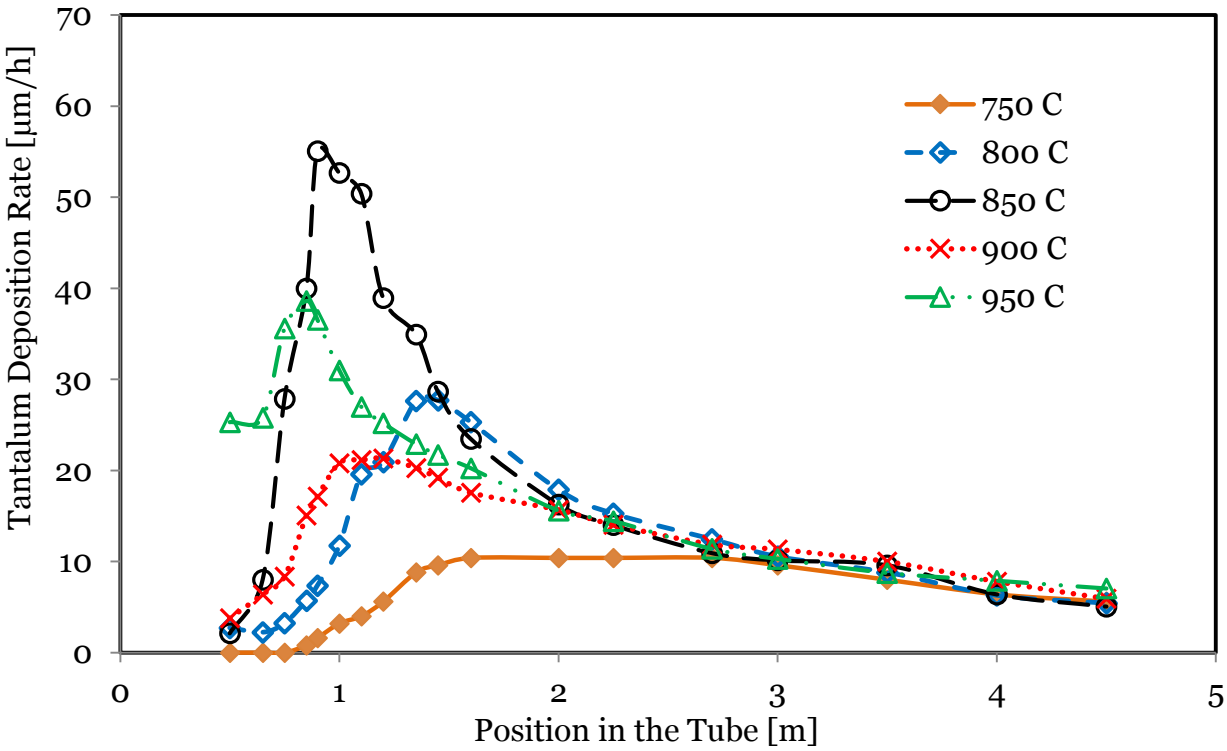

Figure 38: Tantalum deposition rate profiles at 700 – 950 ^{O}C and 25-mbar

Figures 33 – 38 show the deposition profiles for the temperature range of 750 – 950 ^{O}C at 25-mbar. The graphs show that the experimental data for the range of 800 – 900 ^{O}C (Figure 34 - 36) is reproducible while that at 950 ^{O}C (figure 37) seems to have a stochastic element and is non-reproducible. The experiment at 750 ^{O}C was only done once so the reproducibility of it is unknown. It can be observed that there is a gradual increase in deposition rate, with temperature, from 750 – 850 ^{O}C and then a decrease at 900 ^{O}C. The deposition rates at 950 ^{O}C (figure 37) are inconclusive i.e. sometimes lower than what is observed at 900 ^{O}C while other times higher. Taking an average of the seemingly random deposition rates observed at 950 ^{O}C gives a deposition profile that suggests that the rate picks up again and starts increasing with temperature from 900 – 950 ^{O}C as seen in Figure 38.

6.2.2 Effect of System Pressure at constant Feed rate

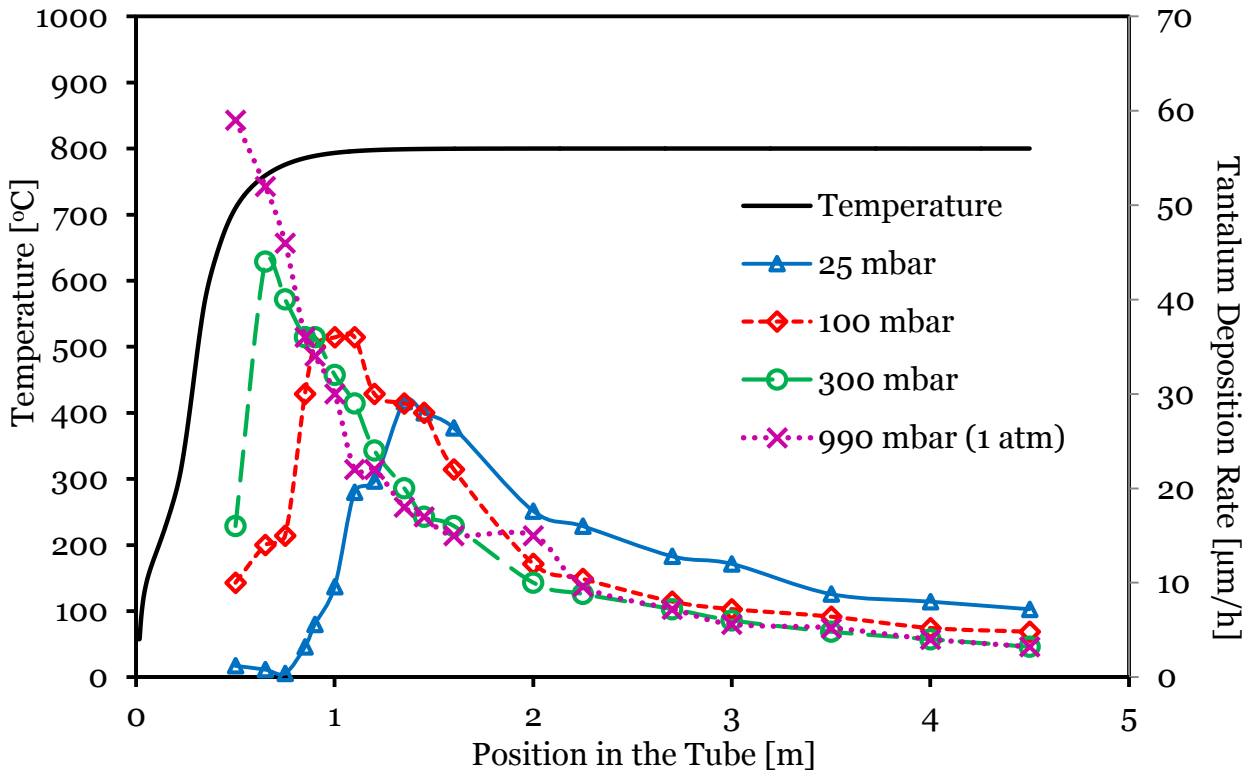

Figure 39: Tantalum deposition rate profiles at 25 mbar, 100 mbar, 300 mbar and 1 atm. T=800 °C

Figure 39 shows the deposition rate profiles along the tube for different system pressures and similar gas feed rates. It is important to note that increasing the deposition pressure in such a system not only changes the partial pressures of the gas components but also their instantaneous residence times in the tube. The higher pressures can only be achieved by applying lower pumping speeds and/or by restricting the downstream flow area by the use of a throttling device (e.g. a needle valve). This directly implies that an increase in the system pressures, without changing the gas feed rates, is synonymous with slower gas flows and a lower pressure drop from the tube inlet to the outlet.

Changing the deposition pressure clearly has a significant effect on the profile along the tube. The peak deposition rate happens earlier (at shorter tube length) and has a higher value when the pressure is increased than at lower pressures.

This is what would be expected because the increase in precursor partial pressure as a result of increasing system pressure leads to higher reaction rates at the tube inlet, that is typically cooler than the rest of the tube. In addition to that, the slower flow velocity means that the precursor rich feed gas has a higher instantaneous residence time allowing for a larger extent of reaction to be achieved in a shorter distance.

However, it is also important to observe that the effect of changing the system pressure seems to diminish at higher pressures. The deposition profiles at 300 mbar and 990 mbar (ca. 1 atm) are very

similar and can only be distinguished by observing the first 0.65 m of the tube; they are otherwise identical profiles.

6.2.3 Effect of Precursor Partial Pressure and Residence time at different Feed rates

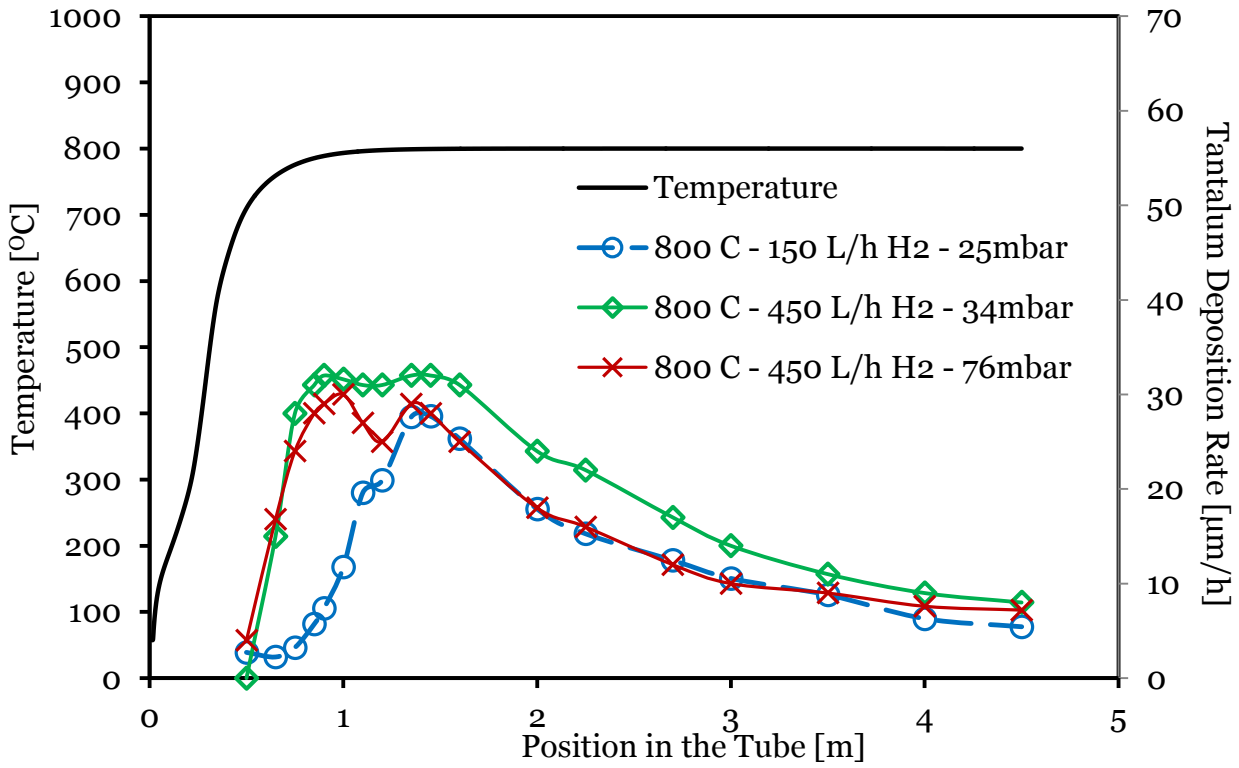

Figure 40: Effect of partial pressure and residence times on the deposition profiles

The experiments shown in figure 40 have been carefully designed to probe specific aspects of the deposition mechanism. The experiments at 25 mbar and 76 mbar have similar gas component partial pressures and flow rates (residence times) but the absolute pressures are different and so are the gas molar compositions. All the CVD experiments are being done in excess hydrogen atmosphere and therefore the volumetric flow of the system is determined by the hydrogen feed rate. Tripling the hydrogen feed rate from 150 L/h to 450 L/h also triples the volumetric flow rate in the system but this is then countered by also tripling the system pressure. The result is a system where the gas component partial pressures and volumetric flow are similar to the former, albeit with different molar compositions and absolute pressure.

The reaction reaches the peak deposition rate earlier in the 76 mbar experiment than the 25 mbar one although the partial pressures and residence time (related to the volumetric flow rate) are similar. Furthermore, both profiles seem to merge after 1.35 m in the tube, which is probably a

coincidence because at this point the reaction systems should have very different gas compositions due to the different extents of reaction.

The experiment at 34 mbar (25 mbar intended by not obtainable) is designed to have a third of the precursor feed partial pressure and a third the reactor residence time (three times the volumetric flow rate) when compared to that at 76 mbar. However, despite the difference in precursor feed partial pressure and instantaneous residence times, the reaction onset in both cases is the same and both reactions reach the peak deposition rate at a tube distance of 0.85m. Moreover, the peak deposition rates are similar with a 3% difference. This shows that although the feed partial pressure and instantaneous residence times play a role in where the peak deposition rate appears, as explained in section 6.2.2; there are more unknown contributions as the explanation given in the previous section cannot be used on its own to account for what is observed here.

A more detailed explanation is suggested based on the kinetic study and is given in the modelling results. See section 6.4.5.

6.3 Characteristics of the deposited Tantalum

6.3.1 Cross Sections

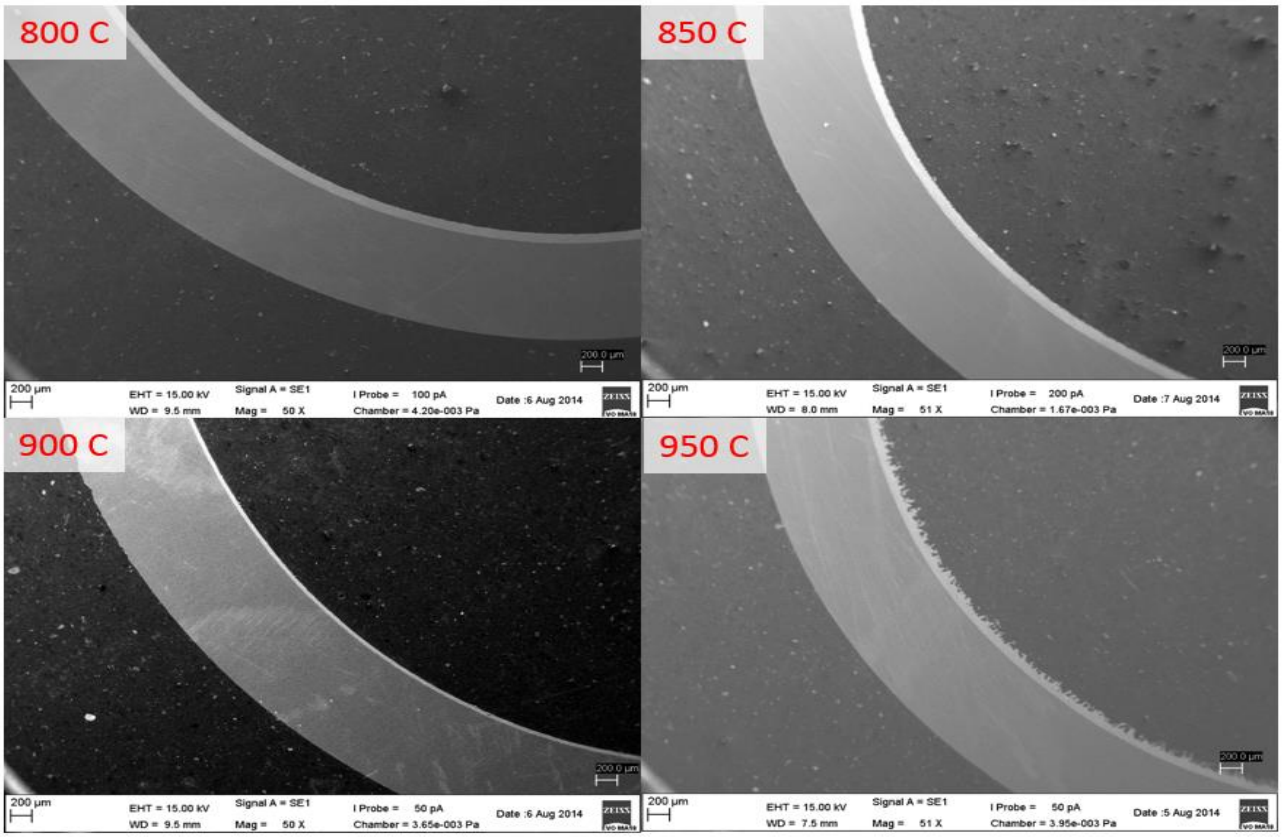

Figure 41: Scanning Electron Microscope (SEM) cross section images at x50 mag. Process Pressure = 25 mbar; Flows = (150 L/h of H_2, 5 L/h of Ar & 50 grams/ h of Cl_2). All micrographs are taken at the point of peak deposition rate

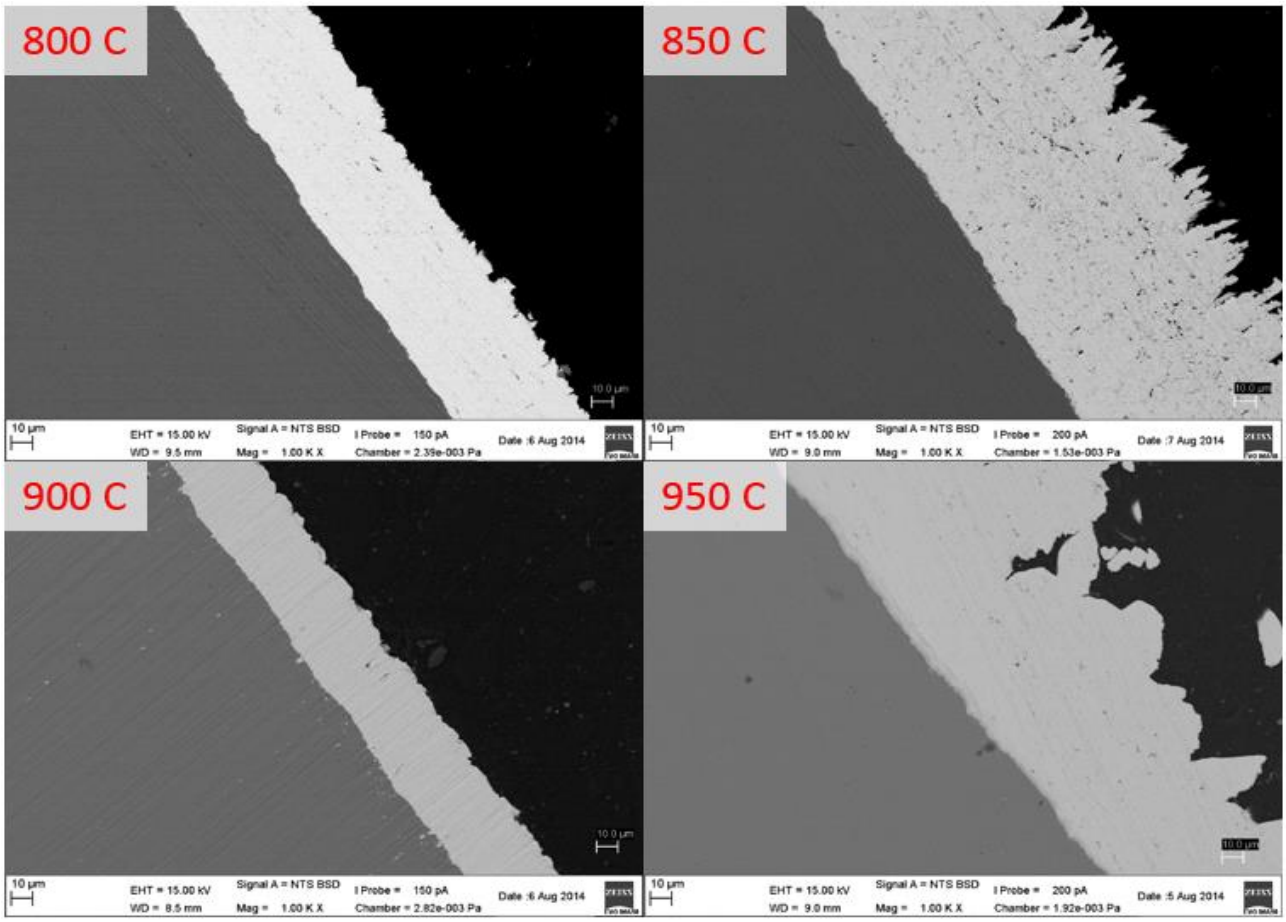

Figure 42: SEM cross section images at x1000 magnification. Process Pressure = 25 mbar; Flows = (150 L/h of H_2, 5 L/h of Ar & 50 grams/ h of Cl_2)

Figures 41 and 42 show cross sections of the tantalum layer on the tube surface at different temperatures. Figure 41 is aimed at emphasizing that the deposited layer has a consistent morphology over large areas of the tube at all temperatures; while figure 42 highlights the differences between the layers when temperature is varied.

Figure 42 shows that the layers deposited at 800 ^{O}C and 900 ^{O}C seem to have relatively flat surfaces when compared to those deposited at 850 ^{O}C and 950 ^{O}C. The layer deposited at 950 ^{O}C is clearly the roughest one since not even the low magnification of figure 41 can conceal its ruggedness.

6.3.2 Alloying Interface

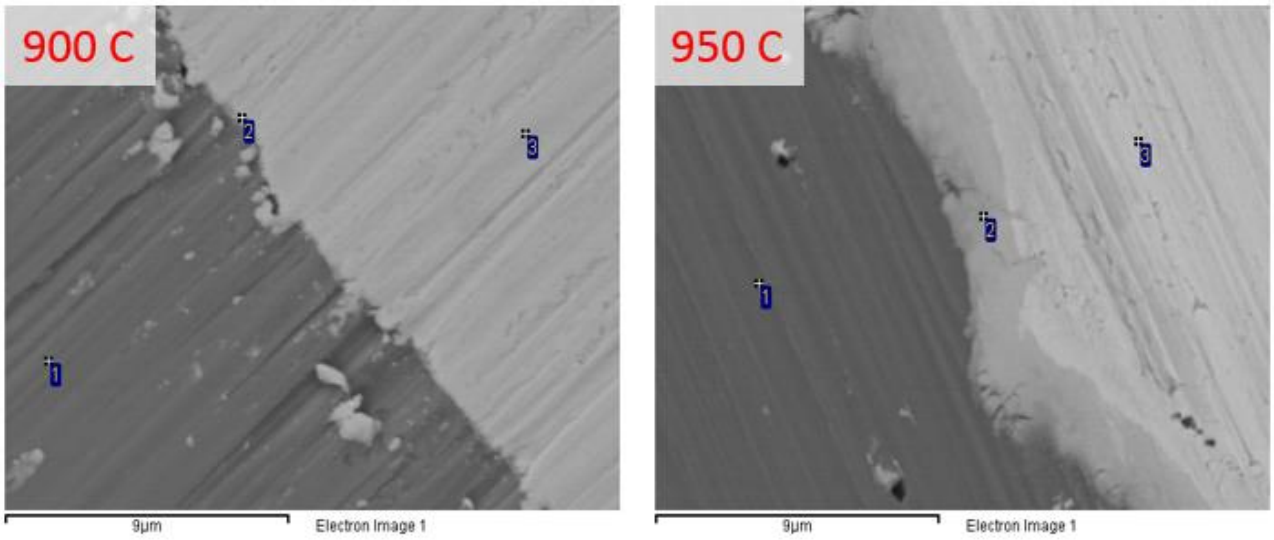

Figure 43: SEM images showing the alloy interface between the tantalum and steel

Table 5: Energy Dispersive X-ray spectroscopy for the spectra at 900 ^{O}C. Results in weight %

Spectrum	C	O	Cr	Mn	Fe	Ni	Mo	Ta	Total
Spectrum 1	1.59		17.64	1.72	64.10	12.61	2.33		100.00
Spectrum 2	5.22	1.78	1.09		2.63			89.28	100.00
Spectrum 3		1.03						98.97	100.00

Table 6: Energy Dispersive X-ray spectroscopy for the spectra at 950 ^{O}C. Results in weight %

Spectrum	C	O	Cr	Mn	Fe	Ni	Mo	Ta	Total
Spectrum 1	2.64		17.29	1.81	62.70	12.48	3.07		100.00
Spectrum 2	11.27	1.54	6.30		24.34	3.22	3.45	49.89	100.00
Spectrum 3	3.26	2.41						94.34	100.00

Figure 43 shows the interface between steel (dark grey) and tantalum (white) at 900 ^{O}C and 950 ^{O}C. Tables 5 and 6 show the energy dispersive x-ray (EDX) spectra for the interfaces and the surrounding regions.

Similar images for 800 ^{O}C and 850 ^{O}C are also shown in appendix B, and are left out here because they are not visually distinguishable from the image taken at 900 ^{O}C.

EDX spectra from the areas marked '1' only show the components of stainless steel and no tantalum at all; while those from the area marked '3' show pure tantalum with traces of carbon from the edge retention matrix and traces of oxygen due to the passivation of tantalum in air.

Spectra from the area marked '2' show that the interface between the stainless steel and tantalum is an alloy zone in which the two materials have inter-diffused.

This alloying zone is clearly much larger at 950 ^{O}C than at the lower temperatures. The alloy zones at the lower temperatures are less than 0.5 µm thick while that at 950 ^{O}C is between 2 - 3 µm thick. This is due to the fact that inter-metallic diffusion happens faster at higher temperatures than at lower ones.

6.3.3 Effect of temperature on the Surface Characteristics

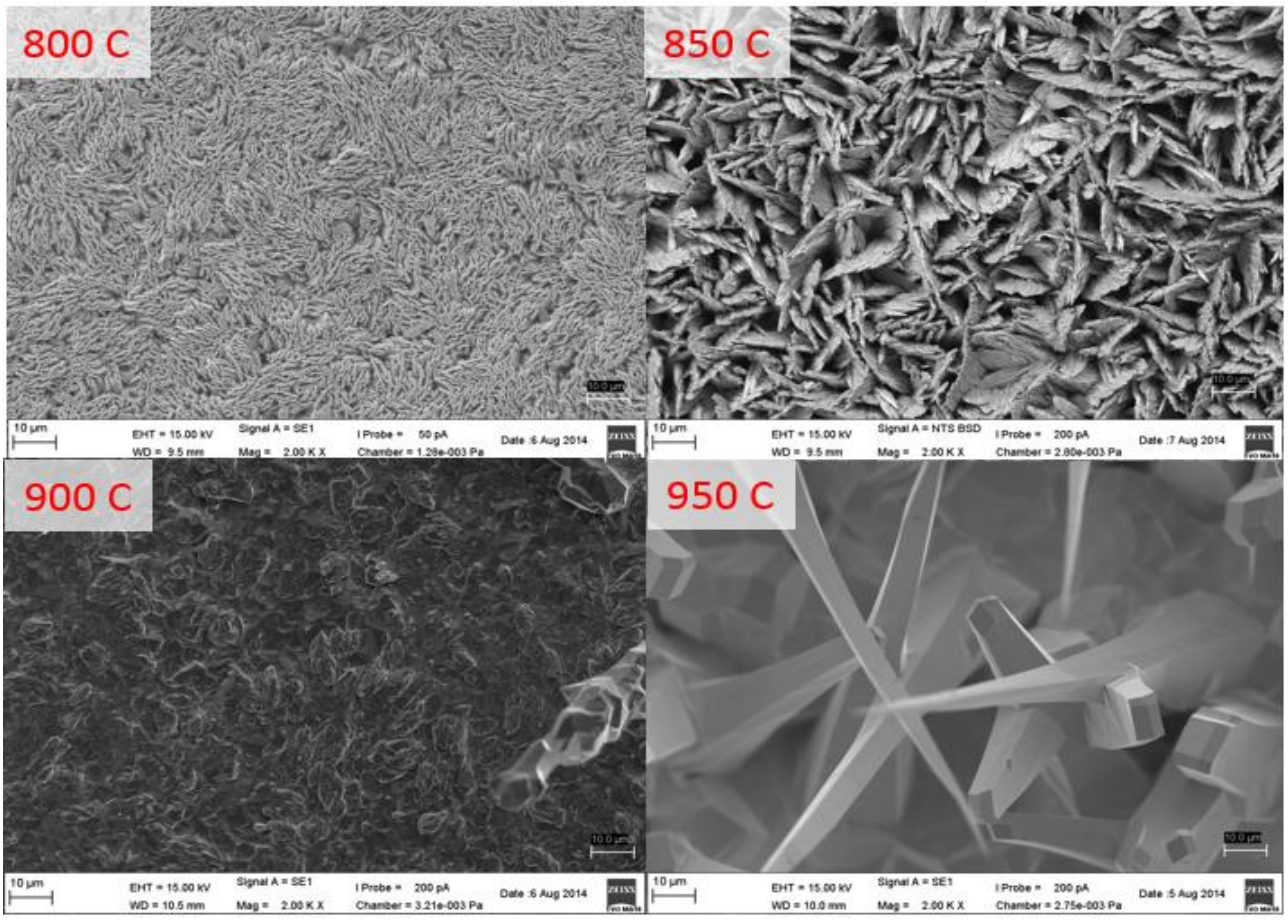

Figure 44: SEM image of the surface of the deposited tantalum layer at x2000 magnification. Process Pressure = 25 mbar; Flows = (150 L/h of H_2, 5 L/h of Ar & 50 grams/ h of Cl_2); All micrographs are taken at the point of peak deposition rate

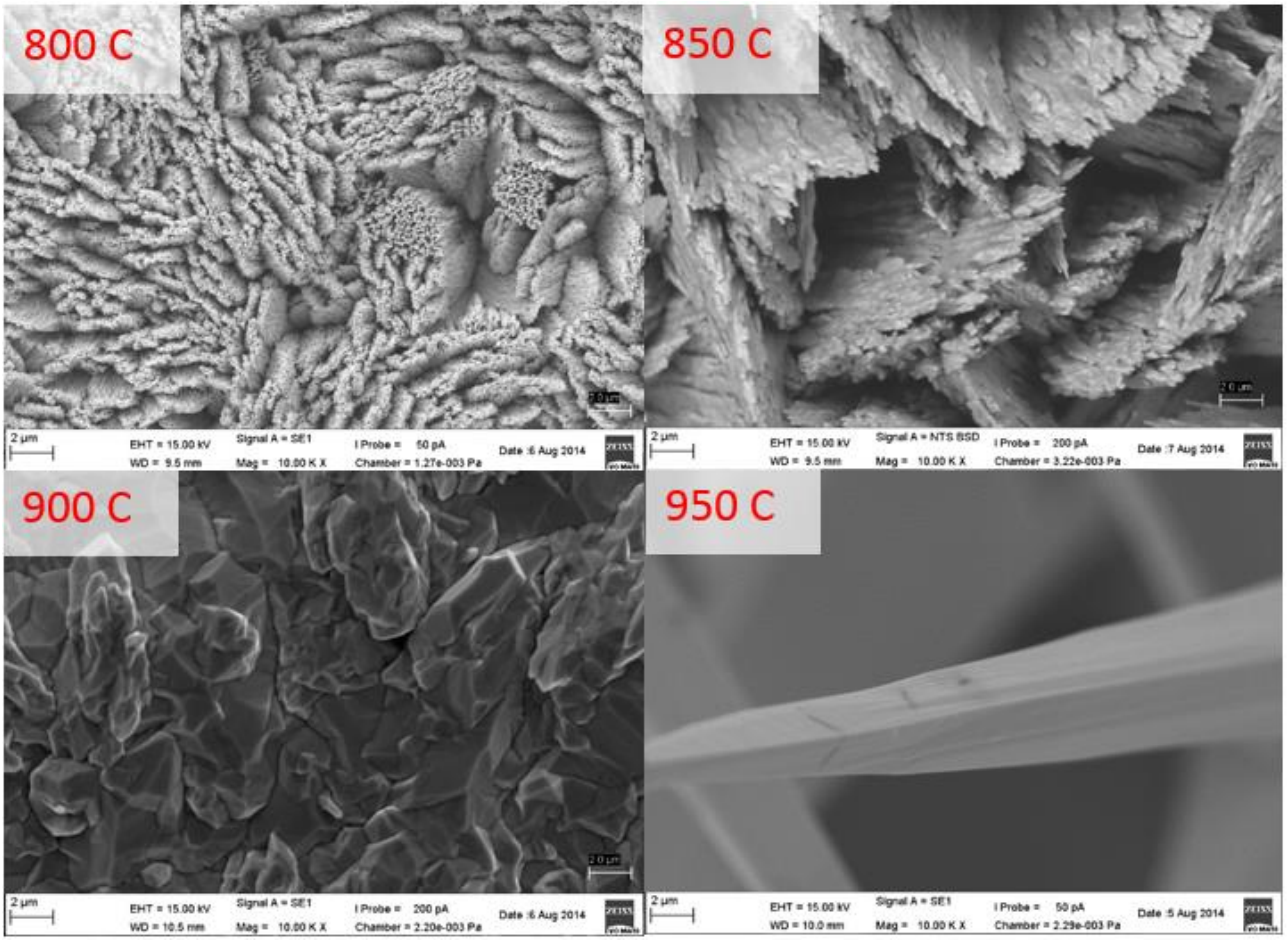

Figure 45: SEM image of the surface of the deposited tantalum layer at x10000 magnification. Process Pressure = 25 mbar; Flows = (150 L/h of H_2, 5 L/h of Ar & 50 grams/ h of Cl_2)

Figures 44 and 45 show that reaction temperature has a large influence on the morphology of the deposited layer. At 800 ^{O}C, the layer seems to be consisting of several vertical whiskers emanating from the substrates surface. Based on the cross sections in figure 42, it is thought that these whisker structures are only predominant on the surface of the deposited layer since the bulk of the layer does not appear to be porous.

The appearance of the surface at 850 ^{O}C is quite similar to that at 800 ^{O}C however, the whiskers seem to be amalgamated into flaky ridge-like structures giving the appearance of a rougher surface.

At 900 ^{O}C the surface looks dense and rugged but with no significant protrusions. Comparing figures 44 & 45 with figure 42 suggests that the layer is dense in its entirety at this temperature.

Looking at figures 41 - 45 shows that the surface structure obtained at 950 ^{O}C is extremely rough. Figure 44 shows the structure to consist of interwoven dendrites, crisscrossing and merging with one another. The cross-sections in figures 41 and 42 show that the bulk of the deposited layer is dense. Figure 45 shows that these dendrites are much larger than the whiskers and flaky ridges seen at 800 ^{O}C and 850 ^{O}C, respectively.

6.3.4 Effect of Pressure on the Surface Characteristics at 800 ^{0}C

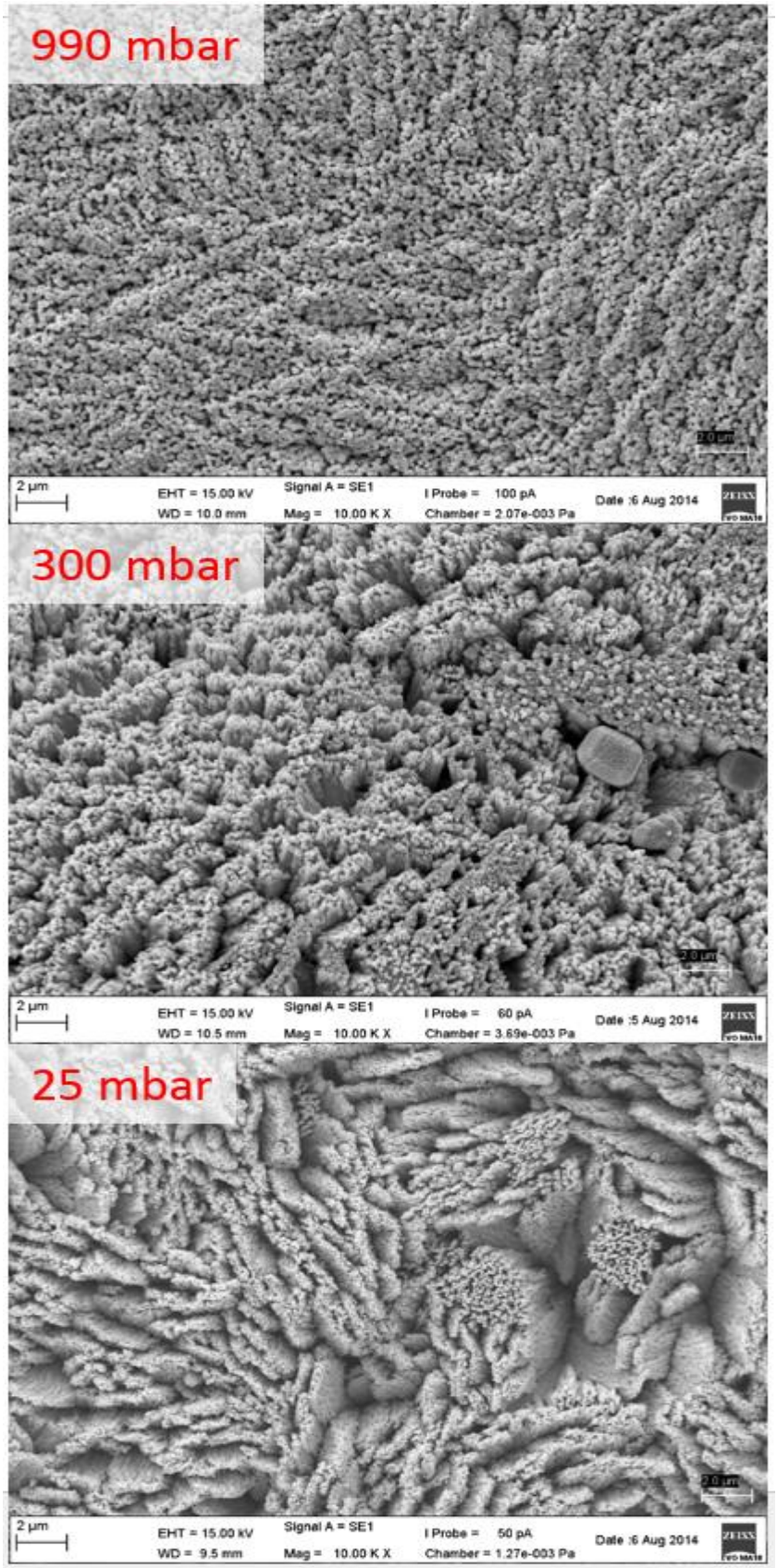

Figure 46: SEM image of the surface of the deposited tantalum layer at x10000 magnification. Temperature = 800 ^{0}C (All micrographs are taken at the point of peak deposition rate)

The surfaces of tantalum layers deposited at 800 ^{0}C but with different system pressures were also compared to determine whether the reaction pressure has any effect on the surface morphology. Looking at figure 46 shows that at all pressures, the structure consists of whiskers albeit with slightly different ordering. The structure obtained at 990 mbar (ca. 1 atm) has evenly distributed whiskers with uniform spacing between them, while that at 300 mbar shows the whiskers to be less evenly distributed with relatively large gaps in some places. At 25 mbar, the whiskers appear to form clusters with 'pathways' and gaps between them.

This tendency for the whiskers to group together at lower pressures is most likely due to the more vigorous flow patterns expected at low pressures i.e. higher flow velocities with more eddies and swirls; hence the 'pathways' between the clusters. Only the arrangement of the whiskers seems to be affected by changing the pressure, the individual whiskers themselves look unaffected.

The layers deposited at different pressures are clearly distinguishable at 800 ^{0}C, whether this is true at other temperatures is matter for future investigations.

The reaction temperature appears to have the most significant effect on the nature of the deposited layer as the variations due to pressure seem to be flow-pattern effects.

6.4 Model Results

6.4.1 Inputs – Gas Properties

6.4.1.1 Viscosity

The viscosity is calculated using the method shown in section 4.3.1 for the temperature range of 400 – 1300K. All the necessary data is taken from reference [49] and [41] Appendix A, sections A and B.

Table 7: Viscosity of Mixture Compared to that of Hydrogen

Temperature (K)	Viscosity of H2 (μP) or (x10^{-7} Pa·s)	Viscosity of H2 – Ar Mixture (Pa·s) X_{Ar}=0.032	Ratio η_{MIX}/η_{H2}
400	109.1	326.6	2.99
600	144.2	325.7	2.26
700	160.4	324.8	2.02
800	175.9	324	1.84
900	190.9	323	1.69
1000	205.4	322.4	1.57
1100	219.5	321.8	1.47
1300	252.96	320.94	1.27

All the experiments in this project were done within the temperature range of 1000 – 1300 K therefore; it is safe to assume that the viscosity of the gas mixture and that of pure hydrogen will have the relation:

$\eta_{MIX} = \gamma \cdot \eta_{H_2}$ Where $1.27 \le \gamma \le 1.57$

The proportionality constant, γ, was taken to be 1.5 because that is what matched the pressure drops measured across the system during the experiments. The pressure drops are shown in figures 47 - 52.

6.4.1.2 Thermal Conductivity

The thermal conductivities are calculated using the method shown in section 4.3.2 for the temperature range of 500 – 1300K. All the necessary data is taken from reference [49] and [41] Appendix A, sections A and B. The thermal conductivities of the pure elements are taken from Yaws C. L. [50].

Table 8: Thermal Conductivity of Mixture Compared to that of Hydrogen

Temperature (K)	**Thermal Conductivity of H_2 k_{H_2} in (W/m·K)**	**Thermal Conductivity of the H_2 – Ar Mixture. k_{MIX} in (W/m·K) X_{Ar}=0.032**	**Ratio k_{MIX}/k_{H_2}**
500	0.26925	0.25797	0.9581
1000	0.428592	0.40817	0.9524
1100	0.45501	0.43226	0.9500
1300	0.5034	0.478	0.9495

Table 8 shows that within the temperature range of 500 – 1300K the thermal conductivity of the gas mixture can always be approximated by multiplying that of Hydrogen by 0.95.

Therefore:

$K_{MIX} = 0.95 \cdot K_{H_2}$

6.4.1.3 Specific Heat Capacity

The Specific heat capacity of the gas mixture is calculated as shown in section 4.3.4. The values for the pure substances are taken from work by *Barin et. al.* [51]

Table 9: Specific Heat Capacity of Mixture Compared to that of Hydrogen

Temperature (K)	**Cp of H2 (J/Kg·K)**	**Cp of Ar (J/Kg·K)**	**Cp of TaCl5 (J/Kg·K)**	**Cp of Mixture (J/Kg·K)**	**Ratio Cp_{MIX}/Cp_{H_2}**	**Ratio of Specific Heats (Cp/Cv)**
500	29.260	20.786	128.06	32.86	1.123	1,34
600	29.326	20.786	129.46	32.98	1.125	1,34
700	29.442	20.786	130.32	33.12	1.125	1,39
800	29.625	20.786	130.89	33.31	1.124	1,33
900	29.880	20.786	131.30	33.57	1.123	1,33
1000	30.205	20.786	131.60	33.88	1.122	1,33
1100	30.579	20.786	131.83	34.24	1.12	1,32
1300	31.429	20.786	132.16	35.04	1.115	1.31

Table 9 shows that there is a consistent relation between the specific heat capacity of hydrogen and that of the standard gas mixture: X_{Ar}=0.031, X_{TaCl_5}=0.039 and X_{H_2}=0.93.

Therefore, it can be assumed with a high degree of accuracy that:

$$Cp_{MIX} = 1.12 \cdot Cp_{H_2}$$

and

The ratio of specific heats, $\frac{Cp_{MIX}}{Cv_{MIX}} = 1.33$

6.4.1.4 Diffusion Coefficient

The diffusion coefficient of the precursor in the gas system was determined for a specific temperature and pressure according to the method in section 4.3.5, and was then scaled to other temperatures and pressures based on equation 59.

The diffusion coefficient was calculated to be 0.01255 m²/s at 1098K and 25 mbar; and this was scaled to other temperatures and pressures using the expression:

$$D_i = D_0 \cdot \left(\frac{T_i}{T_0}\right)^{3/2} \cdot \left(\frac{p_0}{p_i}\right) \text{ [42]} \qquad \text{Equation 59}$$

6.4.2 Verification of the Model Inputs

The input parameters estimated in the previous section are important in obtaining an accurate output from the laminar flow module of the model. Since this is a gaseous system, determining the correct system pressures is of unparalleled importance because it is by this that the reactant partial pressures will be calculated, based on their mole fractions. For this reason, the pressure drop across the reactor - from the inlet to the outlet – was chosen as the fitting criterion to verify the reliability of the laminar flow outputs. By comparing the observed (measured) pressures to the values predicted by the model, it was verified that the estimated input parameters are reliable as shown by figures 47 - 52. Note that the inlet and outlet pressures are measured at the positions labelled P_{IN} and P_{OUT}, in figure 29, to prevent damage of the equipment caused by solidification of the precursor.

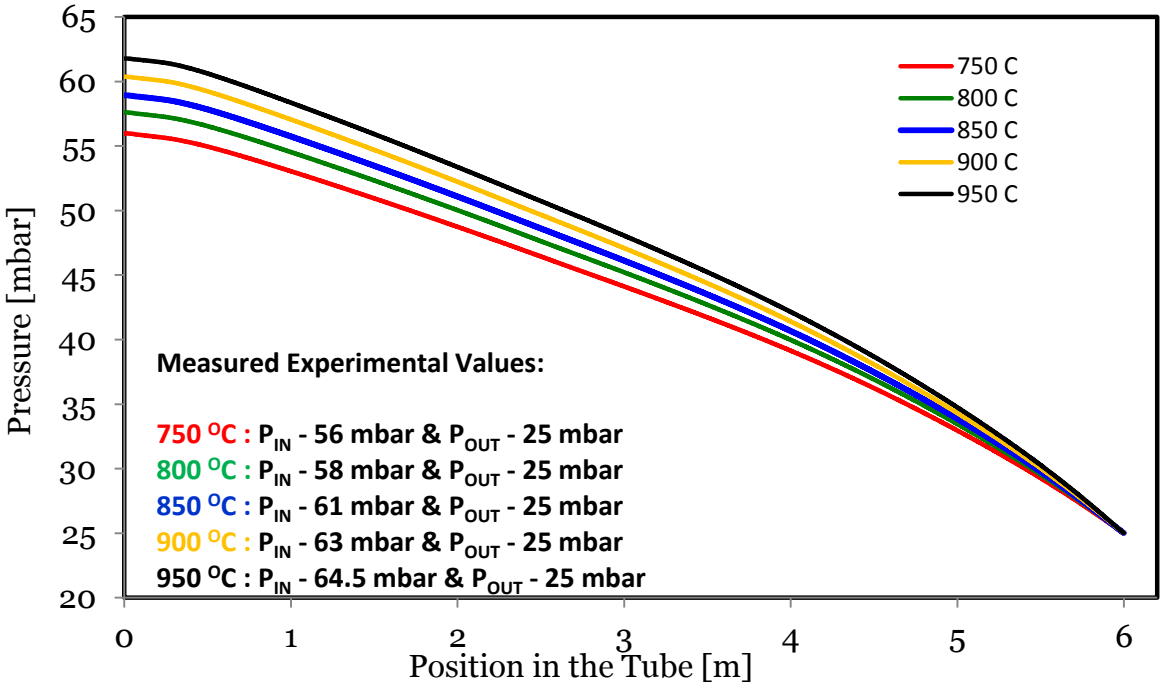

Figure 47: Simulated pressure curve from the tube inlet to the outlet for the **25-mbar** experiments

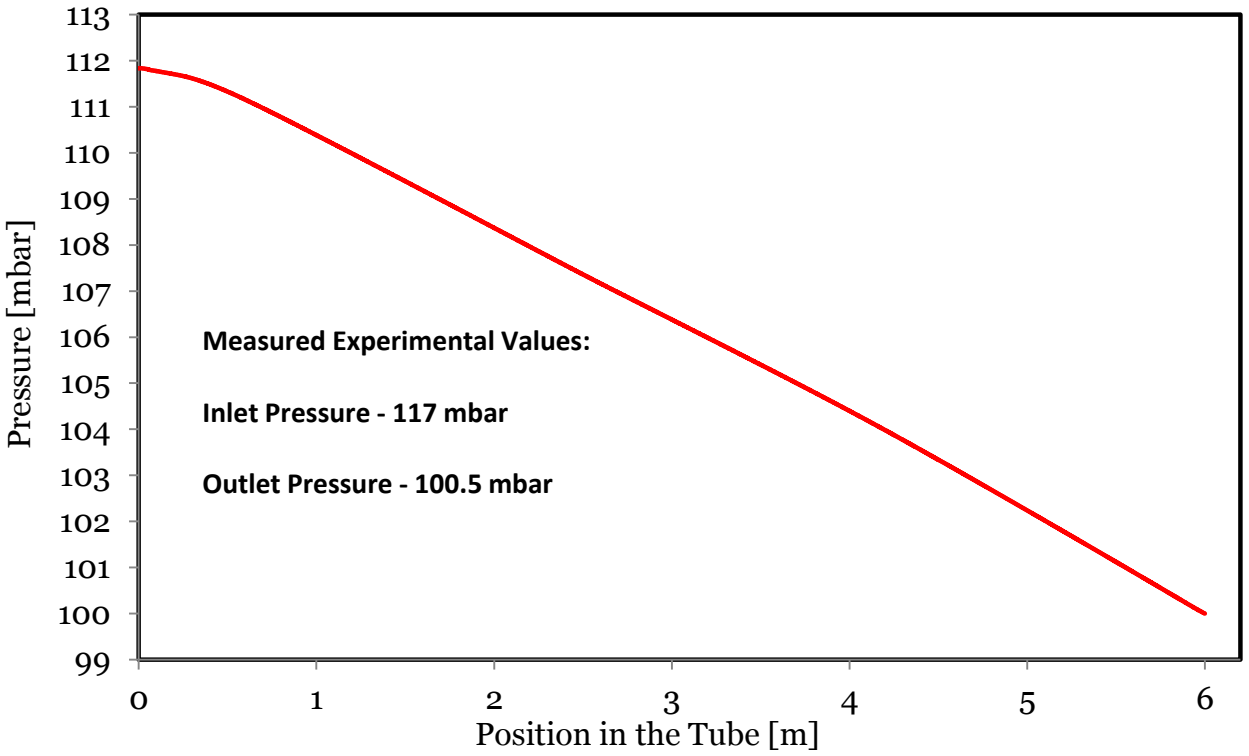

Figure 48: Simulated pressure curve from the tube inlet to the outlet for the **100-mbar** experiment

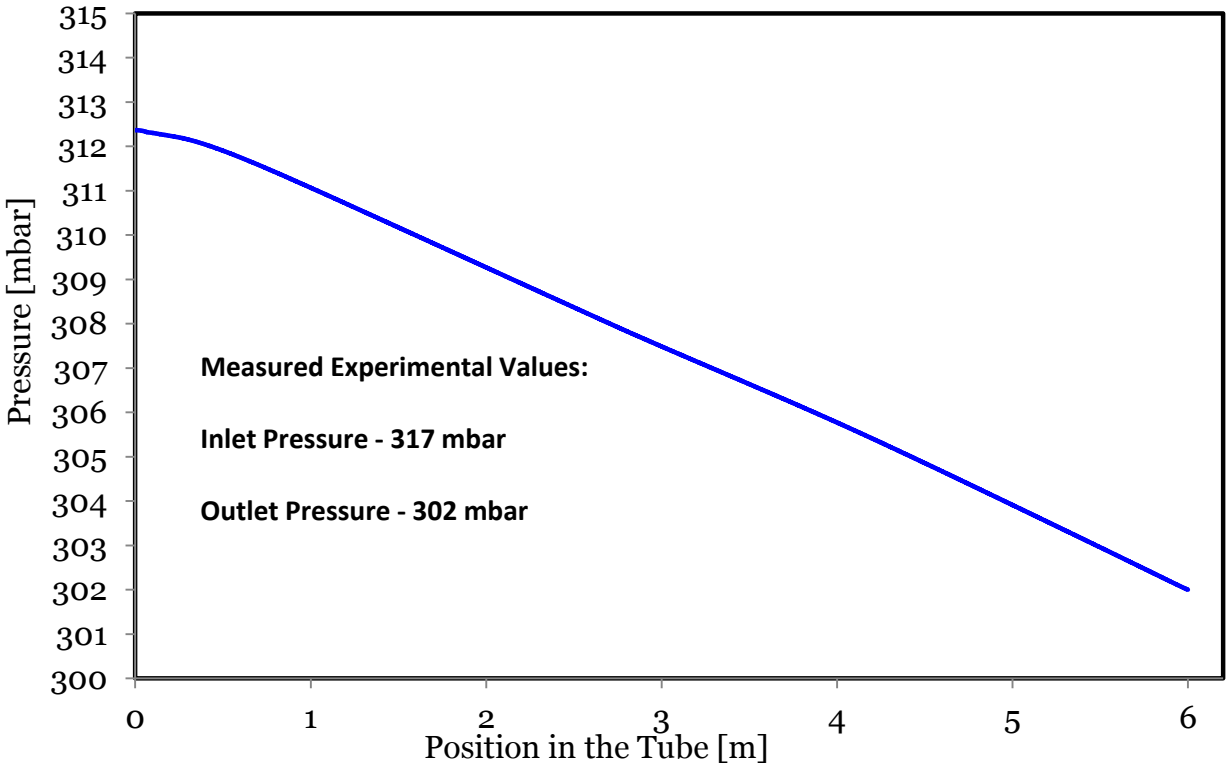

Figure 49: Simulated pressure curve from the tube inlet to the outlet for the **300-mbar** experiment

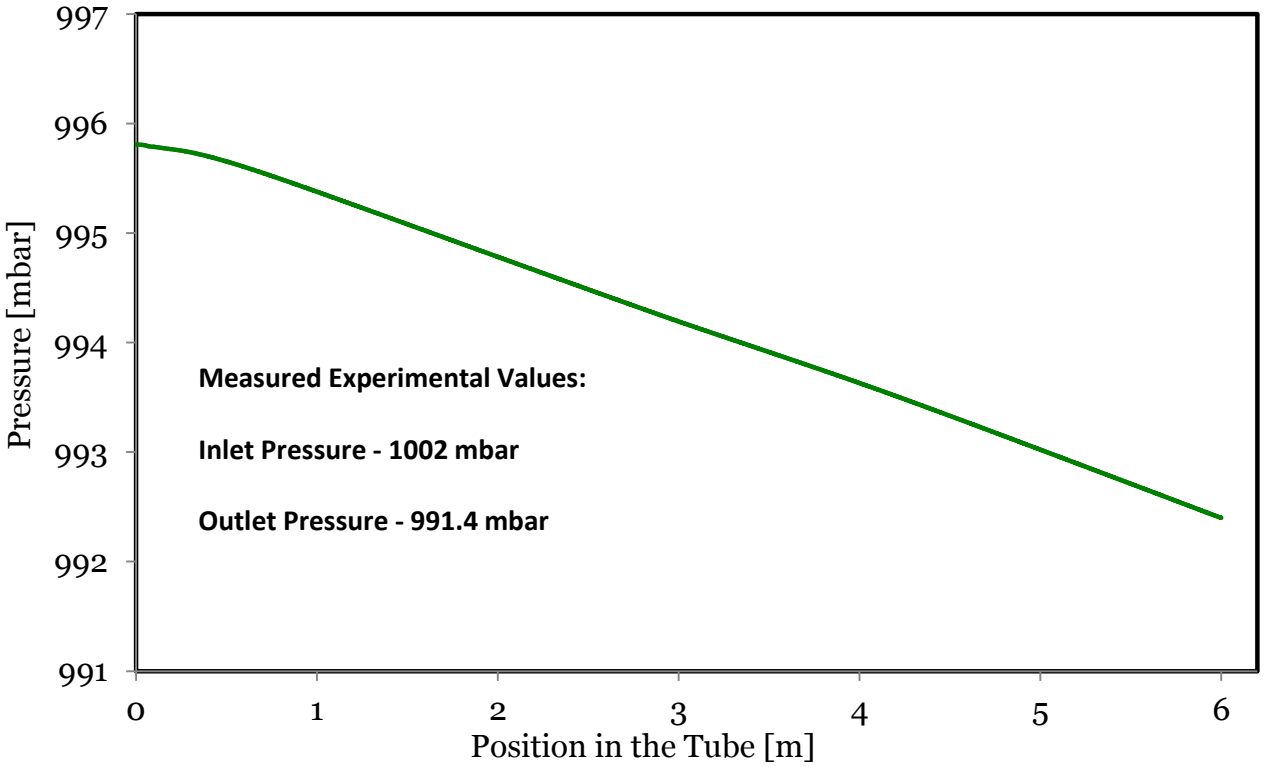

Figure 50: Simulated pressure curve from the tube inlet to the outlet for the **990-mbar** experiment

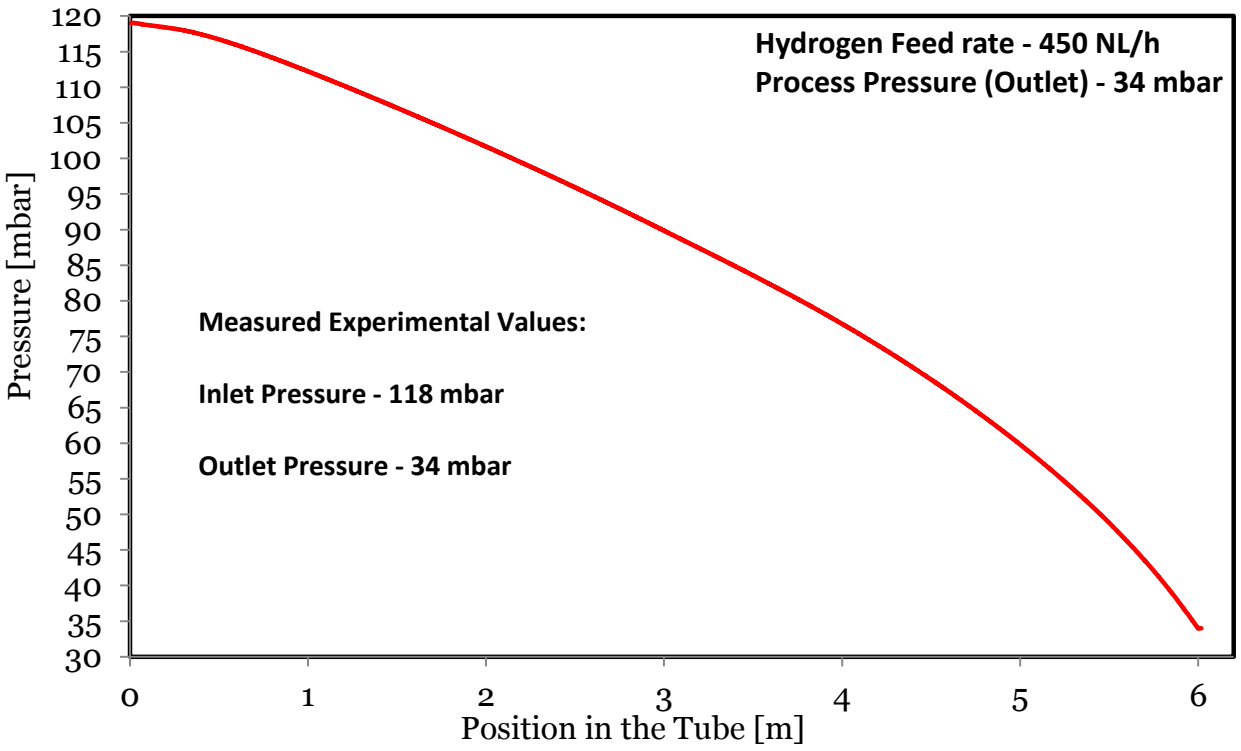

Figure 51: Simulated pressure curve from the tube inlet to the outlet for the **450 L/h H2** & **34-mbar** experiment

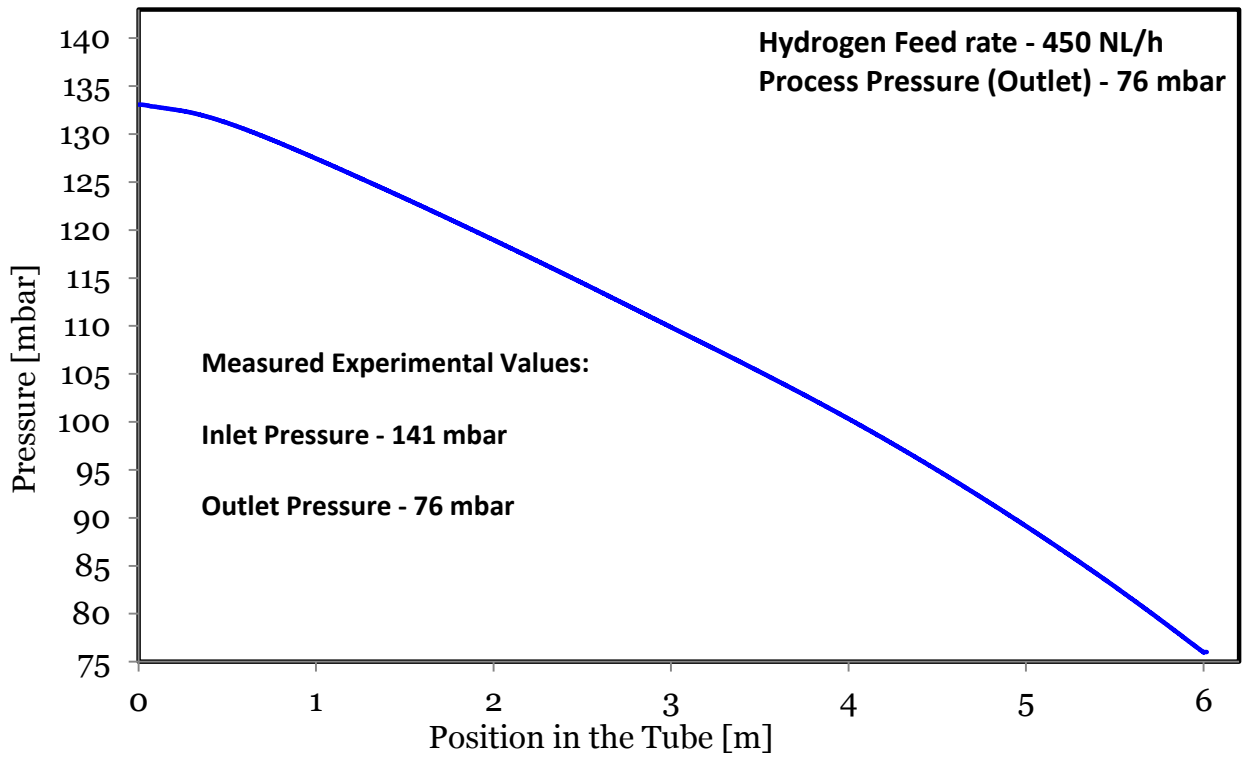

Figure 52: Simulated pressure curve from the tube inlet to the outlet for the **450 L/h H2** & **76-mbar** experiment

Looking at figures 47 - 52 shows that there is a very good agreement between the simulated pressures and those measured during the experiments. This means that the laminar flow module of the model is accurate and its output is very close, or similar, to the flow patterns that the tube has in practice. The thermal (heating and cooling) part of the model was already verified as reliable in previous work by the author. [27]

Once the flow and thermal simulations are satisfactory, their outputs are used as a basis (or input) for the reaction and diffusion module of the model.

The reaction and diffusion module (*Transport of Diluted Species in COMSOL*) is then run while fully coupled with an optimisation module called SNOPT – Sparse Nonlinear OPTimizer.

This optimization task generally tries to minimize an objective function provided by the user and in this case it is a Least Mean Square (LMS) expression that relates the reaction rates at the tube wall to the experimentally observed deposition rates. The minimisation is done by trying different values of the control variables until the lowest possible objective is reached. The control variables are values such as activation energies, reaction enthalpies and pre-exponential factors suggested and implemented by the user (the author in this case).

Therefore, the final output of such an analysis is a set of control variable values, e.g. activation energies, which provide the lowest achievable value for the objective function that in turn is synonymous with the best possible fit between theoretical curve and experimental data.

6.4.3 Final Model Equations and Constants

The kinetic part of the CVD model was implemented as described in the chapters 4.2.4 and 4.2.5. The gas phase reaction equations 23 - 25 were modelled as simple first order reactions governed by the Arrhenius expression thus giving rise to three activation energies and three pre-exponential factors as shown:

Reaction 1: $TaCl_{5(g)} + \frac{1}{2}H_{2(g)} \rightarrow TaCl_{4(g)} + HCl_{(g)}$

$$rate\,1 = C_1 \cdot pTaCl_5 = A_1 \cdot e^{-EA_1/R \cdot T} \cdot pTaCl_5 \qquad \text{Equation 60}$$

Where

C_1 is the reaction constant for Reaction 1
A_1 is the Pre - exponetial factor for Reaction 1
EA_1 is the activation energy for Reaction 1
$pTaCl_5$ is the partial pressure of $TaCl_5$
R is the idea gas constant
T is the Temperature

Likewise

Reaction 2: $TaCl_{4(g)} + \frac{1}{2}H_{2(g)} \rightarrow TaCl_{3(g)} + HCl_{(g)}$

$$rate\,2 = C_2 \cdot pTaCl_4 = A_2 \cdot e^{-EA_2/R \cdot T} \cdot pTaCl_4 \qquad \text{Equation 61}$$

Where

C_2 is the reaction constant for Reaction 2
A_2 is the Pre - exponetial factor for Reaction 2
EA_2 is the activation energy for Reaction 2
$pTaCl_4$ is the partial pressure of $TaCl_4$

And

<u>Reaction 3</u>: $TaCl_{3(g)} + \frac{1}{2} H_{2(g)} \rightarrow TaCl_{2(g)} + HCl_{(g)}$

$$rate\ 3 = C_3 \cdot pTaCl_3 = A_3 \cdot e^{-EA_3/R \cdot T} \cdot pTaCl_3 \qquad \text{Equation 62}$$

Where

C_3 is the reaction constant for Reaction 3
A_3 is the Pre - exponetial factor for Reaction 3
EA_3 is the activation energy for Reaction 3
$pTaCl_3$ is the partial pressure of $TaCl_3$

The surface reactions shown in equations 26 - 29 were modelled as first order Langmuir based surface reactions. It was quickly found that the optimizer (SNOPT) always nullifies the deposition of both TaCl5 and TaCl2 in order to get anywhere close to a reasonable fit with the experimental data. Furthermore, it is already known from section 3.6.2 that TaCl5 is not stable under the conditions in which the deposition reaction happens. For these reasons both TaCl5 and TaCl2 were considered not to be surface active and not to directly contribute to the deposition of tantalum on the surface. They are however accounted for in the gas phase interactions as previously shown.

The deposition rates of the surface-active chlorides TaCl4 and TaCl3 are then accounted for such that:

$$Deposition\ rate = C_r \cdot N_{Sites} \cdot \Theta = A_r \cdot e^{-EA_r/R \cdot T} \cdot N_{Sites} \cdot \frac{\alpha \cdot pTaCl_x}{1 + \alpha \cdot pTaCl_4 + \beta \cdot pTaCl_3} \qquad \text{Equation 63}$$

Where:

- α and β are the adsorption equilibrium constants for TaCl4 and TaCl3 respectively.
- C_r is the reaction rate constant
- Θ is the surface coverage of the species depositing
- N_{sites} is the number of reaction sites per unit area of the surface
- A_r and EA_r are the pre-exponetial factor and activation energies corresponding to C_r

Both α and β can be described by the Van't Hoff expression:

$$Ln\,\xi = \frac{-\Delta H}{RT} + \frac{\Delta S}{R} \quad [52] \qquad \text{Equation 64}$$

Where:

- ΔH is the change in enthalpy for adsorption
- ΔS is the change in entropy for adsorption
- ξ represents either α or β

This led to two deposition rate expressions in the form of:

<u>*Reaction 4*</u>: $TaCl_{4(g)} + 2H_{2(g)} \rightarrow Ta_{(S)} + 4HCl_{(g)}$

$$Rate\ 4 = C_4 \cdot N_{Sites} \cdot \Theta_{TaCl4} = A_4 \cdot e^{-EA_4/R \cdot T} \cdot N_{Sites} \cdot \frac{\alpha \cdot pTaCl_4}{1 + \alpha \cdot pTaCl_4 + \beta \cdot pTaCl_3} \qquad \text{Equation 65}$$

And

<u>*Reaction 5*</u>: $TaCl_{3(g)} + \frac{3}{2}H_{2(g)} \rightarrow Ta_{(S)} + 3HCl_{(g)}$

$$Rate\ 5 = C_5 \cdot N_{Sites} \cdot \Theta_{TaCl3} = A_5 \cdot e^{-EA_5/R \cdot T} \cdot N_{Sites} \cdot \frac{\beta \cdot pTaCl_3}{1 + \alpha \cdot pTaCl_4 + \beta \cdot pTaCl_3} \qquad \text{Equation 66}$$

In both surface reactions: $Ln\,\alpha = \frac{-\Delta H_4}{RT} + \frac{\Delta S_4}{R}$ & $Ln\,\beta = \frac{-\Delta H_5}{RT} + \frac{\Delta S_5}{R}$

The entire kinetic model then consists of 15 variables to be optimized. The variables and their units are shown in Table 10.

Table 10: List of the used variables and their units

Reaction Number	**Activation Energy** [Unit]	**Pre-exponential Factor** [Unit]	**Enthalpy of Adsorption** [Unit]	**Entropy of Adsorption** [Unit]	**Number of Sites** [Unit]
Reaction 1	$EA1\left[\frac{J}{mol}\right]$	$A1\left[\frac{mol}{m^3 \cdot s \cdot Pa}\right]$			
Reaction 2	$EA2\left[\frac{J}{mol}\right]$	$A2\left[\frac{mol}{m^3 \cdot s \cdot Pa}\right]$			
Reaction 3	$EA3\left[\frac{J}{mol}\right]$	$A3\left[\frac{mol}{m^3 \cdot s \cdot Pa}\right]$			
Reaction 4	$EA4\left[\frac{J}{mol}\right]$	$A4\left[\frac{1}{s}\right]$	$\Delta H4\left[\frac{J}{mol}\right]$	$\Delta S4\left[\frac{J}{mol \cdot K}\right]$	$N_{Sites}\left[\frac{mol}{m^2}\right]$
Reaction 5	$EA5\left[\frac{J}{mol}\right]$	$A5\left[\frac{1}{s}\right]$	$\Delta H5\left[\frac{J}{mol}\right]$	$\Delta S5\left[\frac{J}{mol \cdot K}\right]$	$N_{Sites}\left[\frac{mol}{m^2}\right]$

Table 11: Reactions and their rate units

Reaction 1 (Homogeneous)	***Reaction 2 (Homogeneous)***	***Reaction 3 (Homogeneous)***	***Reaction 4 (Heterogeneous)***	***Reaction 5 (Heterogeneous)***
$\left[\frac{mol}{m^3 \cdot s}\right]$	$\left[\frac{mol}{m^3 \cdot s}\right]$	$\left[\frac{mol}{m^3 \cdot s}\right]$	$\left[\frac{mol}{m^2 \cdot s}\right]$	$\left[\frac{mol}{m^2 \cdot s}\right]$

6.4.4 Model fits and Partial Pressure Profiles

After running several optimization exercises, a set of values for the variables listed in table 10 was found that best fitted the experimental data.

The model fits well with all the experiments done at the temperatures 750 ^{O}C, 800 ^{O}C and 850 ^{O}C. It also fits well at all the pressures although its accuracy at the tube inlet noticeably falls as reaction pressure is increased.

The model did not fit the experiments done at 900 ^{O}C & 950 ^{O}C, giving large deviations; this is further discussed in section 6.4.5.

The model-to-experiment fits are shown in figures 53 - 78 and, a triplet of graphs represents each case:

The first graph in each triplet shows how the simulated overall deposition rate fits with the experimental data.

The second graph shows the simulated partial pressure profiles for each chloride of tantalum along the tube's length. These partial pressures are given in order to illustrate the prevalence of the different tantalum chloride species that result from the evolution of $TaCl_5$, through gradual hydrogen reduction.

The third graph in each triplet shows the individual contribution of each of the surface-active chlorides ($TaCl_4$ and $TaCl_3$) to the overall deposition rate.

While looking at the graphs, note that $TaCl_5$ quickly turns into $TaCl_4$ and then becomes $TaCl_3$. Furthermore, note that $TaCl_3$ is accounting for most of the tantalum deposition.

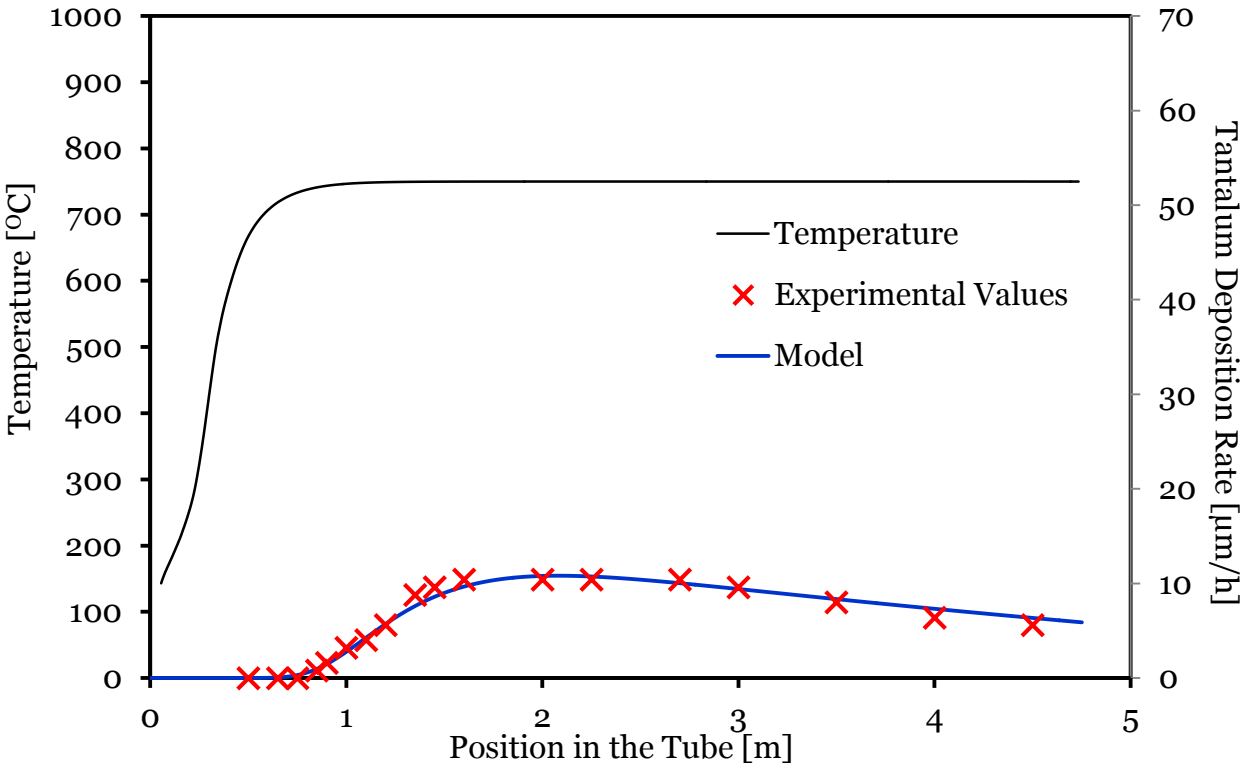

Figure 53: Model Fitting at: 750 °C & 25 mbar (150 L/h - H2, 5 L/h - Ar and 50 g/ h of Cl2

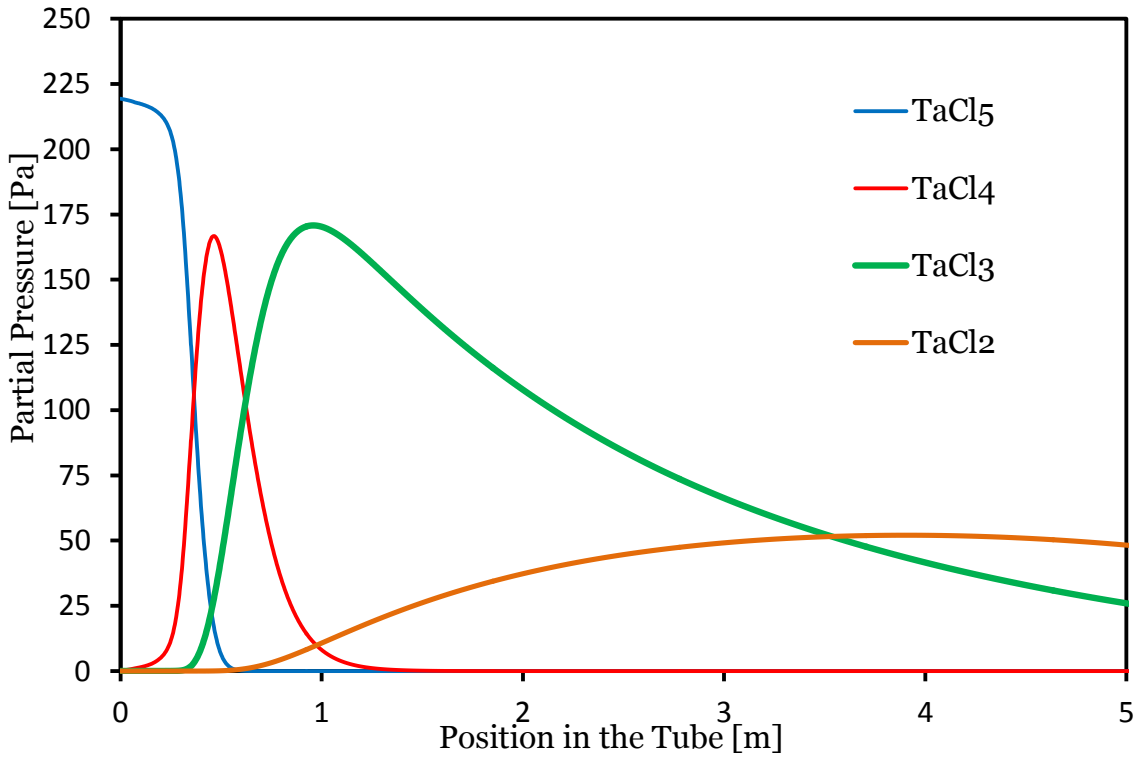

Figure 54: Simulated Partial Pressure profiles at: 750 °C & 25 mbar (150 L/h - H2, 5 L/h - Ar and 50 g/ h of Cl2

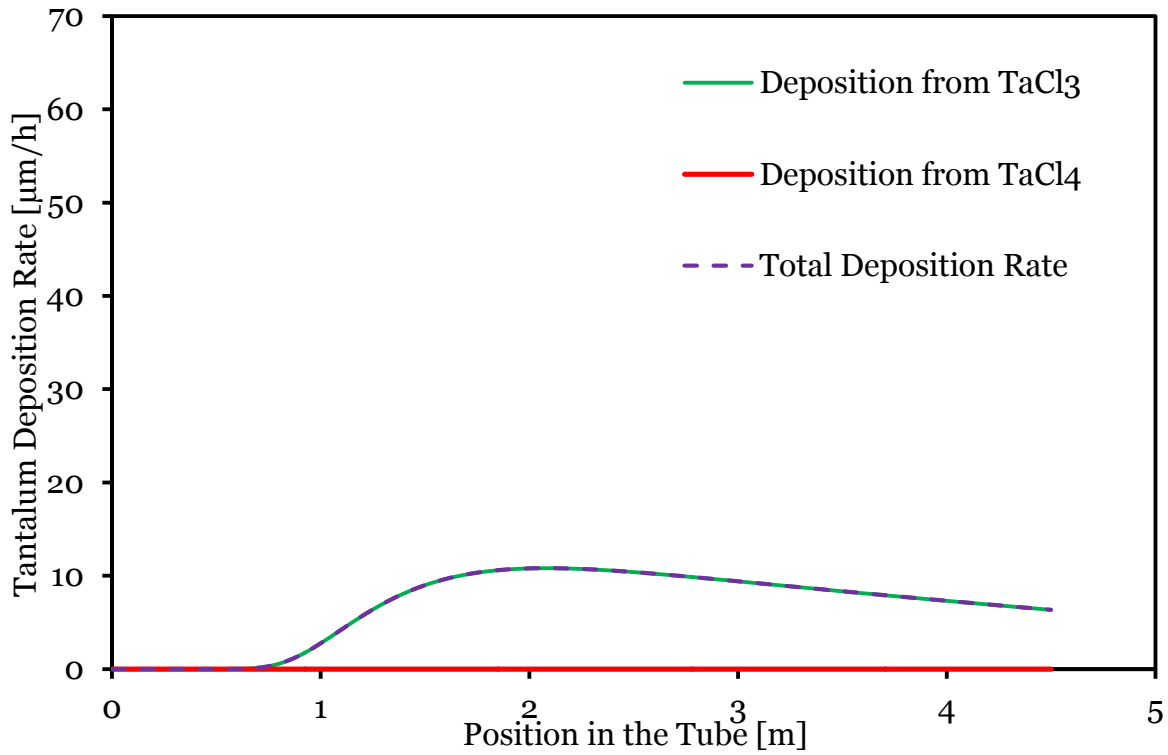

Figure 55: Distribution of the deposition rate at: 750 ^{O}C & 25 mbar (150 L/h - H2, 5 L/h - Ar and 50 g/ h of Cl2

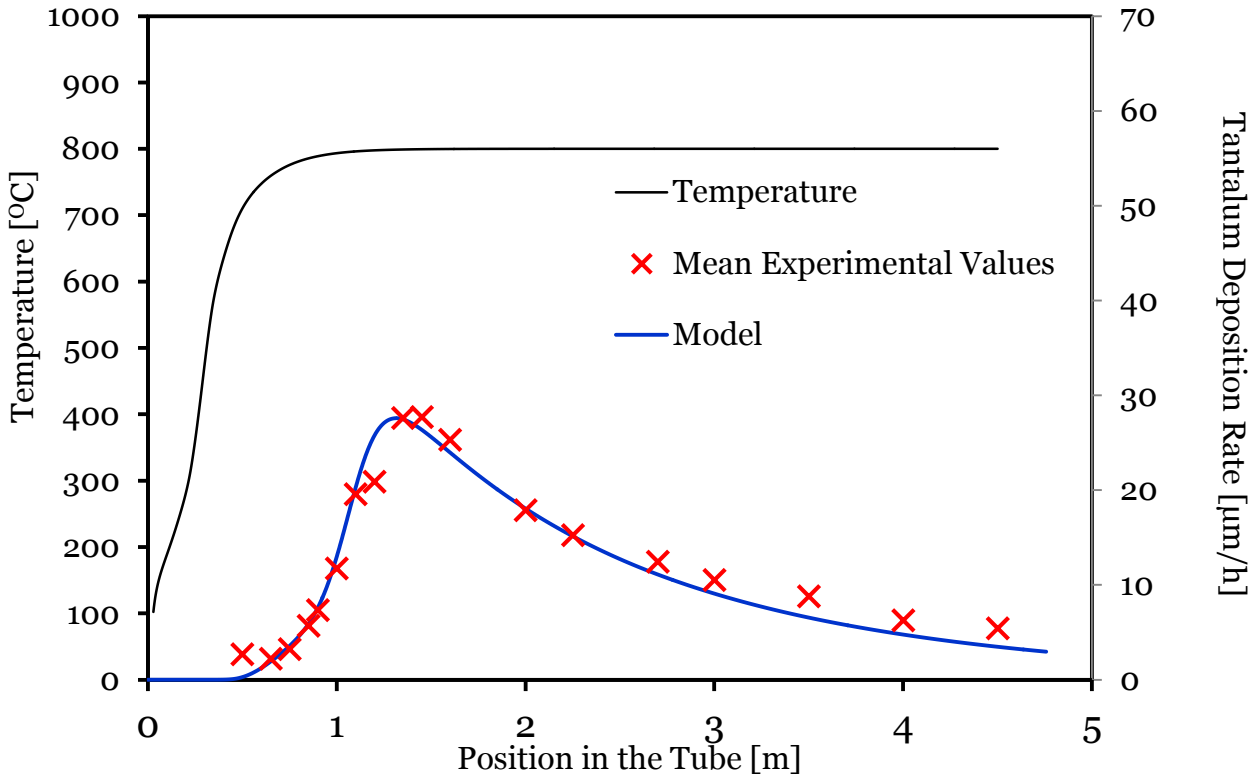

Figure 56: Model Fitting at: 800 °C & 25 mbar (150 L/h - H2, 5 L/h - Ar and 50 g/ h of Cl2

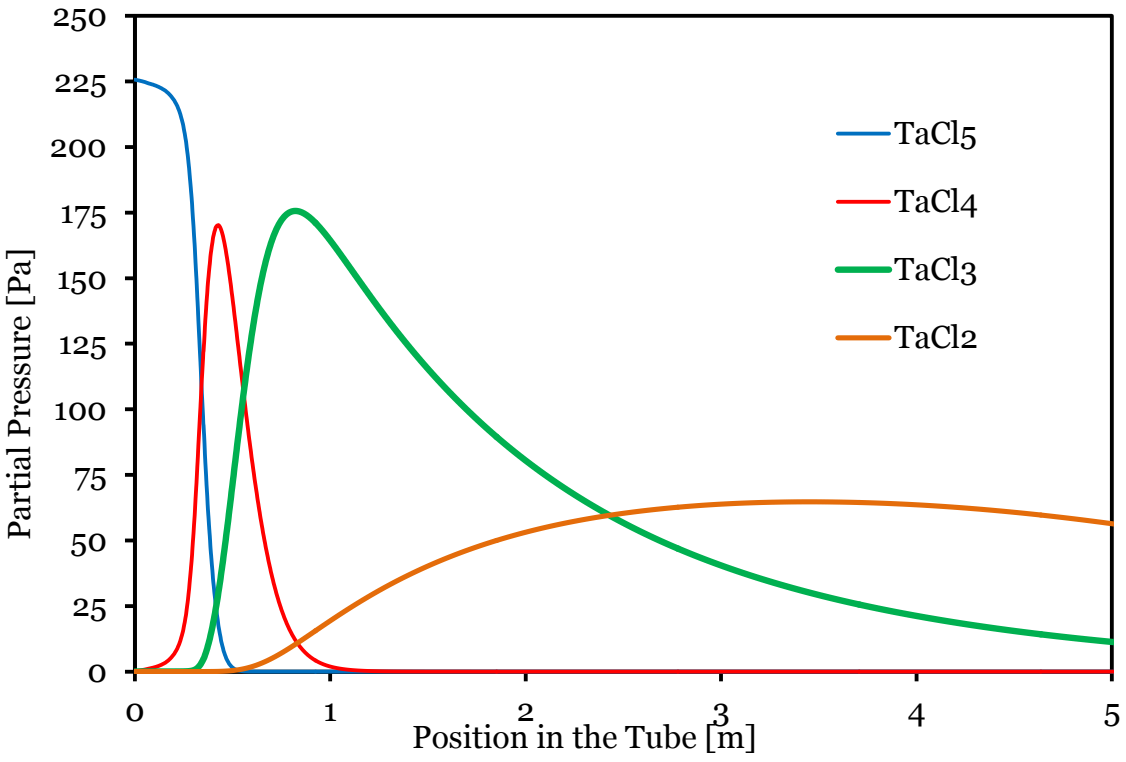

Figure 57: Simulated Partial Pressure profiles at: 800 °C & 25 mbar (150 L/h - H2, 5 L/h - Ar and 50 g/ h of Cl2

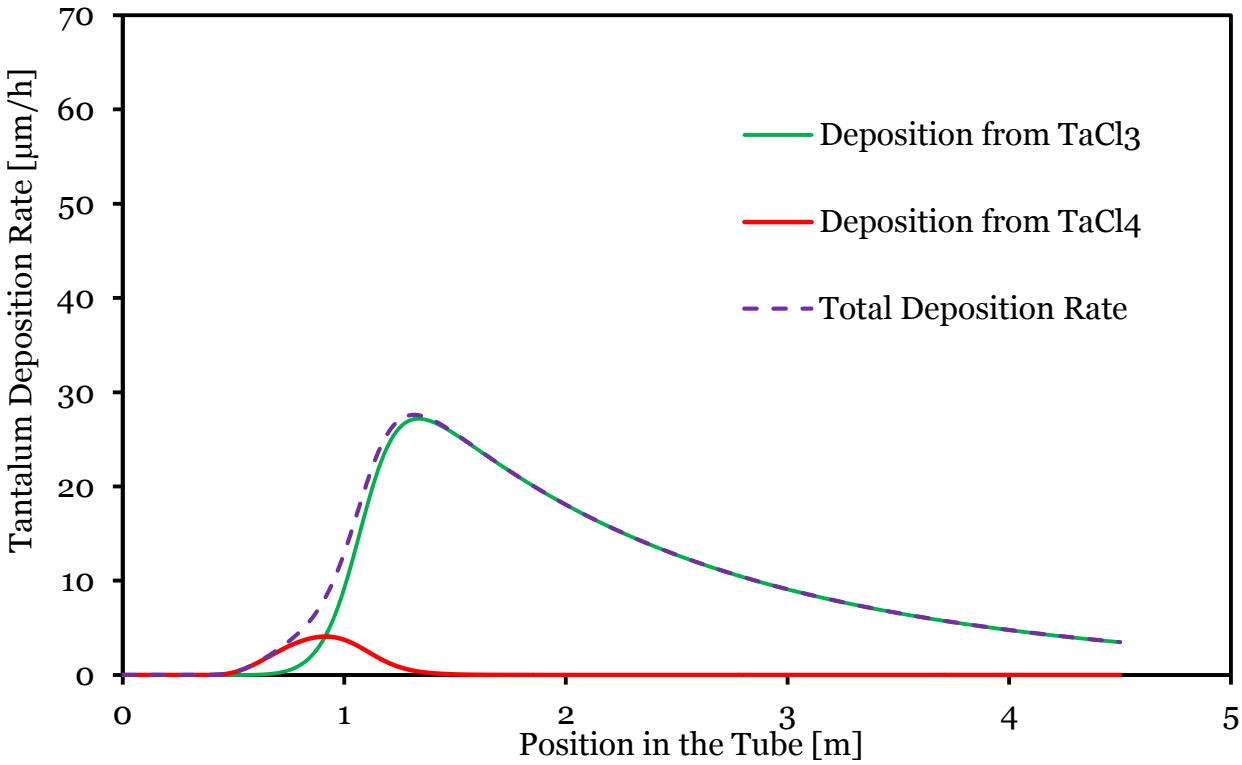

Figure 58: Distribution of the deposition rate at: 800 ^{O}C & 25 mbar (150 L/h - H2, 5 L/h - Ar and 50 g/ h of Cl2

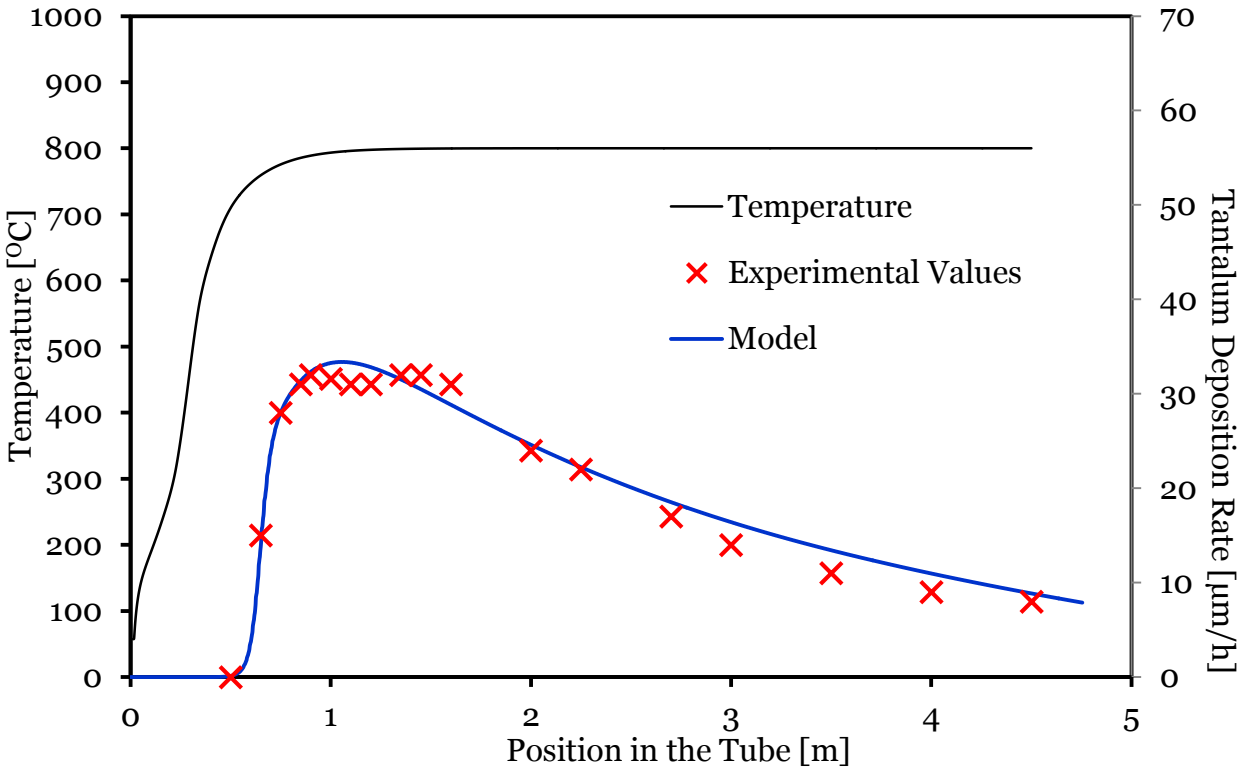

Figure 59: Model Fitting at: 800 °C & 25 mbar (450 L/h - H2, 5 L/h - Ar and 43 g/ h of Cl2. Secondary (backup) H2 flow meter is used.

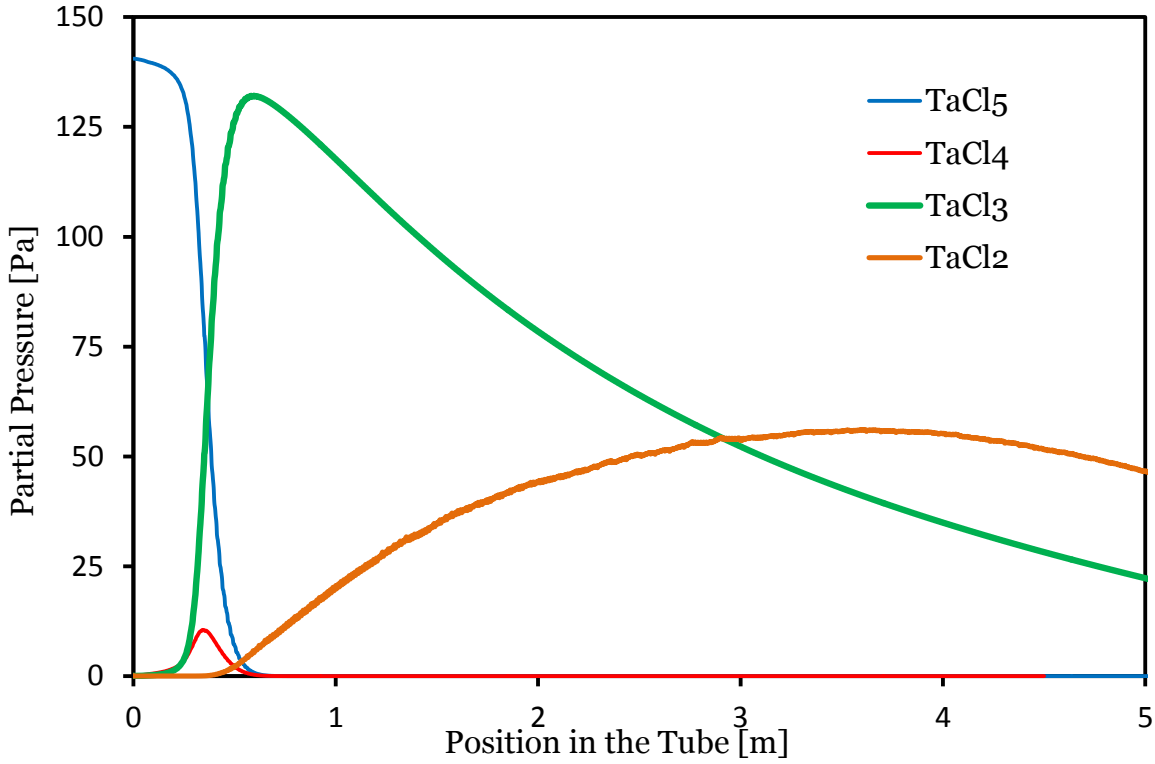

Figure 60: Simulated Partial Pressure profiles at: 800 °C & 25 mbar (450 L/h - H2, 5 L/h - Ar and 43 g/ h of Cl2

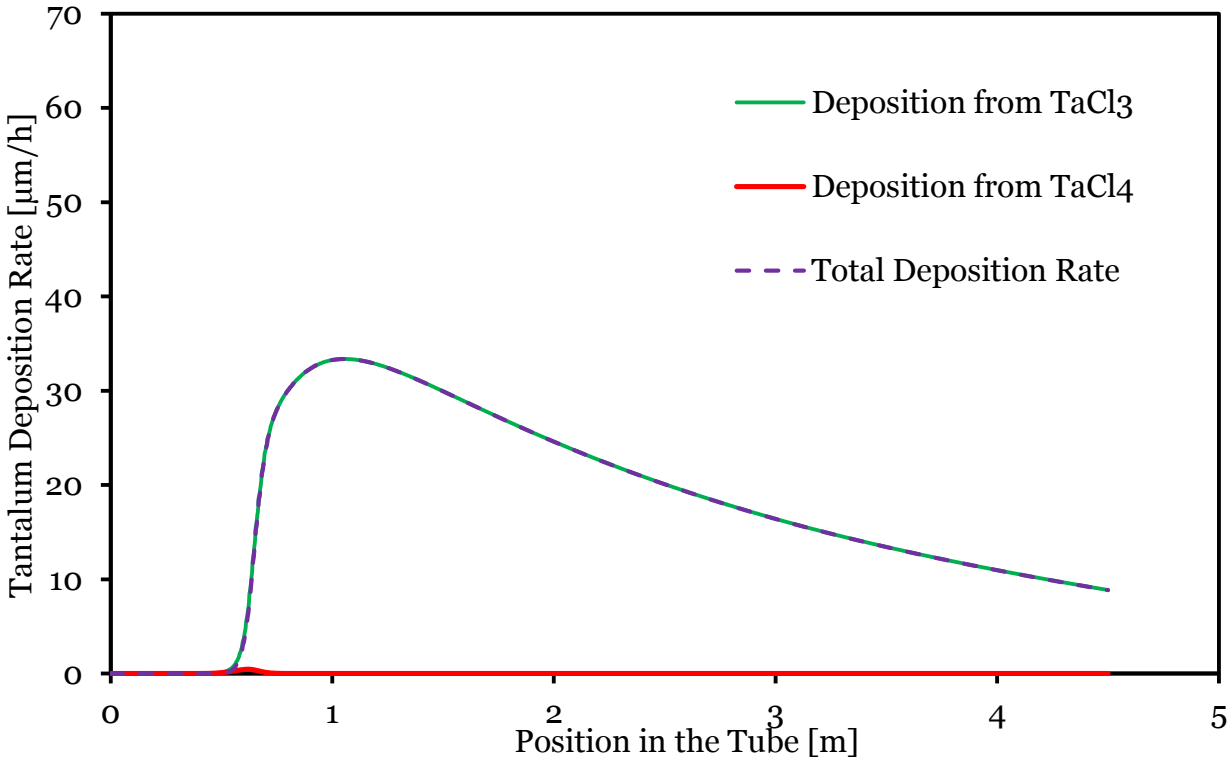

Figure 61: Distribution of the deposition rate at: 800 ^{O}C & 25 mbar (450 L/h - H2, 5 L/h - Ar and 43 g/ h of Cl2

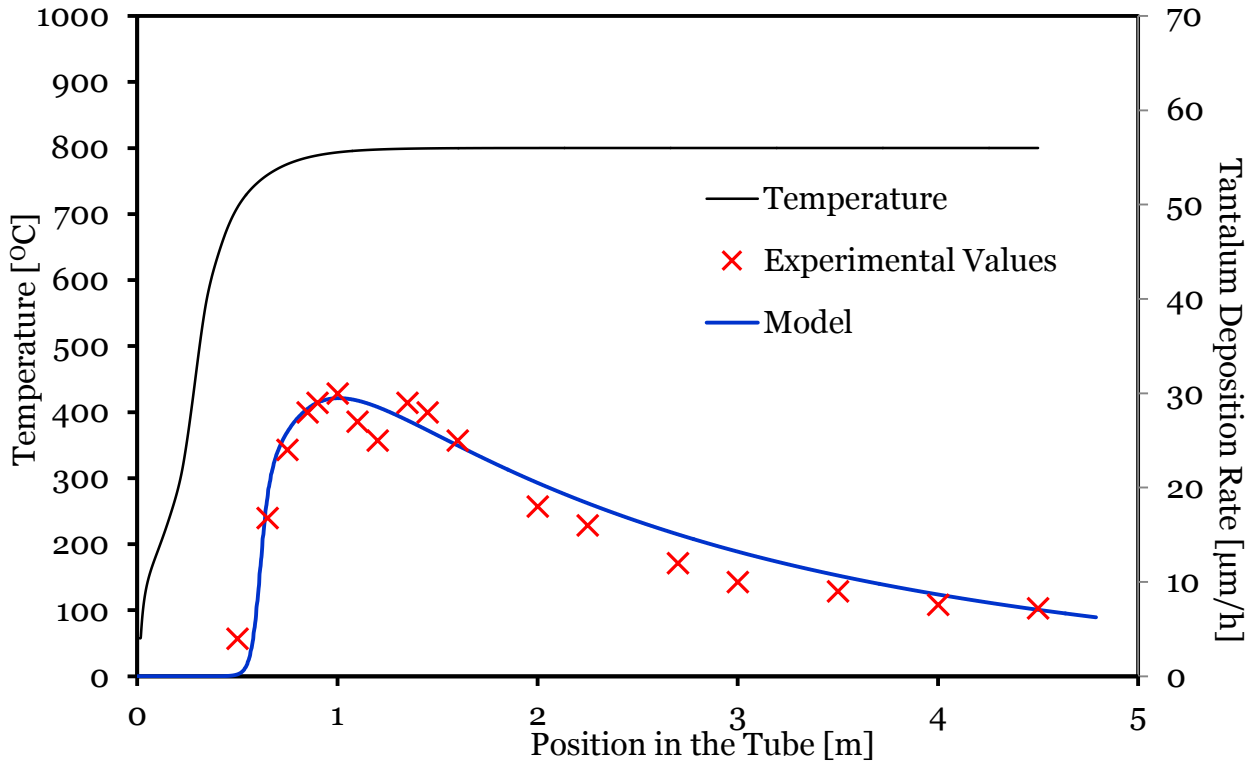

Figure 62: Model Fitting at: 800 °C & 76 mbar (450 L/h - H2, 5 L/h - Ar and 40 g/ h of Cl2. Secondary (backup) H2 flow meter is used.

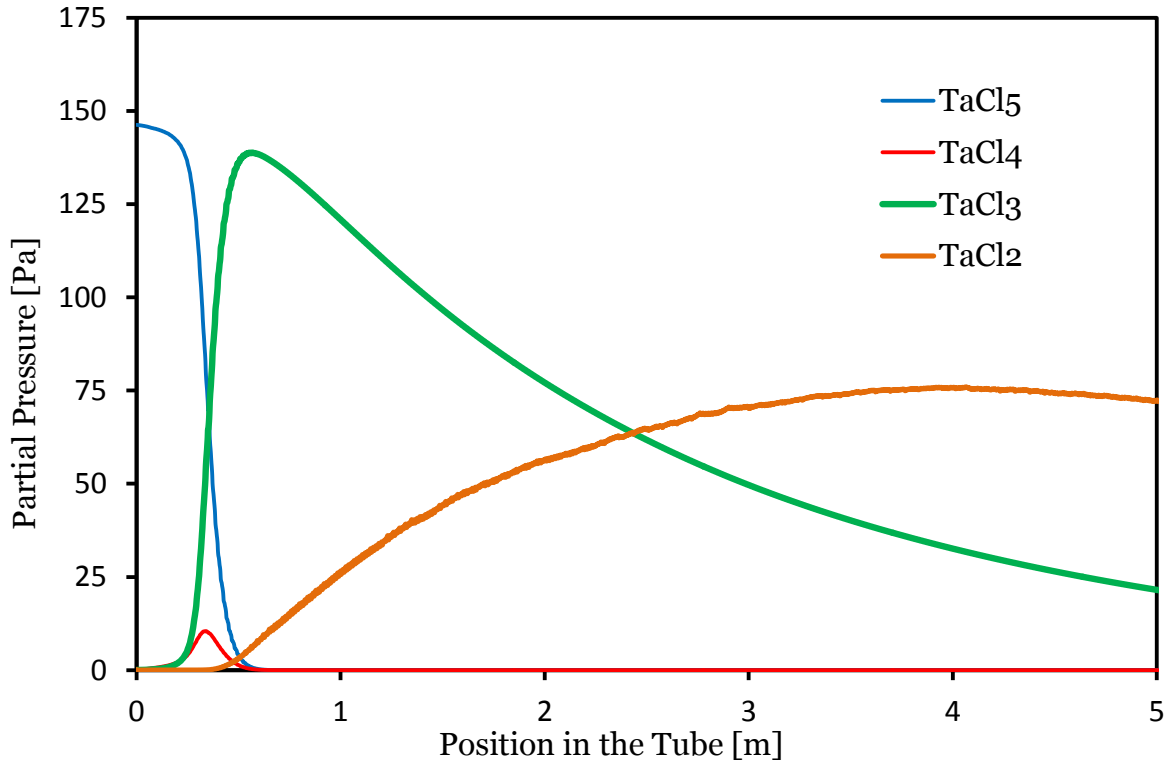

Figure 63: Simulated Partial Pressure profiles at: 800 °C & 76 mbar (450 L/h - H2, 5 L/h - Ar and 40 g/ h of Cl2

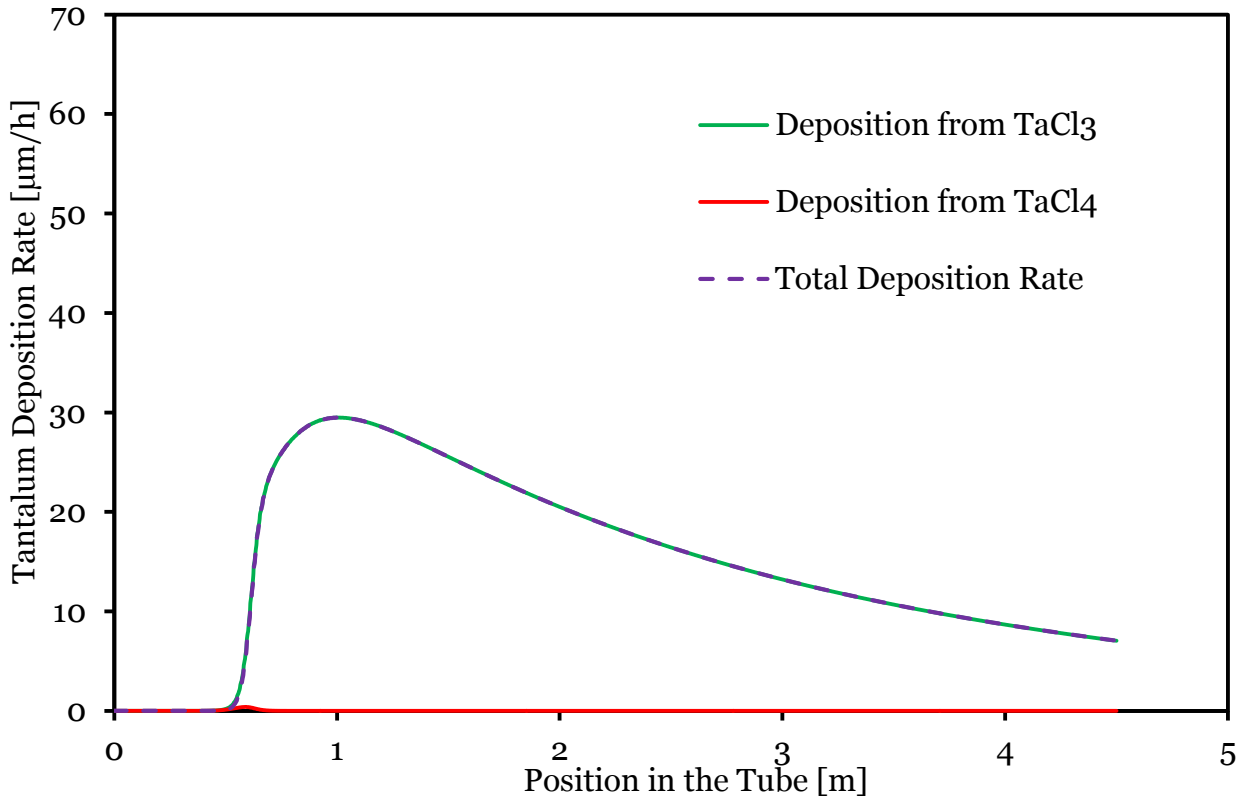

Figure 64: Distribution of the deposition rate at: 800 ^{O}C & 76 mbar (450 L/h - H2, 5 L/h - Ar and 40 g/ h of Cl2

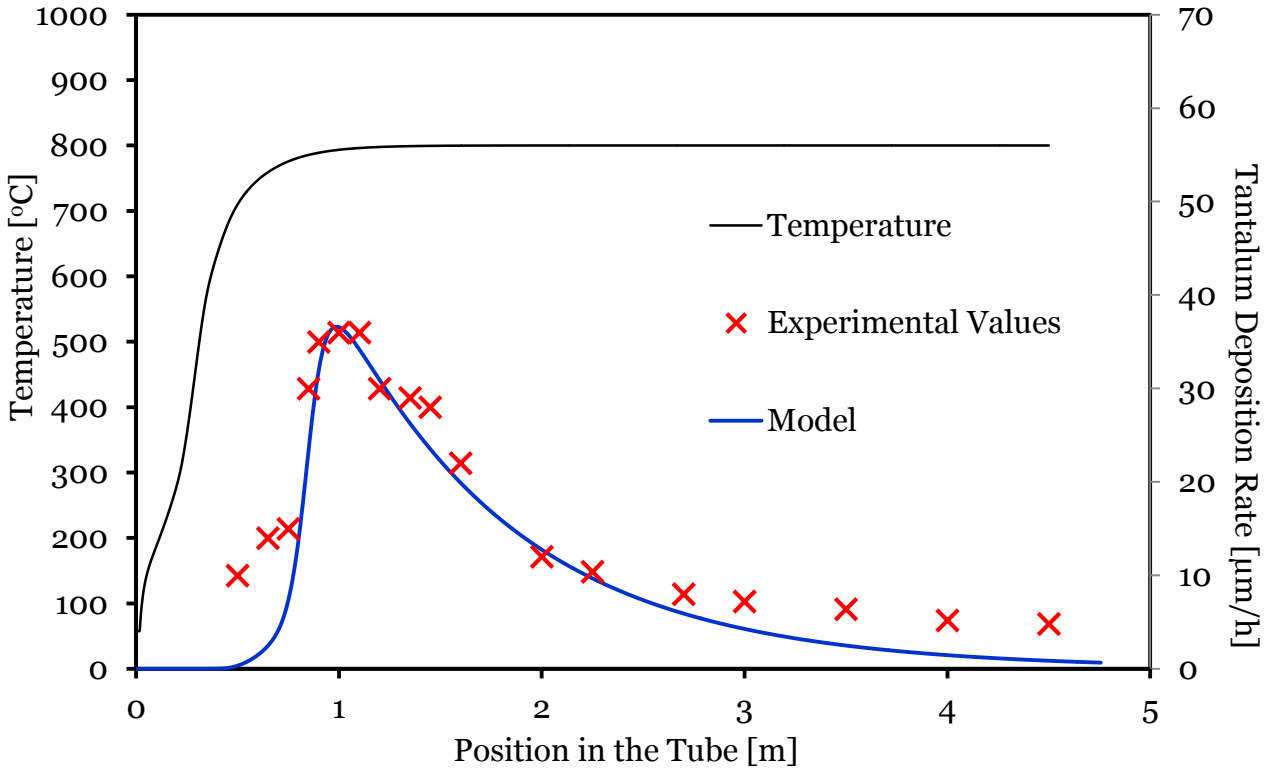

Figure 65: Model Fitting at: 800 °C & 100 mbar (150 L/h - H2, 5 L/h - Ar and 50 g/ h of Cl2

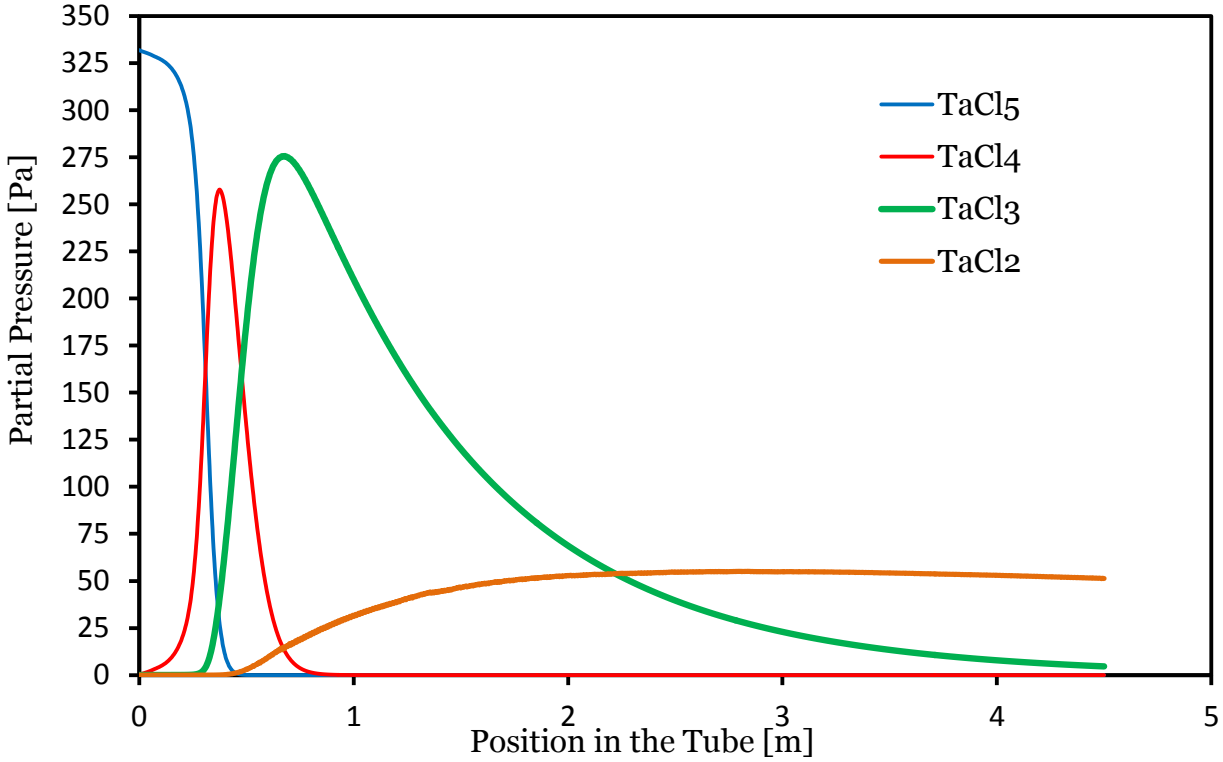

Figure 66: Simulated Partial Pressure profiles at: 800 °C & 100 mbar (150 L/h - H2, 5 L/h - Ar and 50 g/ h of Cl2

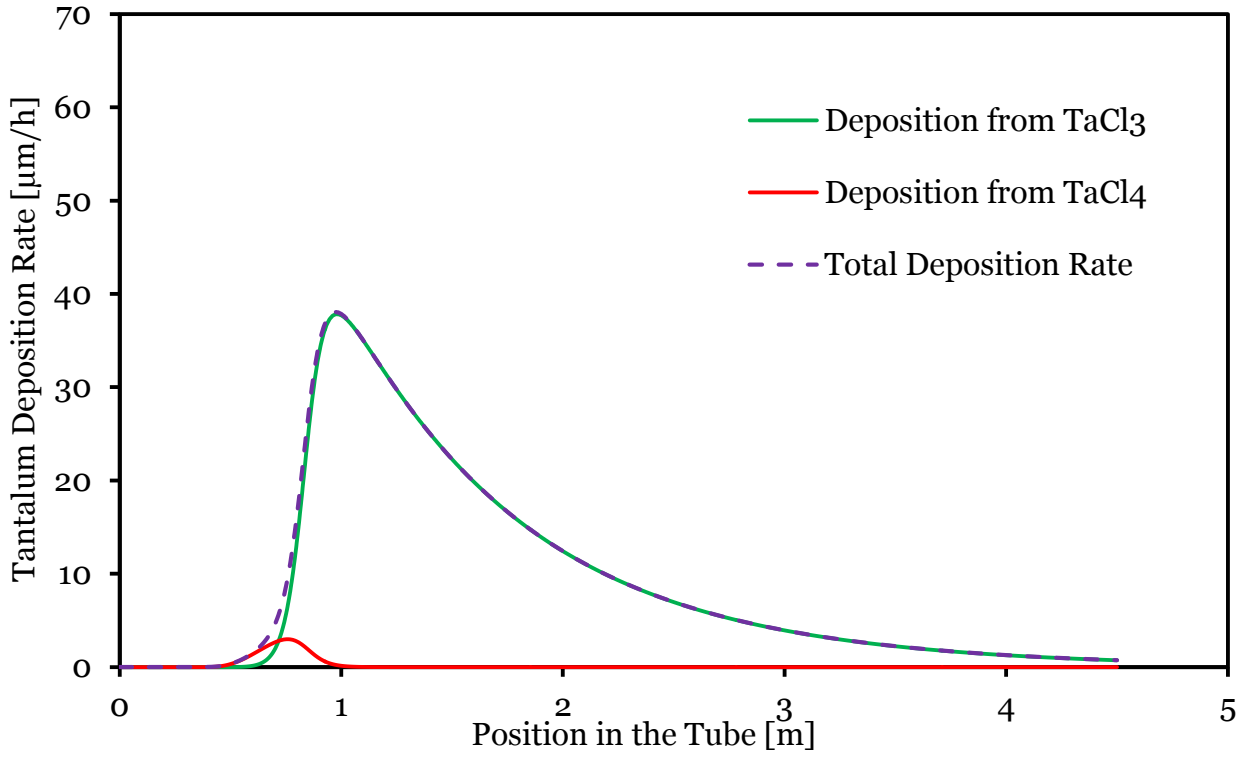

Figure 67: Distribution of the deposition rate at: 800 ^{0}C & 100 mbar (150 L/h - H2, 5 L/h - Ar and 50 g/ h of Cl2

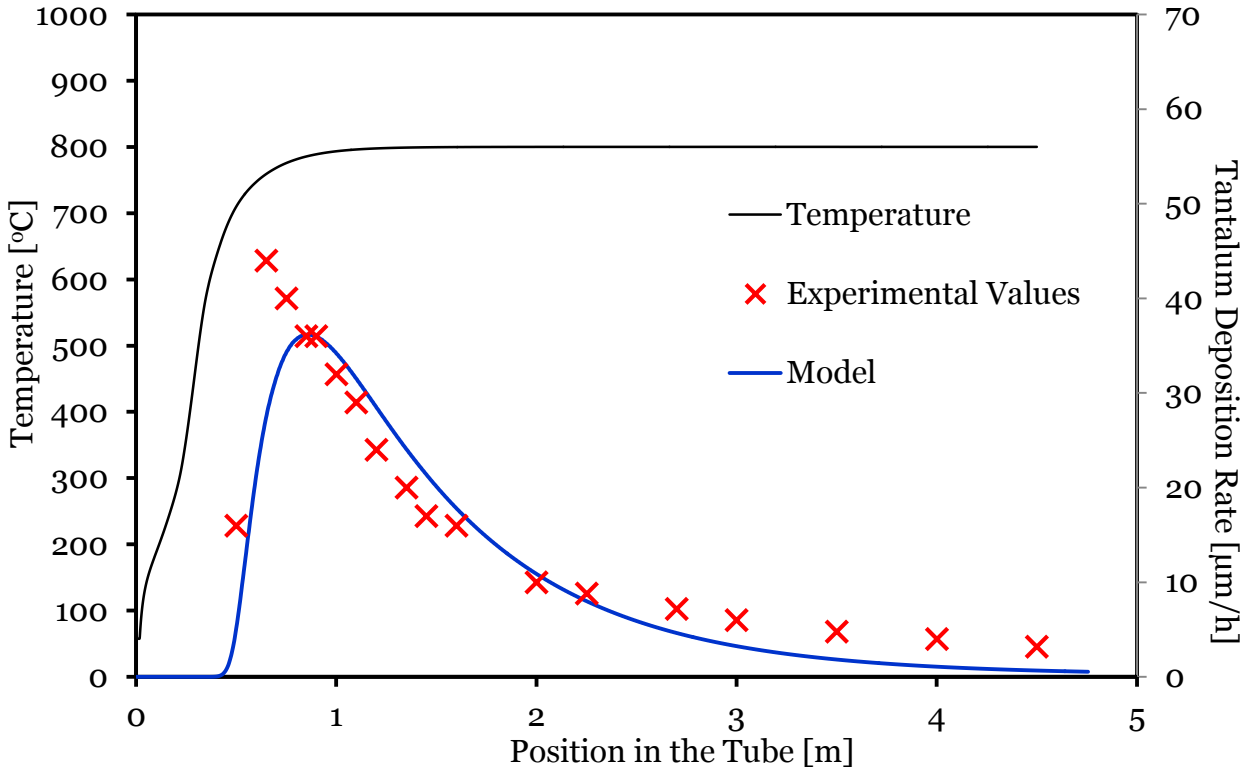

Figure 68: Model Fitting at: 800 °C & 300 mbar (300 L/h - H2, 80 L/h - Ar and 30 g/ h of Cl2

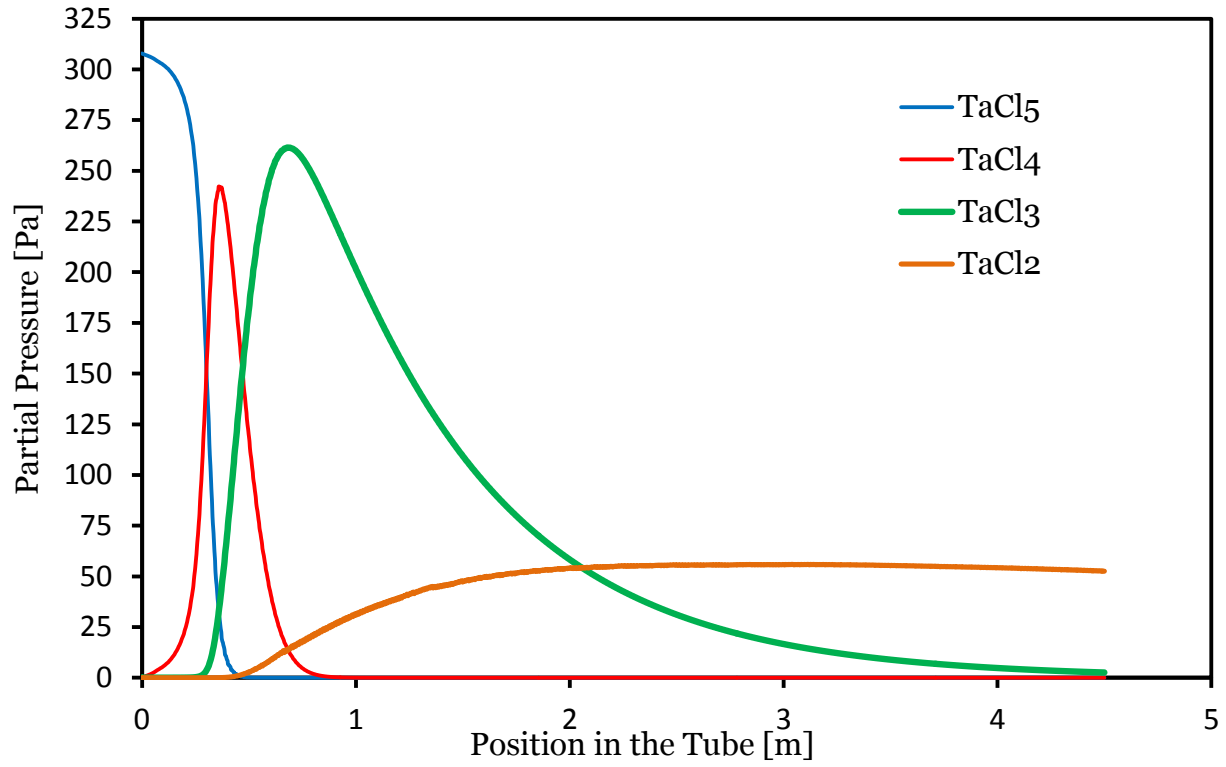

Figure 69: Simulated Partial Pressure profiles at: 800 °C & 300 mbar (300 L/h - H2, 80 L/h - Ar and 30 g/ h of Cl2

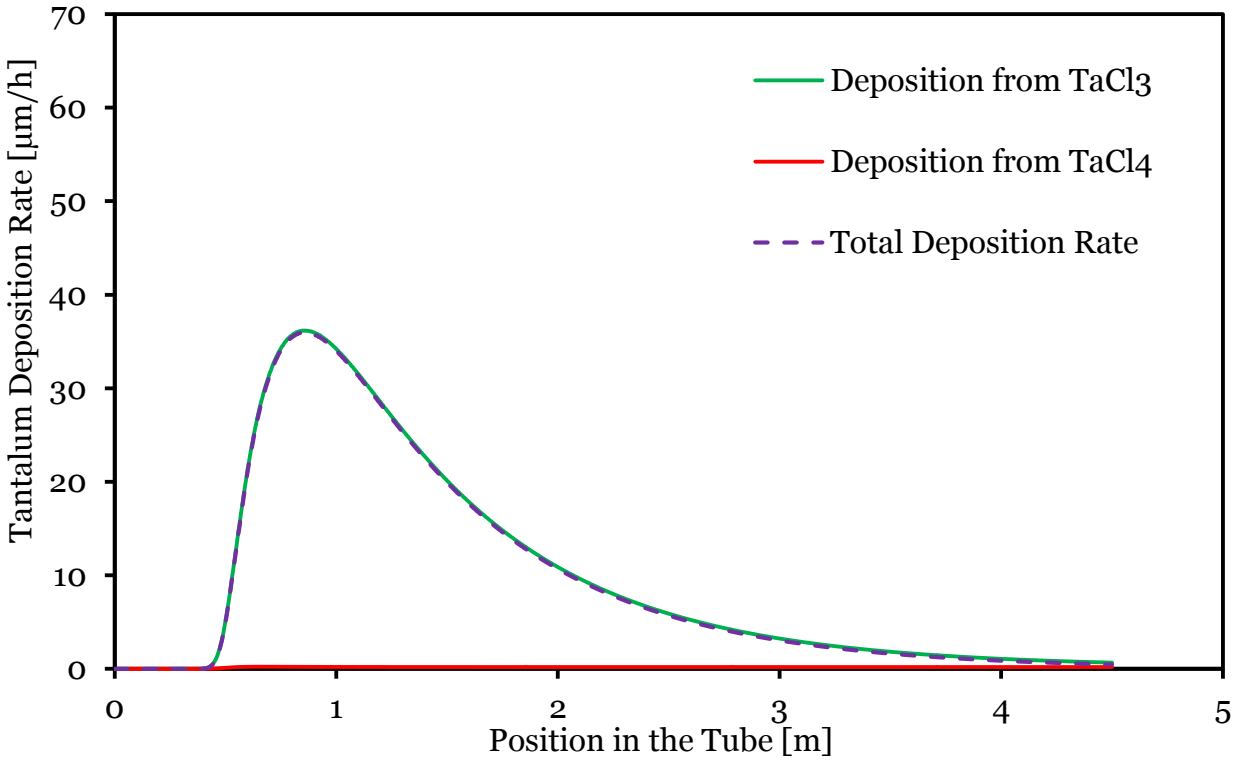

Figure 70: Distribution of the deposition rate at: 800 ^{o}C & 300 mbar (300 L/h - H2, 80 L/h - Ar and 30 g/ h of Cl2

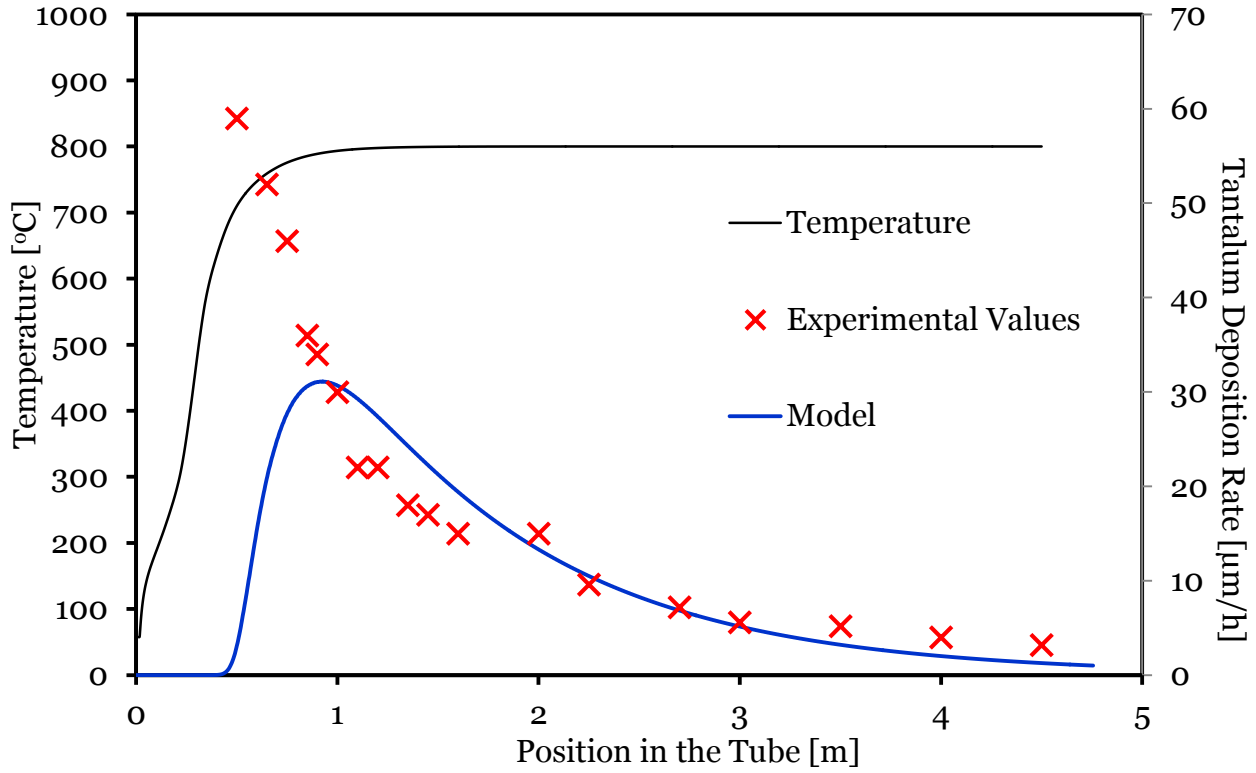

Figure 71: Model Fitting at: 800 °C & 990 mbar (300 L/h - H2, 80 L/h - Ar and 30 g/ h of Cl2

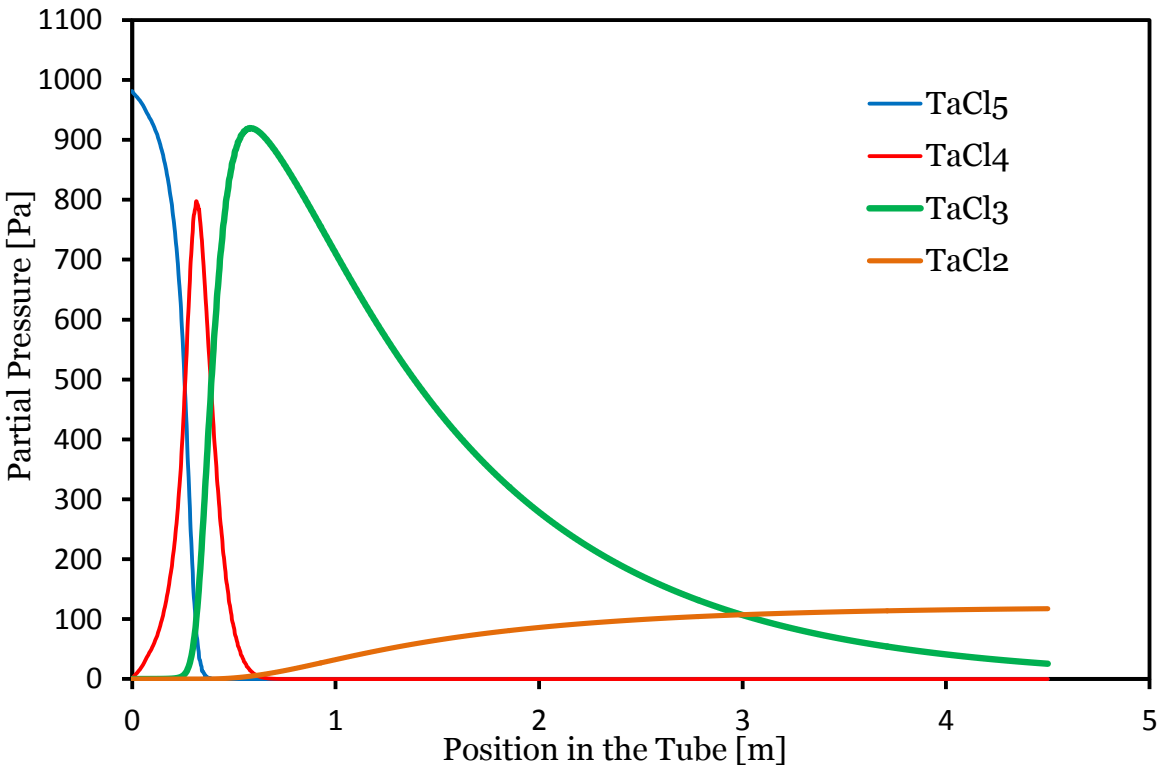

Figure 72: Simulated Partial Pressure profiles at: 800 °C & 990 mbar (300 L/h - H2, 80 L/h - Ar and 30 g/ h of Cl2

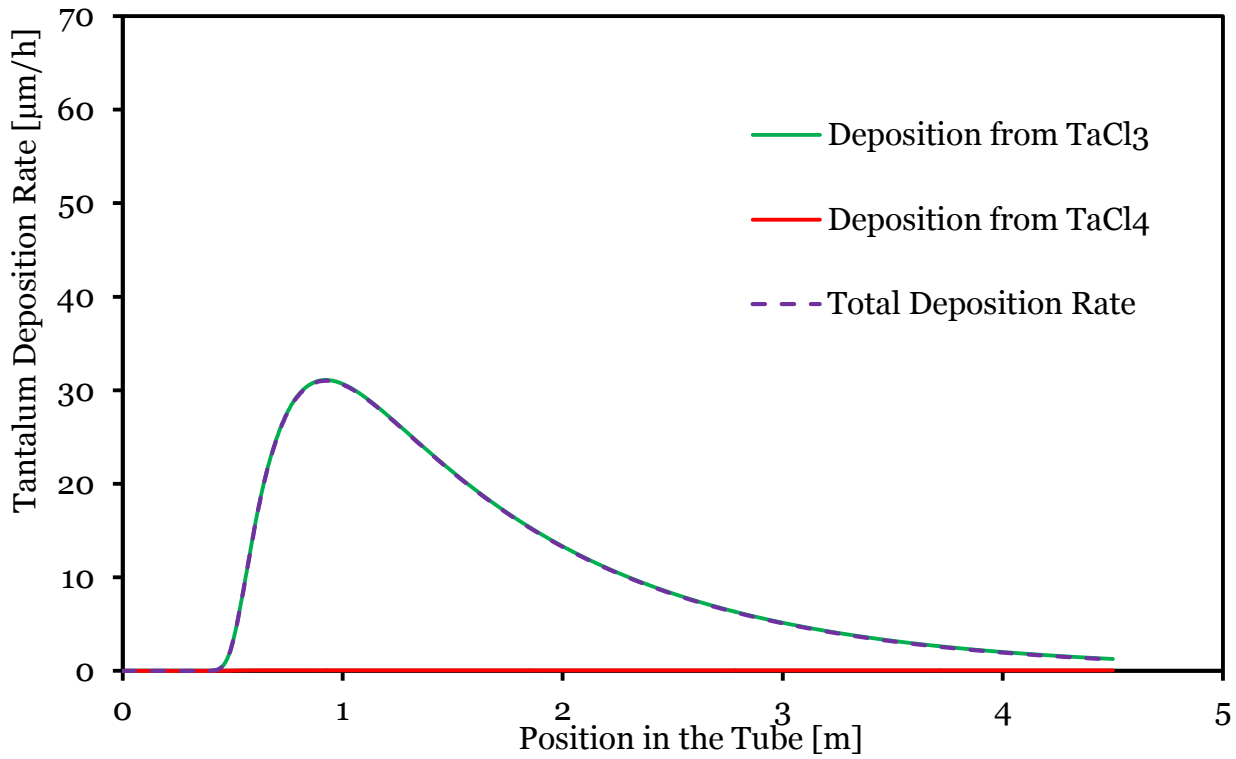

Figure 73: Distribution of the deposition rate at: 800 ^{O}C & 990 mbar (300 L/h - H2, 80 L/h - Ar and 30 g/ h of Cl2

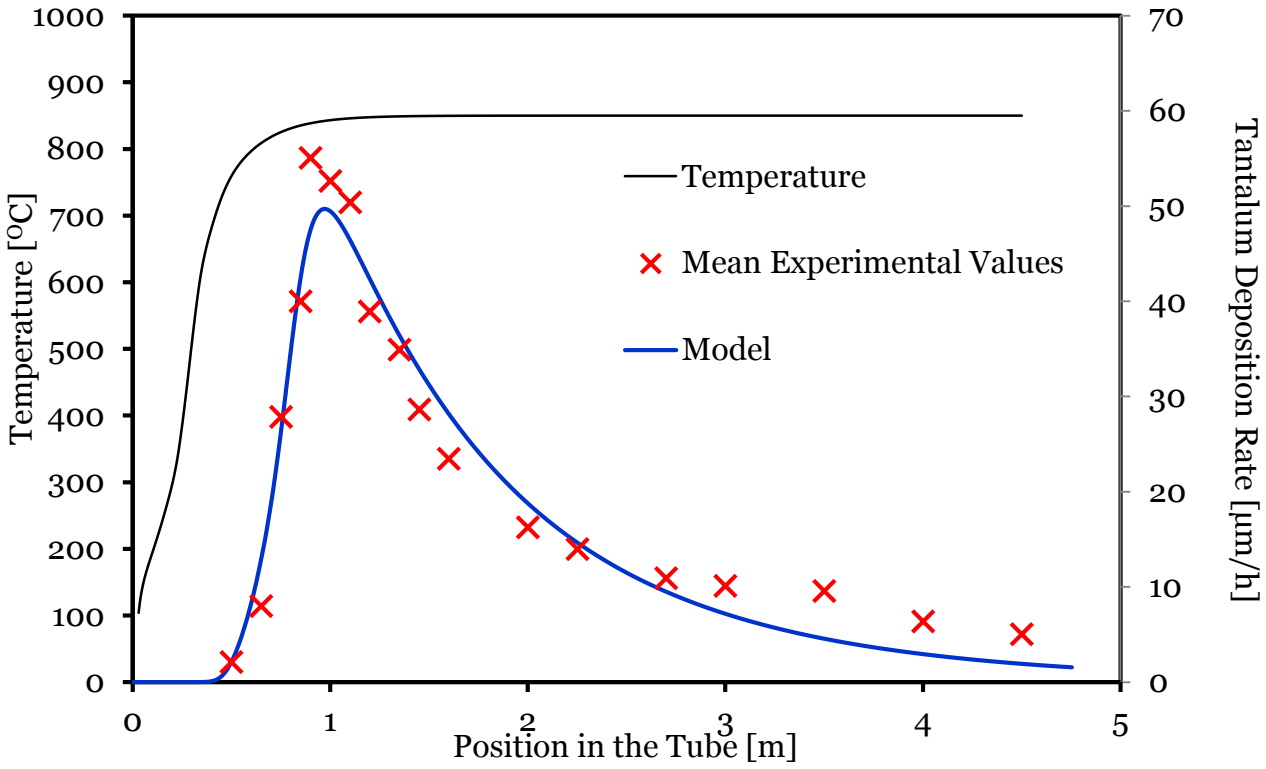

Figure 74: Model Fitting at: 850 °C & 25 mbar (150 L/h - H2, 5 L/h - Ar and 50 g/ h of Cl2

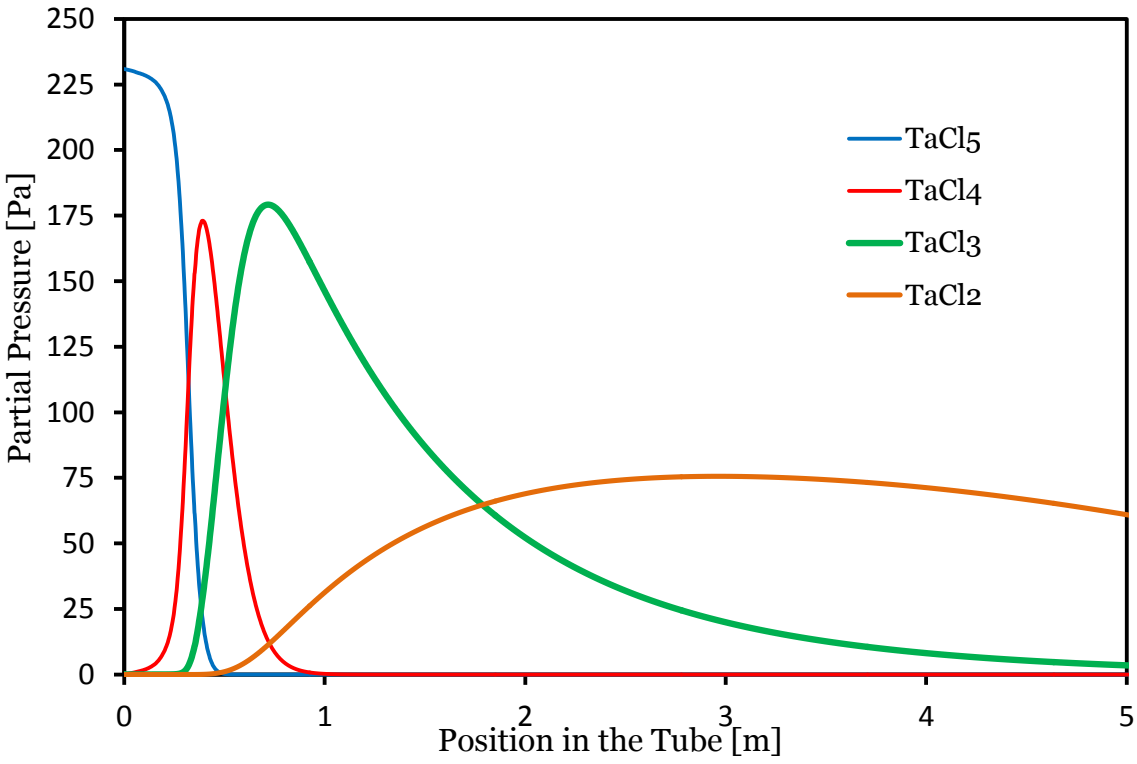

Figure 75: Simulated Partial Pressure profiles at: 850 °C & 25 mbar (150 L/h - H2, 5 L/h - Ar and 50 g/ h of Cl2

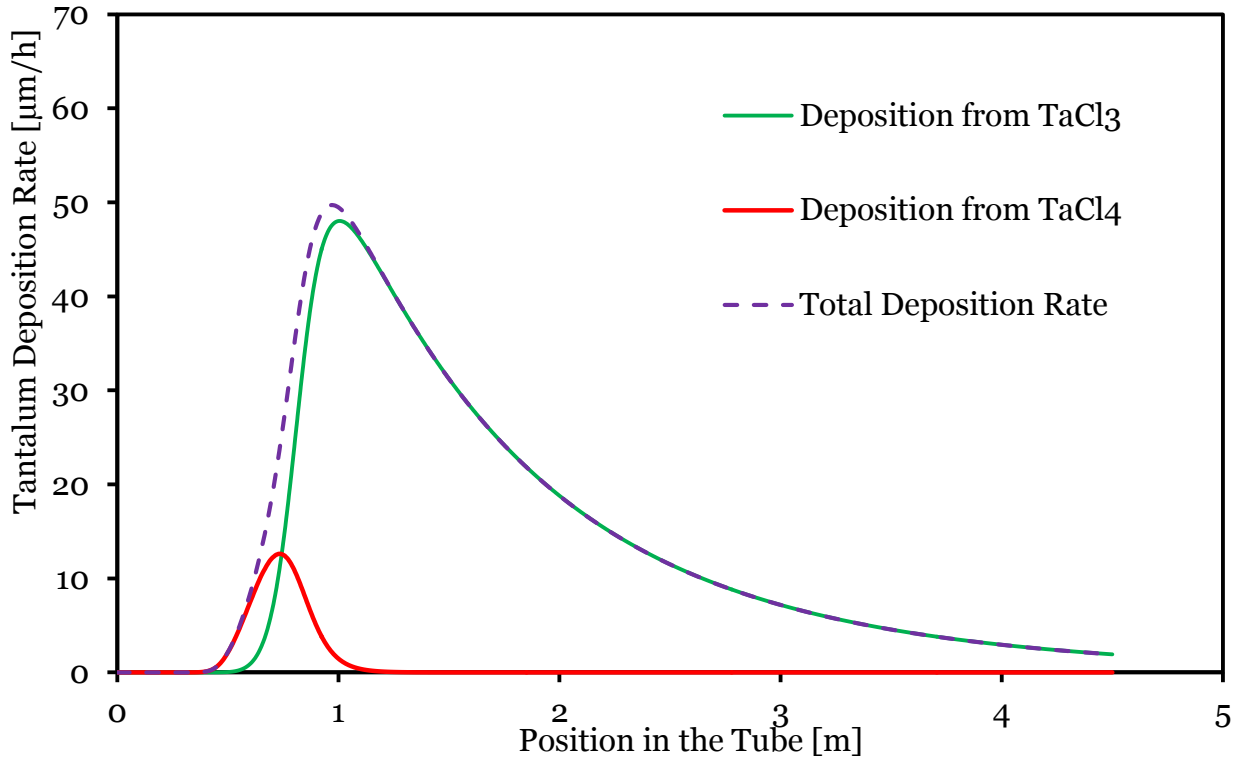

Figure 76: Distribution of the deposition rate at: 850 ^{O}C & 25 mbar (150 L/h - H2, 5 L/h - Ar and 50 g/ h of Cl2

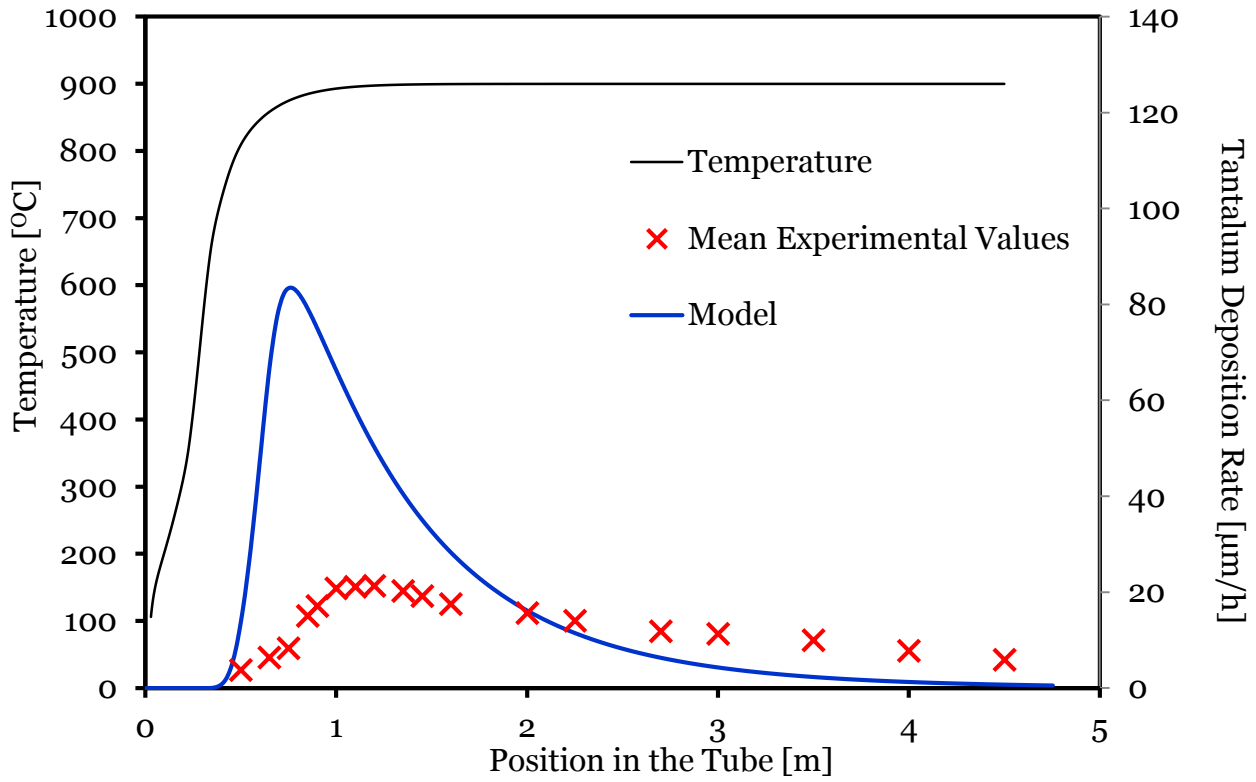

Figure 77: Model Fitting at: 900 °C & 25 mbar (150 L/h - H2, 5 L/h - Ar and 50 g/ h of Cl2

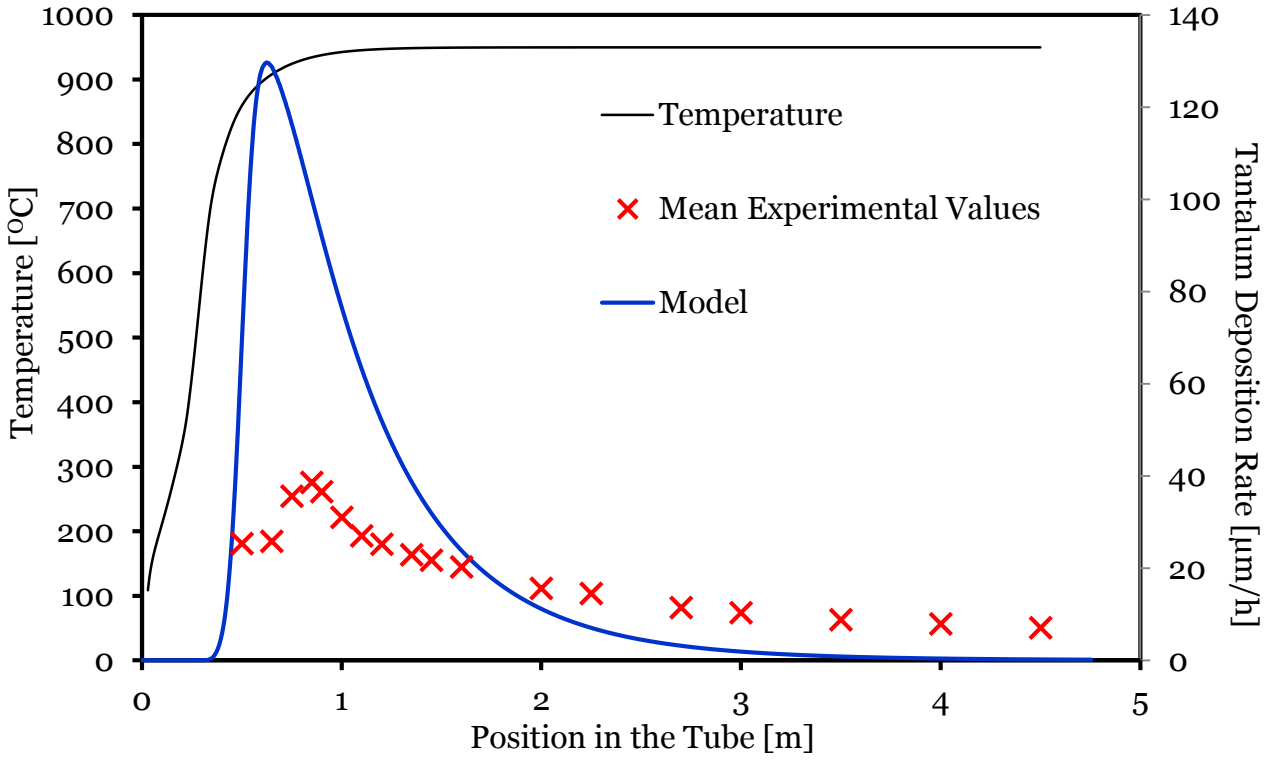

Figure 78: Model Fitting at: 950 °C & 25 mbar (150 L/h - H2, 5 L/h - Ar and 50 g/ h of Cl2

Table 12: Model Variables and their Optimal Values

Variable	Value	Description
A1 $\left[\frac{mol}{m^3 \cdot s \cdot Pa}\right]$	1588170	Pre-exponential Factor Reaction 1
A2 $\left[\frac{mol}{m^3 \cdot s \cdot Pa}\right]$	373127	Pre-exponential Factor Reaction 2
A3 $\left[\frac{mol}{m^3 \cdot s \cdot Pa}\right]$	188223	Pre-exponential Factor Reaction 3
A4 $\left[\frac{1}{s}\right]$	33190	Pre-exponential Factor Reaction 4
A5 $\left[\frac{1}{s}\right]$	310428	Pre-exponential Factor Reaction 5
EA1 $\left[\frac{J}{mol}\right]$	52574	Activation Energy Reaction 1
EA2 $\left[\frac{J}{mol}\right]$	60716	Activation Energy Reaction 2
EA3 $\left[\frac{J}{mol}\right]$	79858	Activation Energy Reaction 3
EA4 $\left[\frac{J}{mol}\right]$	304607	Activation Energy Reaction 4
EA5 $\left[\frac{J}{mol}\right]$	185163	Activation Energy Reaction 5
ΔH4 $\left[\frac{J}{mol}\right]$	-363760	Adsorption Enthalpy TaCl4
ΔH5 $\left[\frac{J}{mol}\right]$	-90530	Adsorption Enthalpy TaCl3
ΔS4 $\left[\frac{J}{mol \cdot K}\right]$	-337	Adsorption Entropy TaCl4
ΔS5 $\left[\frac{J}{mol \cdot K}\right]$	-241	Adsorption Entropy TaCl3
N_{Sites} $\left[mol/m^2\right]$	2962050	Number of Sites

The constants shown in table 12 are typical of the values expected in a CVD system. The pre-exponential values A1-A5 are within the range of 10^3 – 10^7 which is acceptable because reactions involving gases have been known to have pre-exponential factors anywhere from 10^{-5} - 10^{29} depending on the system. [53-55]

The activation energies found (EA1 –EA5) are in the range of 50 – 350 kJ/mol, which is also reasonable because this is a high temperature process, 700 – 950 ^{O}C, and does not happen at all below 600 ^{O}C. The values are also in the range seen in other CVD models. [54, 55]

Secondly, even at the high temperatures used for surface CVD (i.e. 700 – 950 ^{O}C) the complete reduction of tantalum chloride to tantalum still cannot happen in the gas phase, requiring a surface in order to occur. This shows that there is not enough energy to propagate the complete reaction in the gas phase; however, the surface acts as a heterogeneous catalyst upon which the complete reduction of tantalum chloride to tantalum can occur. The reactant species come into closer physical alignment once adsorbed onto a surface thus requiring less activation energy to react. It is for this reason that surface CVD can be modelled similarly to heterogeneous catalysis systems i.e. using Langmuir's adsorption – desorption kinetics. This all sums up to show that activation energies within this order of magnitude are to be expected in high temperature CVD systems. Other CVD systems (Silicon CVD) show very similar values. [54, 56]

Previous work on the CVD of tantalum, by *Eriksen* [29], suggests an overall activation energy of 103 kJ/mol for a direct reaction from $TaCl_{5(g)}$ to $Ta_{(S)}$ however, this is based on a very rudimentary technique and lacks a comprehensive kinetic study.

The adsorption enthalpies ($\Delta H4$ & $\Delta H5$) and entropies ($\Delta S4$ & $\Delta S5$) are in the range of 90 – 400 kJ/mol and 200 - 350 J/mol·K, respectively. These are also very similar to the values found in literature pertaining to other CVD systems. *Gardeniers et. al.* [57, 58] have done comprehensive studies on the adsorption of different silicon chlorides and hydrides onto silicon with respect to the CVD of silicon, and have found adsorption enthalpies and entropies quite close to those found in this work. This is further reinforced by *Giling's* work. [59]

6.4.5 General Discussion

The model developed in this project works well at 750 ^{O}C, 800 ^{O}C and 850 ^{O}C while it fails at 900 ^{O}C and 950 ^{O}C. It also fits well at all pressures, however less accurately at the tube inlets for the high-pressure experiments (990 mbar).

Looking at the SEM images in figures 44 and 45, and the graph in figure 38 (section 6.3.3) shows that the deposition rates and mechanism of deposition are very temperature dependent. Figure 38 shows that, at 25 mbar, the deposition rate increases when temperature is increased within the range of 750 – 850 ^{O}C, but falls when further increased to 900 ^{O}C. The deposition rates observed at 950 ^{O}C seem to be random (or very sensitive to a parameter which we have no control over, see figure 37). The SEM images also show stark differences in the characteristic of the tantalum surfaces deposited at different temperatures. The structure observed at 800 ^{O}C has a resemblance to that seen at 850 ^{O}C, but both are very different to what is seen at 900 and 950 ^{O}C.

All these observations lead to the inference that there is a change in the deposition mechanism somewhere between 850 – 900 ^{O}C. If this is truly the case then it is also reasonable that the model does not apply to the new mechanism of deposition and that is why it does not fit the 900 ^{O}C and 950 ^{O}C experiments.

Based on the kinetic study it was found that the deposition of tantalum happens only from $TaCl_4$ and $TaCl_3$, with $TaCl_3$ accounting for most and in some cases all of the deposition. Comparing the deposition rates with the partial pressure profiles shows that the tantalum deposition rate follows the partial pressure of $TaCl_3$. Comparing figure 56 with figure 57, or figure 59 with figure 60 shows that the earlier that the $TaCl_3$ partial pressure peaks the earlier that the deposition rate peaks also.

Looking at figure 40 reveals that the reactions where 450 L/h of hydrogen is used instead of 150 L/h have deposition peaks that appear significantly earlier in the tube than the counter part reactions. This is because all the reactions are under conditions of an excess hydrogen and tripling the hydrogen flow essentially just reduces the partial pressure of the other components. This reduction in the partial pressure of the $TaCl_3$ leads to its slower depletion by the gas phase reaction to form the inactive $TaCl_2$, but has no effect on the surface reaction that forms tantalum. It can thus be inferred that the peak position of the $TaCl_3$ partial pressure mostly depends on how slowly it is consumed by the gas phase reaction that turns it into $TaCl_2$.

It is for this reason also that the two experiments with 450 L/h of hydrogen (in figure 40) deposit more tantalum in the entire tube (higher yield) than their 150 L/h counterpart. This is emphasized when the 34 mbar experiment is compared to the 76 mbar one.

The reason that the reduction in partial pressure affects the gas phase depletion of $TaCl_3$ significantly and has no effect on the surface reaction is because the surface coverage in this region is high (fresh feed) and therefore close to one, which makes the deposition reaction zeroth-order with respect to precursor partial pressure, as explained in section 4.2.5.

The sudden fall in deposition rate with increasing the temperature from 850 – 900 ^{O}C (see figure 38) can also be explained by the gas phase depletion of $TaCl_3$ to form $TaCl_2$, which is inactive at the

surface. It is probable that above a certain temperature the gas phase *reaction 3* (reduction of $TaCl_3$ to form $TaCl_2$) suddenly becomes more vigorous and competitive in consuming the $TaCl_3$ before it deposits to the surface.

Another explanation for the peculiar behavior seen at 900 ^{O}C is that some of the $TaCl_5$ and $TaCl_4$ could be directly reduced to $TaCl_2$ without passing through the surface-active $TaCl_3$ phase.

Whichever of the two is the right explanation, it is definitely a fundamental change in the way the gas phase species are evolving and therefore not predictable by the kinetic model.

The implication of this is that when increasing the temperature in order to increase the deposition rate, care should be taken that the rate of the gas phase reduction of $TaCl_3$ is not increased as much thus leading to a waste of the precursor. If an increase in temperature were required to increase the overall deposition rate, then it should ideally be accompanied by a reduction of the precursor partial pressure by increasing the hydrogen flow.

It is likely that increasing the hydrogen flow rate would increase the deposition rates seen at 900^{O}C by lowering precursor waste but this has not yet been tested.

Deposition at 950 ^{O}C is generally not recommended because of the large diffusion layer that is formed between the substrate and the tantalum. Figure 43 in section 6.3.2 shows that this diffusion layer is about 2µm thick, which makes it brittle and therefore a liability to mechanical strength. Cutting through the tubes with a saw peeled off the tantalum in some areas for the 950 ^{O}C experiments.

Figure 39 shows that the higher the system pressure the more steep the deposition rate profile is along the tube; meaning high deposition rates at the inlet and very low deposition at the tube outlet. This generally means that lower system pressures are better suited for CVD of tantalum in long narrow channels due to a higher throwing ability (more uniform layers with a farther reach).

The deposition rates at 750 ^{O}C are relatively low and the profile is mostly flat in comparison to the other temperatures. This is useful in depositing uniform layers of tantalum over large surface areas. The lack of a pronounced peak in the deposition rate and the slow formation of $TaCl_2$ (figure 53 and figure 54) mean that the conditions at the temperature offer a great 'throwing ability', which is necessary for uniformly coating long narrow channels.

6.5 Heat Exchanger Results

The heat exchanger was coated by project partner Tantaline® A/S (Denmark) while it was cut and characterised by Alfa Laval®, Lund – Sweden. The author did the 3-D model of the heat exchanger at the Technical University of Denmark.

The coating process was run at 825 ^{O}C and 25 mbar. The feed rates were 300 L/h of Hydrogen, 61 grams/h of Chlorine and 4.8 L/h of Argon.

The exact geometry of the heat exchanger's flow channels was obtained from Alfa Laval® and used to implement the model.

Slight adjustments were made in the model inputs to try to account for the fact that the tantalum coating system at Tantaline A/S includes a pre-heater and that the system pressure is measured further away from the reactor exit than in the author's equipment. These adjustments were that, in the model a system pressure of 27 mbar (at the heat exchanger exit) was used in order to allow a 2 mbar pressure drop for the extra length of the system. In addition, the entire precursor feed was allowed to enter the heat exchanger as TaCl3 chloride instead of TaCl5 to account for the transformation in the pre-heater.

It is worth noting that such a heat exchanger consists of several channels on each working side (nine process channels and ten utility channels) and all channels are considered identical (see Figure 80). The model therefore only calculates for one flow channel (level) to minimize the required computing resources.

Also worth noting is that, apart from the four portals in the corners of the heat exchangers, what appear to be holes in the flow channels are actually contact points between plates. They appear as holes in the model because there is no flow in the contact points, as they are welding points.

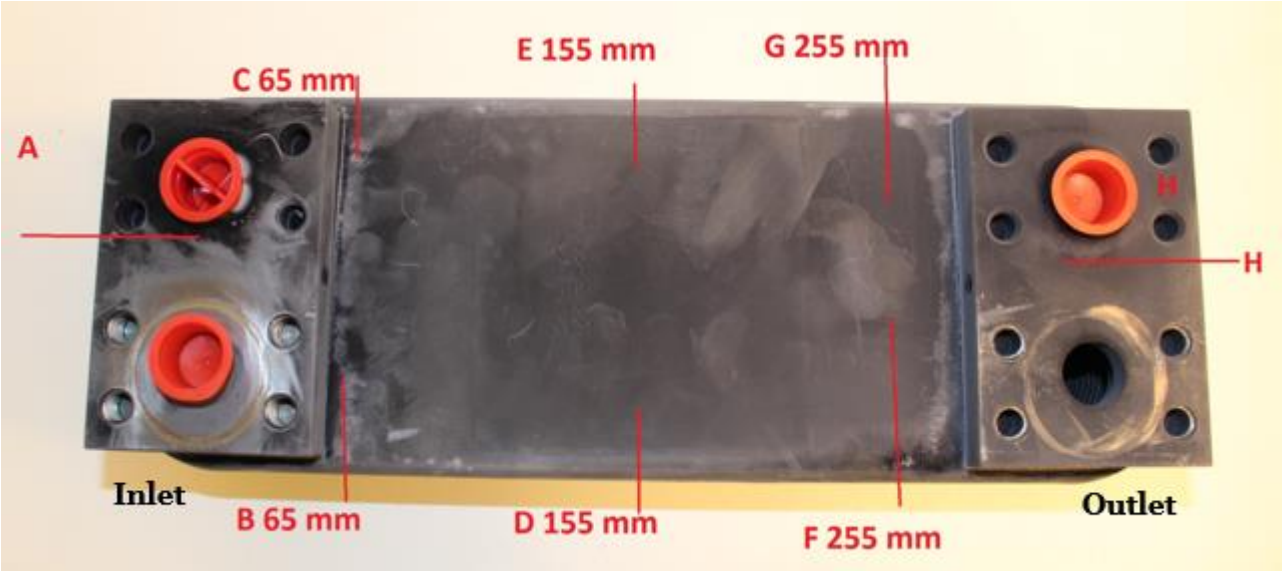

Figure 79: Labeled Picture of the coated Plate Heat exchanger

6.5.1 Visualisation of how plate heat exchangers work

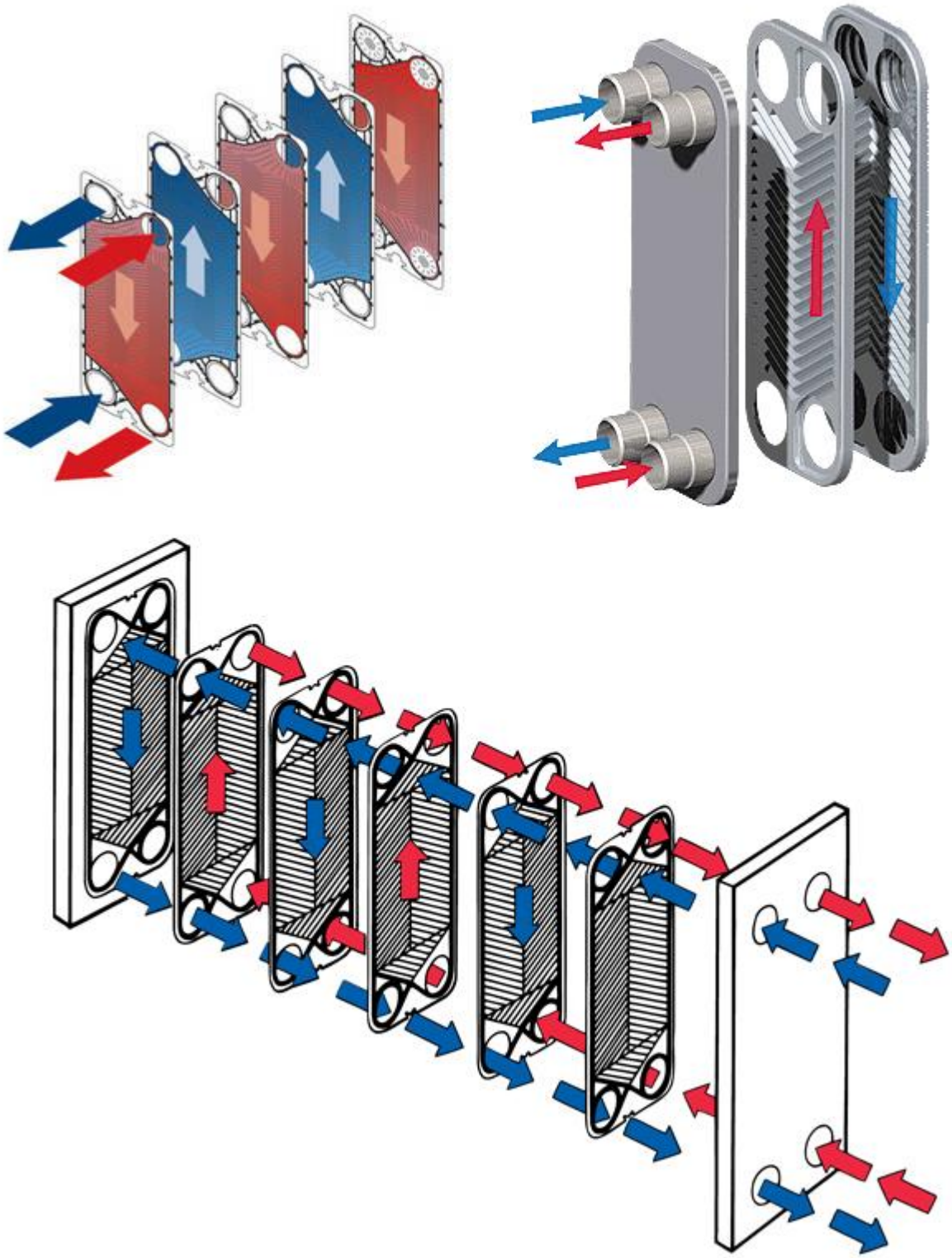

Figure 80: Illustration of the arrangement of flow channels in a plate heat exchanger [60-62]

6.5.2 Pressure Drop in the Heat exchanger

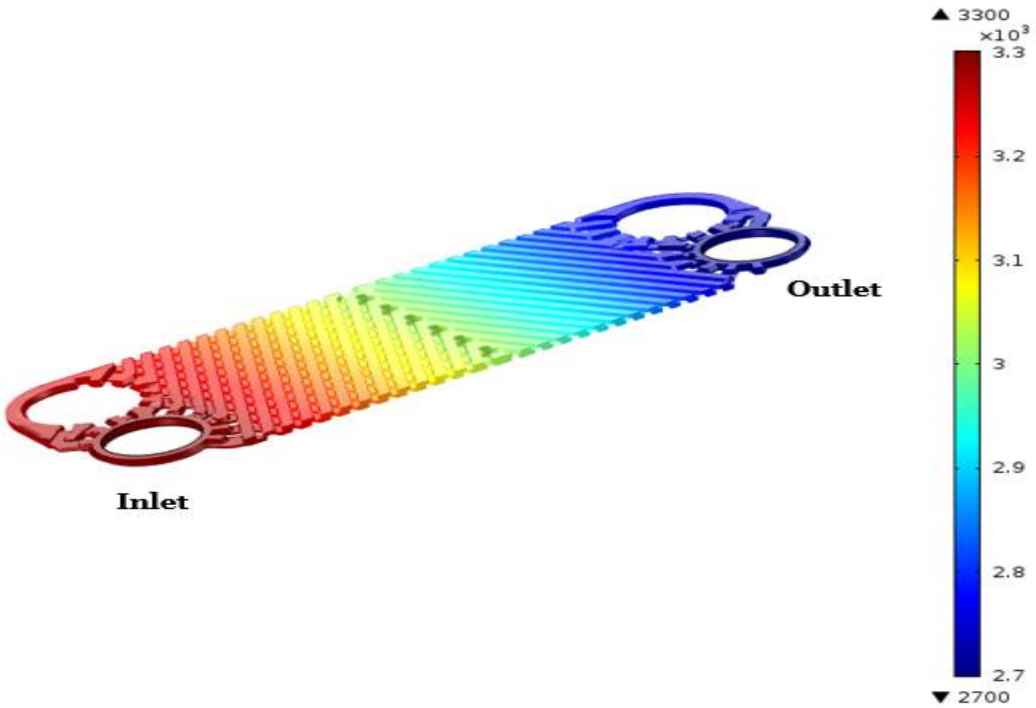

Figure 81: 3-D Surface plot showing the Pressure drop across the Heat Exchanger flow channel. The scale is from 3.3 x 10^3 Pa (33 mbar) to 2.7 x 10^3 Pa (27 mbar).

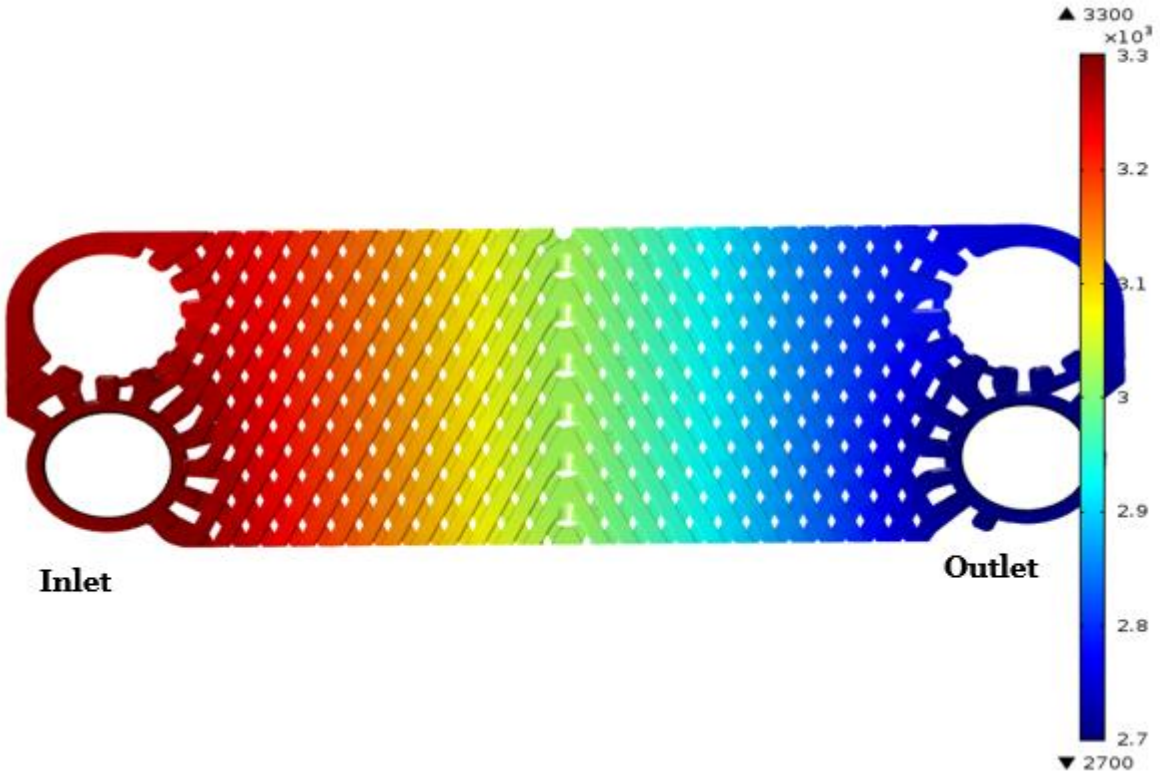

Figure 82: 2-D Surface plot showing the Pressure drop across the Heat Exchanger flow channel. The scale is from 3.3 x 10^3 Pa (33 mbar) to 2.7 x 10^3 Pa (27 mbar).

6.5.3 Flow in the Heat exchanger

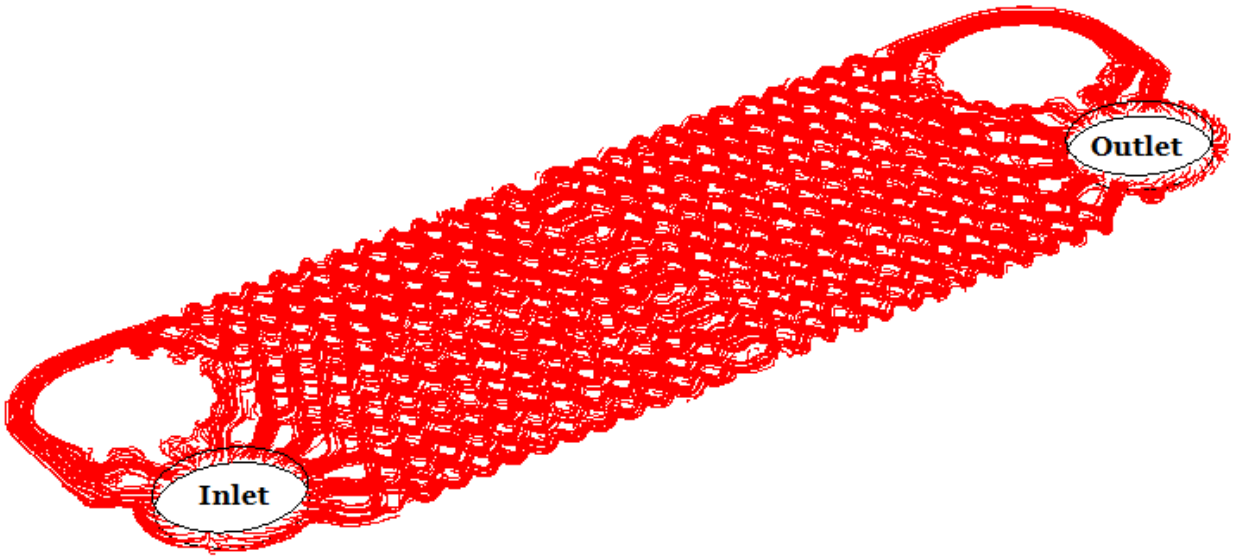

Figure 83: 3-D Streamline plot showing the flow patterns along the Heat Exchanger flow channel

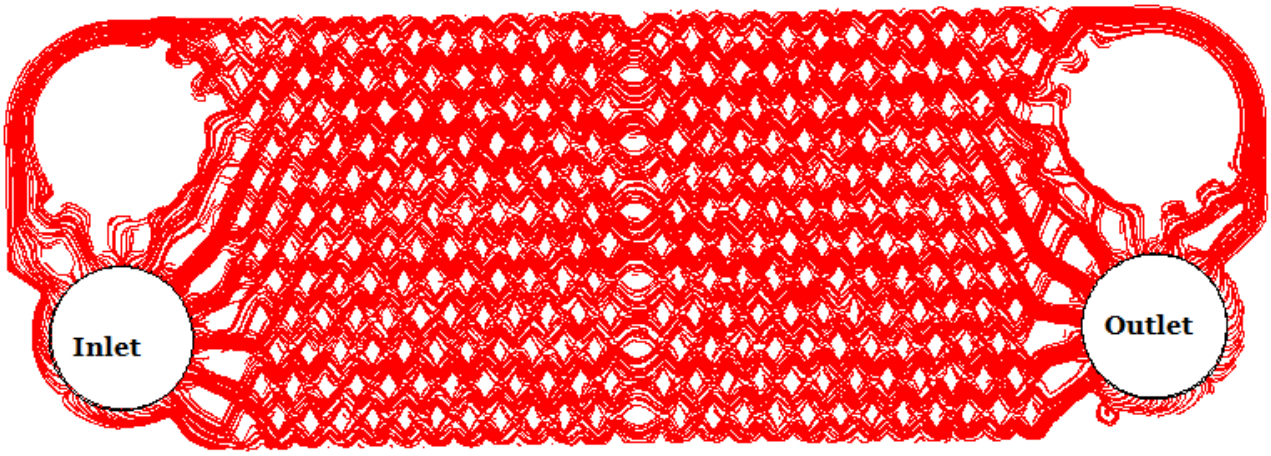

Figure 84: 2-D Streamline plot showing the flow patterns along the Heat Exchanger flow channel

6.5.4 Deposition Profile

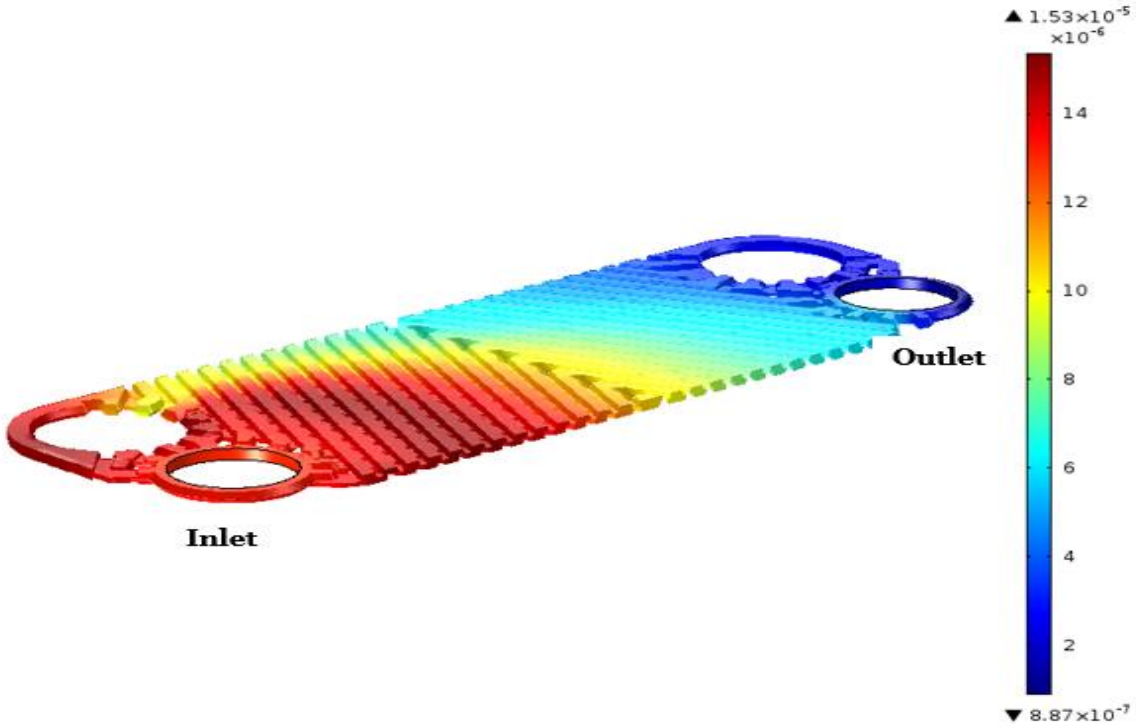

Figure 85: 3-D Surface plot showing the simulated tantalum deposition rates in the Heat Exchanger flow channel. The scale is from 15.3 µm/h to 0.887 µm/h.

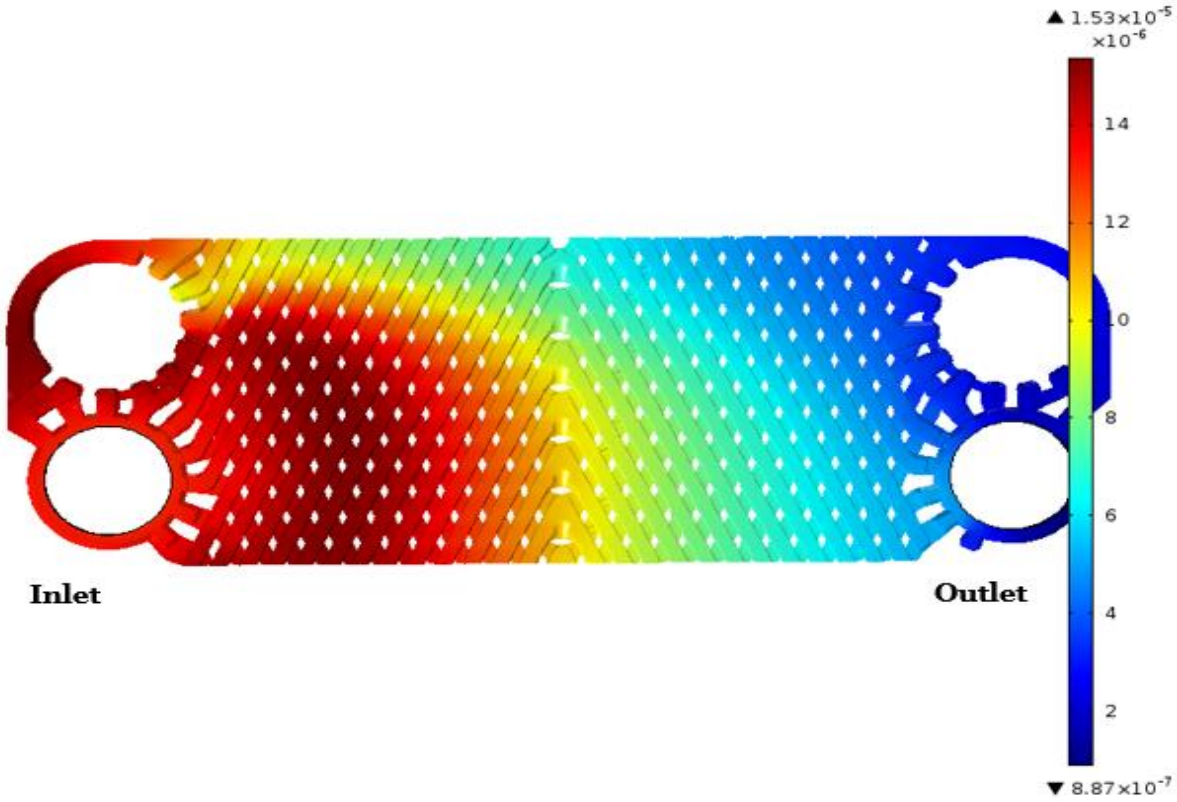

Figure 86: 2-D Surface plot showing the simulated tantalum deposition rates in the Heat Exchanger flow channel. The scale is from 15.3 µm/h to 0.887 µm/h.

Table 13: Deposition Rate at Various points in the Heat Exchanger (Positions labeled in figure 79)

Position	Deposition rate Sample 1 [µm/h]	Deposition rate Sample 2 [µm/h]	Experimental data Average [µm/h]	*Model Prediction [µm/h]*
A	11	12.9	**11.95**	***14.34***
B	17.6	16.5	**17.05**	***14.45***
C	6.25	5.51	**5.88**	***10***
D	4.78	4.78	**4.78**	***10***
E	3.68	4	**3.84**	***6.73***
F	3.68	2.57	**3.125**	***5.35***
G	3.31	3.31	**3.31**	***3.97***
H	2.39	2.57	**2.48**	***2.21***

6.5.5 Comments

The simulation results for the heat exchanger experiment are shown in figures 80- 85, and are compared to the experimental data in table 13.

Comparing the experimental data to the simulation shows both strong and weak points of agreement. Having already shown that the model works well at these experimental conditions (Pressure of 25 mbar and 800 – 850 ^{0}C), it is thought that the discrepancies between the model and the experiment are mainly due to the fact that the preheater has not been modelled along. This being a 3-D model would require extensive computing resources which are currently not available to the author. The assumption that all the TaCl5 would have turned into TaCl3 by the heat exchanger's inlet while none of it is lost to deposition in the preheater cannot be entirely accurate but is the best guess to go by. It is however good that the discrepancies are small, which shows that they could be eliminated or minimised if the preheater is modelled and the experiment is run in a more controlled environment (using an experimental machine instead of a production machine).

7 CONCLUSION

The aim of this project was to study the CVD of tantalum in long narrow channels and to implement a model that can be used to optimize the process; this has been done with a great degree of success. A kinetic model has been developed and shown to work within the temperature range of 750 – 850 ^{O}C and at all pressures. It was also found that the deposition rates are very dependent on the substrate temperature with almost no deposition at 700 ^{O}C and stochastic deposition at 950 ^{O}C. The deposition rates were found to increase with temperature within the 750 – 850 ^{O}C temperature range, but suddenly fall at 900 ^{O}C and show random results at 950^{O}C. This peculiar behaviour is explained based on observations made in the kinetic model, with respect to the abundance of $TaCl_3$ in the reaction system, while suggesting two mechanisms through which the situation could arise.

The effects of system pressure on the deposition rate was also studied and it was found that increasing system pressures leads to higher deposition rates although this effect diminishes as atmospheric pressure is approached. The increase in deposition rates due to increase in system pressure is explained by the fact that increasing system pressure also increases the partial pressure of the precursor and its residence time in the tube; both lead to higher deposition rates and extent of reaction/ yield. This effect of system pressure was observed in the range of 25 – 300 mbar; increasing the pressure above 300 mbar showed no significant effects.

Experiments in which the reactant partial pressures and residence times are varied showed that the effects of system pressure on the deposition rate cannot entirely be explained by the change in residence times or the increase in surface reaction rate due to increased precursor partial pressure. It was found, through model fitting, that the rate at which $TaCl_3$ is formed and consumed by the gas phase reactions plays a significant role in the overall deposition.

The kinetic model has been used to suggest that $TaCl_3$ is the most dominant contributor of tantalum to the surface and that its prevelence in the system has a significant effect on the deposition rate profile along the tube. $TaCl_4$ was also shown to directly contribute, though insignificantly, to the formation of tantalum on the surface. Both $TaCl_5$ and $TaCl_2$ were shown not to be surface active; with the formation of $TaCl_2$ actually having an inhibitory effect to the overall deposition yield.

The fact that the experiment run at 34 mbar has a higher overall deposition rate than the one run at 76 mbar, or that the deposition rate falls when increasing temperature from 850 ^{O}C to 900 ^{O}C, is linked to the gas phase consumption of $TaCl_3$ in a manner analogous to competitive inhibition.

These observations highlight the role performed by $TaCl_3$ in tantalum CVD and show that any optimisation procedure needs to take this into account. Especially, care must be taken when efforts are made to increase the deposition rate, either by increasing reaction temperature of reactant partial pressure, that the gas phase comsumption of $TaCl_3$ is not increased as well. This would lead to lower

depostion rates and poorer yields. Generally, increasing reactant partial pressures leads to higher deposition peaks (poorer distribution) and is not recommended for CVD in long narrow channels. When temperature is increased in order to increase yield and deposition rate, care should be taken by increasing the hydrogen flow in order to further dilute the gas mixture and prevent precursor waste through the formation of $TaCl_2$.

SEM cross section images have shown that the deposited tantalum is relatively smooth at 800 and 900 ^{O}C when compared to 850 and 950 ^{O}C, with the surface at 950 ^{O}C being the roughest. The same cross sections also show that there is an intermetallic diffusion (alloy) zone at the tantalum-steel interface. The diffusion zone was found to be much thicker and more brittle at 950 ^{O}C than at the lower temperatures. For this reason, deposition at 950 ^{O}C is not recommended.

SEM images of the tantalum surface showed that both temperature and pressure have an effect on the morphology of the tantalum surface. The effects of temperature are most significant with the 800 ^{O}C surface consisting of closely spaced whiskers, that at 850 ^{O}C looking flaky, 900 ^{O}C being flat and rugged, and 950 ^{O}C consisting of dendrites that are orders of magnitude larger than the whiskers seen at 800^{O}C. The effect of pressure on the surface morphology seemed less pronounced at the microscopic level and is explained by the flow patterns expected at these pressures.

The SEM images and deposition-rate profile graphs play a significant role in showing that there is a fundamental change in the system behaviour between 850 - 900 ^{O}C that leads to a decrease in deposition rate with increase in temperature, a peculiar tendency not well described by the model.

One heat exchanger coating experiment was done in collaboration with the project's industrial partners and a corresponding model simulation was implemented. There were both points of accurate and inaccurate prediction by the model.

The values given for the constants in table 12 represent a unique solution for the implemented mechanism. No other solutions were found that could fit the experimental data. A sensitivity and uncertainty analysis of the model is recommended as future work in this area in order to shed more light on how the model, and the CVD system in general, behave. A rudimentary analysis on how small perturbations in the chlorine flow affect the overall deposition rate at 800 ^{O}C and 25 mbar is shown in figure 88, Appendix C.

8 REFERENCES

1. Bermúdez, M.-D., F.J. Carrión, G. Martínez-Nicolás, and R. López, *Erosion–corrosion of stainless steels, titanium, tantalum and zirconium.* Wear, 2005. **258**(1–4): p. 693-700.
2. Robin, A. and J.L. Rosa, *Corrosion behavior of niobium, tantalum and their alloys in hot hydrochloric and phosphoric acid solutions.* International Journal of Refractory Metals and Hard Materials, 2000. **18**(1): p. 13-21.
3. Kouřil, M., E. Christensen, S. Eriksen, and B. Gillesberg, *Corrosion rate of construction materials in hot phosphoric acid with the contribution of anodic polarization.* Materials and Corrosion, 2012. **63**(4): p. 310-316.
4. Kuznetsov, S.A., *15 - Electrochemical Synthesis of Novel Niobium and Tantalum Compounds in Molten Salts*, in *Molten Salts Chemistry*, F. Lantelme and H. Groult, Editors. 2013, Elsevier: Oxford. p. 311-329.
5. Cardarelli, F., P. Taxil, and A. Savall, *Tantalum protective thin coating techniques for the Chemical Process Industry: Molten salts electrocoating as a new alternative.* International Journal of Refractory Metals and Hard Materials, 1996. **14**(5–6): p. 365-381.
6. Spitz, J. and J. Chevallier. *Comparative study of tantalum deposition by chemical vapor deposition and electron beam vacuum evaporation.* in *International Conference on Chemical Vapour Deposition (CVD-5)*. 1975. Stoke Poges, United Kingdom: Department de Metallurgie de Grenoble.
7. Suh, Y., W. Chen, S. Maeng, S. Gu, R.A. Levy, and H. Thridandam, *Synthesis and characterization of plasma assisted chemically vapor deposited tantalum.* Thin Solid Films, 2010. **518**(19): p. 5452-5456.
8. Levy, R.A., *Investigation of Chemically Vapor Deposited Tantalum for Medium Caliber Gun Barrel Protection*, 2008, New Jersey Institute of Technology: New Jersey.
9. Kodas, T.T. and M.J. Hampden-Smith, *The Chemistry of Metal CVD*. 1994, Weinheim - New York - Basel - Cambridge - Tokyo VCH.
10. Cardonne, S.M., P. Kumar, C.A. Michaluk, and H.D. Schwartz, *Tantalum and its alloys.* International Journal of Refractory Metals and Hard Materials, 1995. **13**(4): p. 187-194.
11. Nikiforov, A.V., I.M. Petrushina, E. Christensen, A.L. Tomás-García, and N.J. Bjerrum, *Corrosion behaviour of construction materials for high temperature steam electrolysers.* International Journal of Hydrogen Energy, 2011. **36**(1): p. 111-119.
12. Moore, R.E. and M.S. Austin, *Use of Porous Tantalum Cones in Revision Total Knee Arthroplasty.* Operative Techniques in Orthopaedics, 2012. **22**(4): p. 209-221.
13. Li, X., L. Wang, X. Yu, Y. Feng, C. Wang, K. Yang, and D. Su, *Tantalum coating on porous Ti6Al4V scaffold using chemical vapor deposition and preliminary biological evaluation.* Materials Science and Engineering: C, 2013. **33**(5): p. 2987-2994.
14. Eriksen, S., B. Gillesberg, L.N. Langmaack, and E. Christensen. *Tantalum Coated Carbon-Carbon Composite Material for Surgical Implants*. in *Materials and Processes for Medical Devices Conference*. 2004. St. Paul Minnesota: ASM International.
15. Martin, R.F. and P.-A. Wülser, *Niobium and tantalum in minerals: Siderophile, chalcophile or lithophile, and polyvalent.* Journal of Geochemical Exploration, (0).
16. Gladczuk, L., A. Patel, C. Singh Paur, and M. Sosnowski, *Tantalum films for protective coatings of steel.* Thin Solid Films, 2004. **467**(1–2): p. 150-157.
17. Jiang, A., T.A. Tyson, L. Axe, L. Gladczuk, M. Sosnowski, and P. Cote, *The structure and stability of β-Ta thin films.* Thin Solid Films, 2005. **479**(1–2): p. 166-173.
18. Pierson, H.O., *Handbook of Chemical Vapor Deposition (CVD)*. Second ed. 1999, New Jersey: Noyes Publications.
19. Jiang, A., A. Yohannan, N.O. Nnolim, T.A. Tyson, L. Axe, S.L. Lee, and P. Cote, *Investigation of the structure of β-tantalum.* Thin Solid Films, 2003. **437**(1–2): p. 116-122.
20. Patnaik, P., ed. *Handbook of Inorganic Chemicals*. 2003, McGraw-Hill Companies: New York.
21. Manchester, F.D., ed. *Phase Diagrams of Binary Hydrogen Alloys*. Monograph Series on Alloy Phase Diagrams. 2000, ASM International.

22. Mueller, W.M., J.P. Blackledge, and G.G. Libowitz, eds. *Metal Hydrides*. 1968, Academic Press: New York, London.
23. Robin, A., *Corrosion behavior of niobium, tantalum and their alloys in boiling sulfuric acid solutions.* International Journal of Refractory Metals and Hard Materials, 1997. **15**(5–6): p. 317-323.
24. Xu, Y. and X.-T. Yan, *Chemical Vapour Deposition: An Integrated Engineering Design for Advanced Materials*. Engineering Materials and Processes. 2010, London: Springer.
25. Trkula, M., *Vapor Deposition of Tantalum and Tantalum Compounds*, in *125th Proceedings Meeting of TMS (Tantalum Symposium)*1996, Los Alamos National Laboratory.
26. Carlsson, J.-O. and P.M. Martin, *Chapter 7 - Chemical Vapor Deposition*, in *Handbook of Deposition Technologies for Films and Coatings (Third Edition)*, P.M. Martin, Editor. 2010, William Andrew Publishing: Boston. p. 314-363.
27. Mugabi, J.A., *Optimization of the Chemical Vapour Deposition of Tantalum* in *Department of Chemistry*2011, Technical University of Denmark: Lyngby, Denmark. p. 116.
28. Bird, R.B., W.E. Stewart, and E.N. Lightfoot, *Transport Phenomena*. 2nd Revised Edition ed. 2006, New York: John Wiley and Sons Inc.
29. Eriksen, S., *Chemical Vapour Deposition of Tantalum and experiments on niobium, tungsten and platinum CVD.*, in *Department of Chemistry*1999, Technical University of Denmark: Lyngby Denmark. p. 187.
30. Powell, C.F., *Chemically Deposited Metals*, in *Vapor Deposition*, J.H. Oxley and J.M. Blocher, Editors. 1966, John Wiley & Sons, INC.: New York, London, Sydney.
31. Powell, C.F., I.E. Campbell, and B.W. Gonser, *The deposition of tantalum and columbium from their volatilized halides.* Tantalum and Colombium, 1948. **95**(6): p. 258-265.
32. Stolz, M., K. Hieber, and C. Wieczorek, *Universal chemical vapour deposition system for metallurgical coatings.* Thin Solid Films, 1983. **100**(3): p. 209-218.
33. Ugolini, D., S.P. Kowalczyk, and F.R. McFeely, *Photoelectron spectroscopy studies of chemical vapor deposition of Ta from a TaF5 precursor on Si and SiO2 substrates.* Journal of Applied Physics, 1991. **70**(7): p. 3899-3906.
34. Kaloyeros, A.E., X. Chen, S. Lane, H.L. Frisch, and B. Arkles, *Tantalum diffusion barrier grown by inorganic plasma-promoted chemical vapor deposition: Performance in copper metallization.* Journal of Materials Research, 2000. **15**(12): p. 2800-2810.
35. Chen, X., H.L. Frisch, A.E. Kaloyeros, and B. Arkles, *Low temperature plasma-promoted chemical vapor deposition of tantalum from tantalum pentabromide for copper metallization.* Journal of Vacuum Science & Technology B: Microelectronics and Nanometer Structures, 1998. **16**(5): p. 2887-2890.
36. Macionczyk, F., B. Gerold, and R. Thull, *Repassivating tantalum/tantalum oxide surface modification on stainless steel implants.* Surface and Coatings Technology, 2001. **142–144**(0): p. 1084-1087.
37. Park, K.Y., H.J. Kim, and Y.J. Suh, *Preparation of tantalum nanopowders through hydrogen reduction of TaCl5 vapor.* Powder Technology, 2007. **172**(3): p. 144-148.
38. Shroff, A.M., *Chemical vapor deposition of tungsten, tantalum, and molybdenum by the chloride reduction process.* High Temperatures - High Pressures, 1974. **6**: p. 415-421.
39. Perry, A.J., C. Beguin, and H.E. Hintermann, *Tantalum coating of mild steel at atmospheric pressure.* Thin Solid Films, 1980. **66**(2): p. 197-210.
40. COMSOL-MULTIPHYSICS, *COMSOL Documentation*, 2011.
41. Poling, B.E., J.M. Prausnitz, and J.P. O'Connell, *The Properties of Gases and Liquids*. 5 ed. 2001, New York: McGraw-Hill.
42. Hirschfelder, J.O., C.F. Curtiss, and R.B. Bird, *Molecular Theory of Gases and Liquids*. 1954, New York: Wiley.
43. Mason, E.A. and S.C. Saxena, *Physics of Fluids*. 1 ed. 1958.
44. White, F.M., *Fluid Mechanics*. 4th ed. 1998, Boston: McGraw-Hill.
45. Chapman, S. and T.G. Cowling, *The Mathematical Theory of Non-uniform Gases*. 1952, New York: Cambridge University Press.
46. Cussler, E.L., *Diffusion; Mass Transfer in Fluid Systems*. 3rd ed. 2009, Cambrigde: Cambridge University Press.

47. Van Heijningen, R.J.J., J.P. Harpe, and J.J.M. Beenakker, *Determination of the diffusion coefficients of binary mixtures of the noble gases as a function of temperature and concentration.* Physica, 1968. **38**(1): p. 1-34.
48. Papari, M.M., D. Mohammad-aghaiee, B. Haghighi, and A. Boushehri, *Transport properties of argon–hydrogen gaseous mixture from an effective unlike interaction.* Fluid Phase Equilibria, 2005. **232**(1–2): p. 122-135.
49. Shashkov, A.G., A.F. Zolotukhina, L.P. Fokin, and A.N. Kalashnikov, *Transfer properties of mixtures of rarefied neutral gases. Hydrogen–argon system.* Journal of Engineering Physics and Thermophysics, 2010. **83**(1): p. 188-208.
50. Yaws, C.L., *Chapter 6 - Thermal Conductivity of Gas – Inorganic Compounds*, in *Transport Properties of Chemicals and Hydrocarbons*, C.L. Yaws, Editor. 2009, William Andrew Publishing: Boston. p. 292-298.
51. Barin, I.P.G., *Thermochemical data of pure substances*. 1995, Weinheim; New York: VCH.
52. Atkins, P.W., *Physical Chemistry*. 1998: Freeman.
53. Liu, S.-S. and W.-D. Xiao, *Numerical simulations of particle growth in a silicon-CVD fluidized bed reactor via a CFD–PBM coupled model.* Chemical Engineering Science, 2014. **111**(0): p. 112-125.
54. Ni, H., S. Lu, and C. Chen, *Modeling and simulation of silicon epitaxial growth in Siemens CVD reactor.* Journal of Crystal Growth, 2014. **404**(0): p. 89-99.
55. Cheng, W.T., H.C. Li, and C.N. Huang, *Simulation and optimization of silicon thermal CVD through CFD integrating Taguchi method.* Chemical Engineering Journal, 2008. **137**(3): p. 603-613.
56. Castillo, J.L. and D.E. Rosner, *Role of high activation energy homogeneous chemical reactions in affecting CVD-rates and deposit quality for heated surfaces.* Chemical Engineering Science, 1996. **51**(24): p. 5325-5340.
57. Gardeniers, J.G.E., L.J. Giling, F. de Jong, and J.P. Van der Eerden, *A theoretical study of adsorption equilibria in silicon CVD.* Journal of Crystal Growth, 1990. **104**(3): p. 727-743.
58. Gardeniers, J.G.E. and L.J. Giling, *Vapour growth of silicon: growth anisotropy and adsorption.* Journal of Crystal Growth, 1991. **115**(1–4): p. 542-550.
59. Giling, L.J., H.H.C. De Moor, W.P.J.H. Jacobs, and A.A. Saaman, *Adsorption on Si(111) during CVD of silicon from silane: The effect of temperature, bond strength, supersaturation and pressure.* Journal of Crystal Growth, 1986. **78**(2): p. 303-321.
60. Genemco. Available from: http://www.genemco.com/aloe/plate.html.
61. Radion. Available from: http://www.radion.co.il/index.php?id=749.
62. Danfoss. Available from: http://www.technoserviceco.com/gasket.htm.

APPENDIX A

Tantalum deposition rate profiles with a Preheater installed

(Referred to in section 6.1)

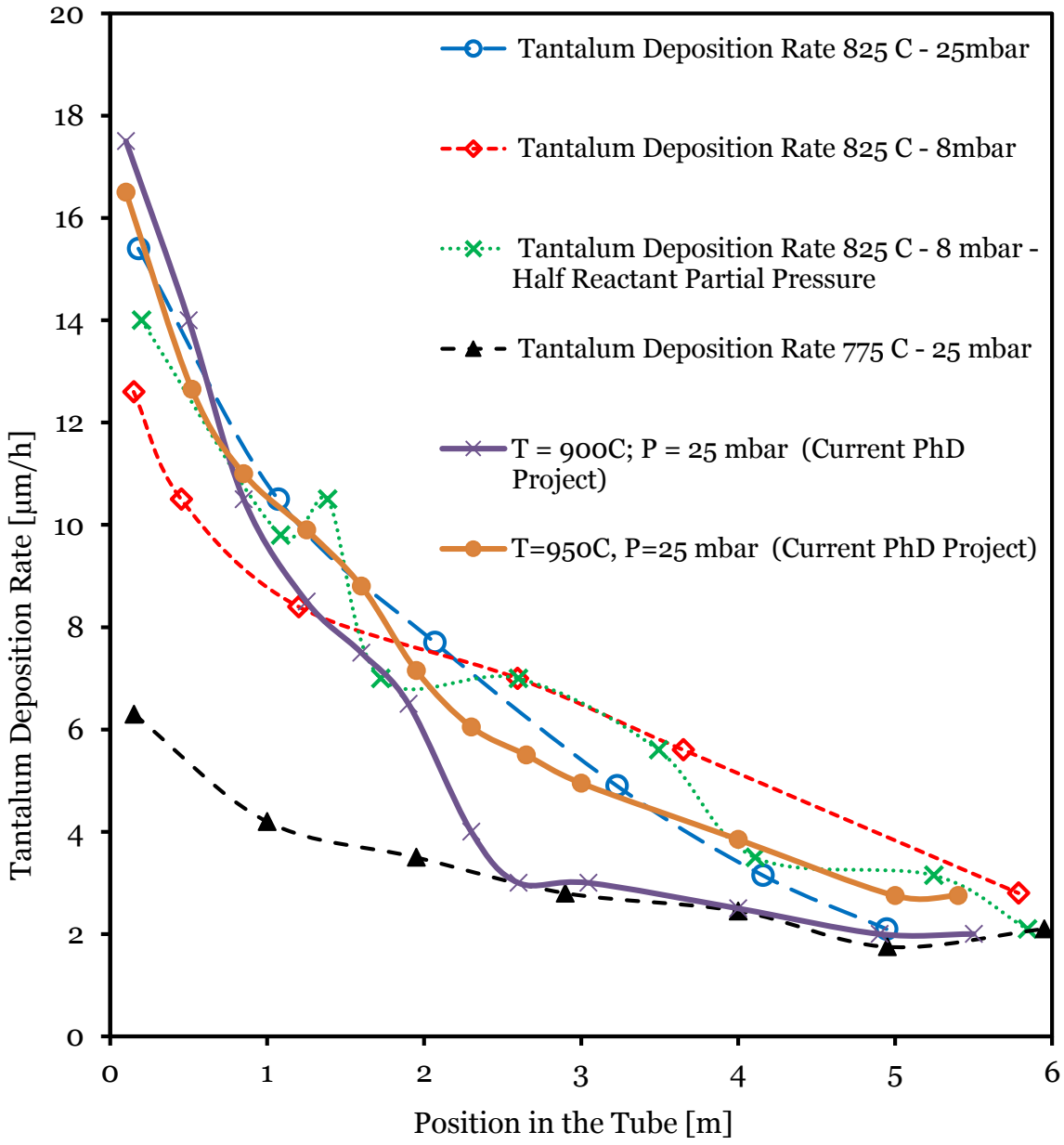

Figure 87: Tantalum deposition rate profiles along the tube length for all experiments with a preheater installed.

APPENDIX B

SEM Images of the Tantalum-Steel interface. (Referred to in section 6.3.2)

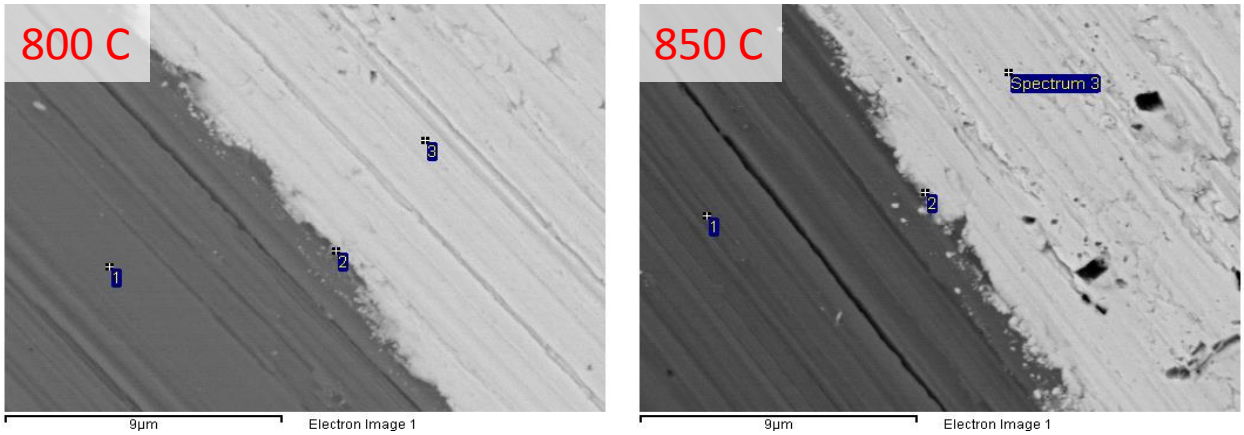

Figure 1: SEM images showing the alloy interface between the tantalum and steel (800 & 850 ^{O}C)

Table 14: Energy Dispersive X-ray spectroscopy for the spectra at 800 ^{O}C. Results in weight %

Spectrum	C	O	Cr	Mn	Fe	Ni	Mo	Ta	Total
Spectrum 1	2.16		17.01	1.64	63.16	13.18	2.85		100.00
Spectrum 2	3.02	4.13	8.16	0.82	25.00	4.94		53.93	100.00
Spectrum 3	2.75	2.71						94.54	100.00

Table 15: Energy Dispersive X-ray spectroscopy for the spectra at 850 ^{O}C. Results in weight %

Spectrum	C	O	Cr	Mn	Fe	Ni	Mo	Ta	Total
Spectrum 1	2.35		17.55	1.80	62.37	13.16	2.76		100.00
Spectrum 2	2.70	2.79	9.57	0.79	31.72	6.07		46.35	100.00
Spectrum 3	2.04	2.29						95.67	100.00

APPENDIX C

Uncertainty Analysis of the model's sensitivity to Chlorine flow rates (Referred to in section 7)

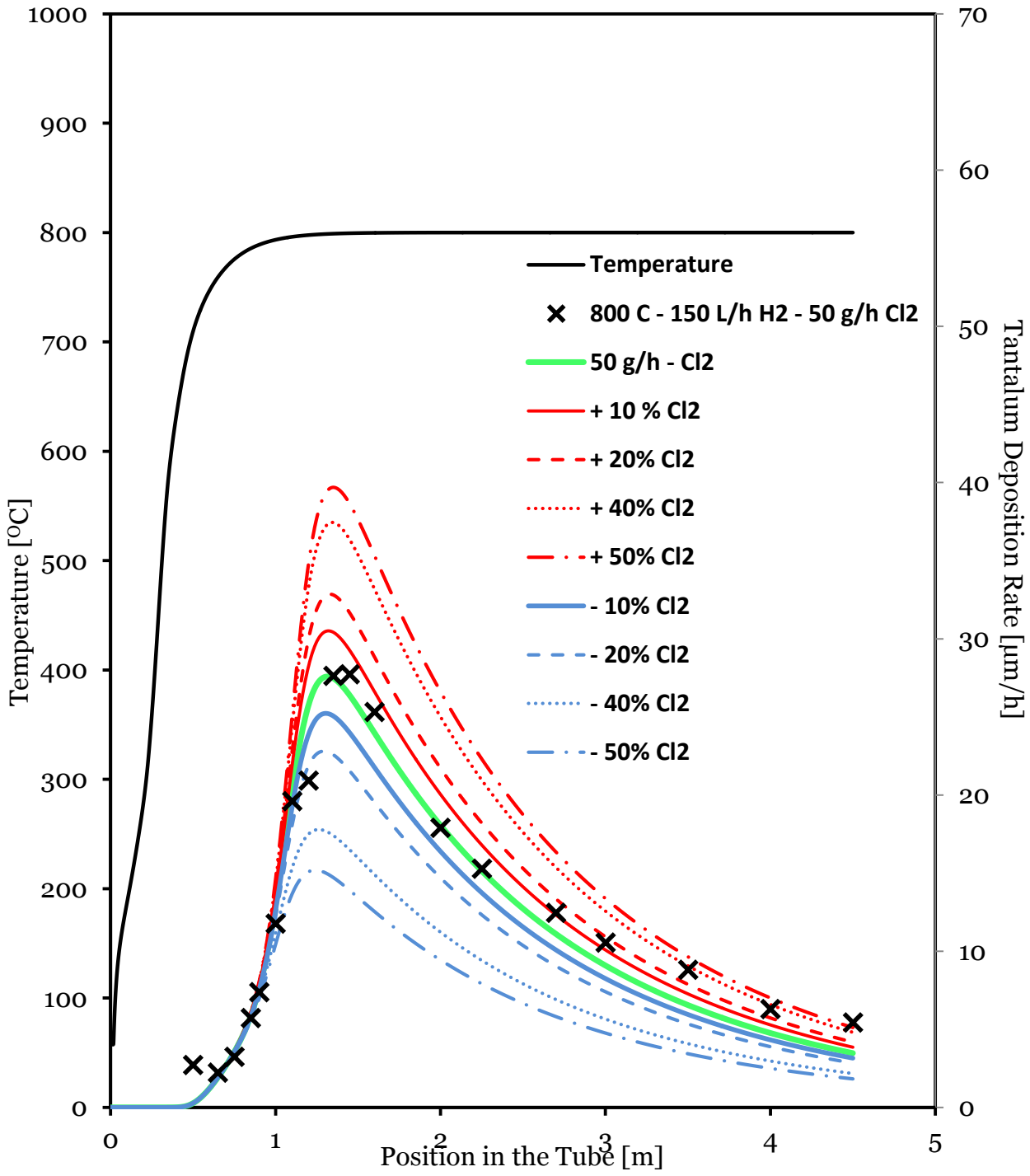

Figure 89: Uncertainty Evaluation of the Chlorine Flow rate. Based on the 50 g/h (green line) benchmark. The crosses represent experimental data at the benchmark conditions.